EFFECTS OF THREE-DIMENSIONAL FORCING ON ALONGSHORE CURRENTS: A COMPARATIVE STUDY

By

KRISTEN D. SPLINTER

A THESIS PRESENTED TO THE GRADUATE SCHOOL
OF THE UNIVERSITY OF FLORIDA IN PARTIAL FULFILLMENT
OF THE REQUIREMENTS FOR THE DEGREE OF
MASTER OF SCIENCE

UNIVERSITY OF FLORIDA

2004

This thesis is dedicated to my parents, for their support and guidance throughout my education.

ACKNOWLEDGMENTS

I would like to thank my parents for their continual support throughout my education; pushing me to excel, and letting me find my way. I thank my sister, Karen, and my parents, for always being there when I needed someone to talk to.

I would like to extend my appreciation to my advisor, Dr. Donald N. Slinn, for his patience and guidance throughout the process. I thank Drs. Robert Thieke (University of Florida), and Todd Holland and Joe Calantoni (Navel Research Laboratory, Stennis Space Center, MS) for giving me the opportunity to help with field research. It brought a new level of understanding to my work. I also thank Dr. Kraig Winters (Scripps Institute of Oceanography, San Diego, CA) for the use of his computer programs and for his continued support throughout. I would also like to thank Drs. Robert Dean and Robert Thieke for serving on my supervisory committee.

I thank all of the students and faculty who have helped me along the way; Brian Barr, Jodi Eshleman, Jamie MacMahan, Jon Miller, Robert Weaver, and Bret Webb. Their guidance and friendship throughout this process, along with their patience with my computer problems and various dilemmas have been greatly appreciated. Finally, I thank all of my housemates and friends in Gainesville who made me feel welcome and part of a family so far away from home.

TABLE OF CONTENTS

LIST OF TABLES

LIST OF FIGURES

Abstract of Thesis Presented to the Graduate School
of the University of Florida in Partial Fulfillment of the
Requirements for the Degree of Master of Science

EFFECTS OF THREE-DIMENSIONAL FORCING ON
ALONGSHORE CURRENTS: A COMPARATIVE STUDY

By

Kristen D. Splinter

August 2004

Chair: Donald N. Slinn
Major Department: Civil and Coastal Engineering

Our study introduced a new 3D, time-dependent, non-hydrostatic, Large Eddy Simulation (LES) nearshore circulation model. It was wave-phase-averaged, in a curvilinear, bottom conforming, σ-coordinate system; with a rigid lid that was capable of examining depth-dependent, low-frequency, and nearshore current response to breaking waves in the surf zone. A principal advantage of our model was that it included dynamics of the undertow and vertical mixing that led to enhanced cross-shore mixing. Uncertainties associated with modeling bottom friction were reduced because bottom stress was modeled with the no-slip condition by using a high-resolution vertically clustered grid with O (1-10 cm) scales near the seabed. The LES turbulence closure scheme produced reasonable time-averaged alongshore and cross-shore vertical velocity profiles.

The model was formulated for alongshore-uniform bathymetry, and included a shore-parallel sand bar. Forcing conditions for the alongshore currents in the model were coupled to beach topography and specified surface wave conditions, using the

Thornton-Guza (1983,1986) wave breaking sub-model. The model included wave set-up through an induced cross-shore pressure gradient. A variety of vertical distributions of the wave-induced radiation stresses were tested. Results indicated that vertical profiles for undertow, mean alongshore current profiles, and dynamics of alongshore-current shear instabilities depended on the particular approximation chosen for the forcing.

In contrast to simulations using a depth-averaged 2D model, the initial instabilities developed on the vertical shear in the water column and produced relatively short wavelength disturbances that caused the flow to transition to turbulence before organizing into larger scale flow features. The strength, stability, and location of the alongshore current were dependent on the vertical distribution of forcing and domain length. Depth-varying forcing suppressed the development of the large-scale shear instabilities and influenced the time-dependent effects of the unsteady flows. Short domains [O (20 m)] were dominated by the effects of the vertical distribution of forcing that produced stronger mean alongshore currents with peaks located shoreward of the nearshore bar. Long domains [O (200 m)], however, included the effects of shear waves, and produced mean alongshore currents with broader cross-shore profiles, and less distinct peaks located further in the bar trough.

Including the effects of anisotropic mixing, vertically dependent forcing, and large-scale shear instabilities produced mean alongshore currents that were of reasonable magnitude centered in the bar trough of a barred beach system.

CHAPTER 1
INTRODUCTION

The circulation patterns of the surfzone are important because they affect the alongshore and cross-shore movement of sediment, and the strength of the overall currents. Two distinct types of idealized nearshore circulation models are commonly used to investigate aspects of surfzone dynamics. Two-dimensional (2D) cross-shore (x-z) circulation models are often used to study sediment transport and undertow. These generally assume alongshore uniformity, and are sensitive to the vertical distribution of wave shear stresses. The second class of models simulate 2D alongshore (x-y) currents. These generally consider variations of the current and topography in both the alongshore and cross-shore directions, but are approximated by a depth-averaged current. Some alongshore current models have proven useful for predicting the current structure on plane beaches for certain wave conditions, but are less useful for a barred beach system.

According to wave radiation stress theory (Longuet-Higgins, 1970), alongshore currents are produced near the location of wave breaking. In a barred beach system, this commonly occurred near the bar crest, and at the shoreline. Some field observations, however, showed that a mean current maximum developed in the trough region, a location where reduced breaking occurred (Church et al., 1992). Our purpose was to gain a better understanding of the physics that influenced alongshore currents.

Most contemporary nearshore circulation numerical models (Allen et al., 1996; Slinn et al., 1998, 2000; Özkan-Haller and Kirby, 1999; Van Dongeren and Svendsen, 2000) used various forms of the 2D depth-integrated flow approximation. Although

valid, because the water was shallow, O (1 m), compared to its horizontal dimensions, O (100 m), this approximation may have obscured several important three-dimensional (3D) features. Two such features were:

- A depth-dependent vertical distribution of the cross-shore radiation stress could have produced shoreward momentum flux in the upper portion of the water column, and a resulting return flow in the lower portion of the water column, known as undertow.

- Under some conditions, breaking waves could have effectively mixed the momentum across the water depth at relatively high frequency.

Together these processes might have led to enhanced cross-shore diffusion rates that could have decreased the mean cross-shore shear of the alongshore current, and shifted the peak current toward the bar trough.

Ongoing research to explain the shoreward shift of the alongshore current on a barred beach has focused on four main topics: shear waves, cross-shore circulation, wave rollers, and alongshore pressure gradients. These topics and aspects of the vertical distribution of the wave radiation stresses are reviewed next.

Methods of Cross-Shore Mixing

Shear Instabilities

Strong alongshore currents on the order of 1 m/s have been generated in the surfzone by the alongshore momentum flux caused by obliquely incident surface gravity waves. The transfer of momentum from the wave field to the mean current was characterized by the cross-shore gradient of the wave radiation stress (e.g., dS_{xy}/dx) (Longuet-Higgins, 1970). Greenwood and Sherman (1986) discussed lateral mixing of alongshore current profiles over barred beaches, and suggested that for a plane beach solution, the presence of bars would enhance lateral mixing by increasing the cross-shore velocity gradients. Observations at Duck, North Carolina by Oltman-Shay et al. (1989)

showed the presence of alongshore propagating velocity perturbations associated with the presence of shear in the alongshore currents. Özkan-Haller and Kirby (1999) and Slinn et al. (1998, 2000) showed that the nonlinear evolution of shear instabilities provided significant horizontal mixing of alongshore momentum that affected the cross-shore distribution of the alongshore current. The stability and structure of shear instabilities depended on several factors. These included magnitude and cross-shore profile of the alongshore current, beach topography, presence of nonzero gradients of the horizontal Reynolds stresses (Dodd and Thornton, 1990), and bed shear stress (Dodd et al., 2000).

Shear instabilities were distinguished from gravity waves because their periods [O (10^2-10^3 s)], were too long for their associated wave lengths [O (10^2 m)] (Oltman-Shay et al., 1989) based on the dispersion relationship. (E.g., a 100 m long wave in 5 m of water should have had a period of approximately 14.5 s). Shear waves were most pronounced in areas where strong alongshore O (1 m/s) currents were present, and had total RMS shear wave fluctuations varying between 10 and 40% of the maximum alongshore current (Noyes et al., 2004). They were generated as the alongshore current grew in strength and became unstable, which caused the alongshore current to meander in a sinusoidal pattern, and first appeared as an alongshore progressive wave feature (Bowen and Holman, 1989). They were often strongest, and most prevalent on barred beach profiles where wave breaking over the bar generated a strong shear in the alongshore current, and enhanced the growth rate of the shear waves (Dodd et al., 2000).

Field observations by Noyes et al. (2004) also suggested that these instabilities were generated in the region where the greatest shear occurred, just seaward of the location of the maximum alongshore velocity. The instabilities were characterized by an

exchange of energy from the mean current to a perturbation velocity field. Cross-shore mixing of alongshore momentum through the Reynolds stresses usually occurred when the cross-shore gradient of the depth-averaged alongshore velocity went through an inflection point (Dodd and Thornton (1990) and Rayleigh (1880)).

Research to explain the field observations of shear instabilities has been based on linear theory, weakly nonlinear theory, and nonlinear analysis of shear wave growth. Bowen and Holman (1989) used linear stability analysis of depth-integrated currents to show that these disturbances could have been produced by instabilities developed by the cross-shore shear of the alongshore current. Allen et al. (1996) used a nonlinear model to show that the finite amplitude behavior of unstable flows on plane beaches could be described by the ratio of frictional to advective terms (ΔQ). As the friction factor was decreased, the flows changed from weakly unstable, to chaotic. They also examined the effect of different alongshore domain lengths, and concluded that shear wave instabilities initially grew at the wave length corresponding to the fastest-growing linearly unstable mode ($2\pi / k_o$). As domain length increased, however, the initial disturbances of the flow merged, and their length scales evolved into longer wave length propagating disturbances when ΔQ was moderate to large (Allen et al., 1996).

Slinn et al. (1998) extended the work of Allen et al. (1996) by applying coupled forcing to a barred beach profile. They found that short wave-length disturbances continued to dominate the velocity spectrum even for large values of ΔQ. They presented four different flow regimes that were attained by altering the bottom friction. As bottom friction was decreased, instabilities of the current changed from stable shear waves, to fluctuating vortex patches, to shedding vortex pairs, and finally to turbulent shear flows.

Finite amplitude structures generated were independent of domain length for a barred beach system, and remained at length scales predicted by linear theory: on the order of 100 to 200 m. The strength of these fluctuations increased as bottom friction decreased. This agreed well with Dodd (1994) and Falques and Iranzo (1994) who found that increasing the bed shear stress and eddy viscosity reduced the current velocity and dampened the shear instabilities.

Once the alongshore instabilities grew to finite amplitude, they continued to evolve and shed vortices from the mean current. Bowen and Holman (1989) suggested that this might be an important feature of cross-shore mixing in this environment, because shear instabilities might provide rates of turbulent diffusion up to ten times greater than those produced by breaking gravity waves.

Cross-Shore Circulation: Mass Flux and Undertow

Cross-shore circulation was usually excluded from 2D depth-averaged alongshore current models because of the approximation that alongshore and cross-shore currents were approximately vertically uniform. Although this approximation was often sufficient for large-scale nearshore models, cross-shore circulation existed and could potentially have influenced the alongshore current. Instead, mass flux and undertow were studied in 2D cross-shore circulation models. Cross-shore circulation was driven by the onshore component of the wave radiation stress gradient, dS_{xx}/dx. The undertow was largely a result of the local variation between the depth-dependent radiation stress and the depth-uniform horizontal pressure gradient due to set-up. These were in equilibrium with each other over the water depth (Svendsen, 1984a), but unbalanced throughout the water column. As the waves traveled through the surfzone and breaking occurred, their wave heights decreased, and resulted in a decreased shoreward mass flux. This produced a

downwards directed flow (Svendsen, 1984a) from the free surface, and also encouraged cross-shore circulation. The mass flux above the trough level from the shoaling waves pushed the alongshore current near the surface shoreward, while the alongshore current near the bottom was pulled seaward by the increased return flow in the undertow. Svendsen and Lorenz (1989) noted that in the surfzone, the wave-averaged cross-shore current always had a shoreward velocity component near the free surface, and an off-shore directed component near the bottom.

Results from cross-shore circulation models were sensitive to boundary conditions and integral constraints. Cross-shore models tended to invoke:

- Depth-integrated mass balance (net zero mass flux).
- A no-slip condition on the bottom boundary (Svendsen and Hansen, 1988).

The choice of the turbulent eddy-viscosity term in these models also contributed to the predicted undertow profile. Haines and Sallenger (1994) found that the eddy-viscosity varied significantly over the cross-shore in the surfzone, and also varied in the vertical near the top and bottom boundaries. Faria et al. (2000) disagreed, and found that a depth-dependent eddy viscosity did not reduce the differences between model results and field data. Using a constant eddy-viscosity inside and outside the boundary layer, with the no-slip bottom boundary condition, however, yielded onshore velocities in the bottom boundary layer. This result, however, contradicted field data from Hansen and Svendsen (1984) and Haines and Sallenger (1994) who observed a strong undertow jet over the bar during their field experiments. Two modeling approaches have been developed to address this problem. Stive and Wind (1996) suggested replacing the no-slip condition at the bottom with a specified shear stress at the wave trough level.

Svendsen et al. (1987) proceeded with the no-slip condition, but applied two eddy viscosity terms: with a smaller one in the boundary layer than in the interior of the fluid.

Several lab experiments have been conducted to study the undertow profile. Matsunaga et al. (1988, 1994) found instabilities in the off-shore directed flow seaward of the breaker line. These instabilities, which they termed a vortex train, consisted of a solitary layer of large eddies rotating about a horizontal, alongshore axis. Larger scale lab experiments conducted by Li and Dalrymple (1998) showed two layers of oppositely rotating vortex trains. These vortex trains caused vertical mixing of the cross-shore current and could potentially affect the alongshore current as well.

Faria et al. (2000) presented model results for the vertical structure of the undertow. The undertow was not uniform with depth, over the cross-shore, or steady in time. Undertow flows were approximately parabolic in the vertical, and varied in magnitude with water depth. In the inner trough zone, they found the return flow was weak with very little vertical structure. Maximum offshore flows occurred at the shoreward face, and on top of the bar, which coincided with areas of intense wave breaking. Seaward of the bar, they found that the undertow was nearly depth uniform. The variation of the undertow across the surfzone could induce cross-shore mixing of the alongshore current.

The changing strength of the undertow across a barred beach profile was explained by channel flow theory and mass conservation. As the cross-sectional area decreased in shallow water, the flow velocity must have increased to conserve volumetric flow rate. The same concept held on the offshore side of the bar where undertow currents decreased. Putrevu and Svendsen (1992) suggested that the vertical profile of the undertow could have caused considerable shearing of the alongshore current in the

cross-shore direction. Including effects of variable cross-shore circulation could influence the position of the alongshore current.

Surface Rollers

The standard wave radiation stress theory assumed an instantaneous transfer of momentum from breaking waves to the mean water column. The wave roller was introduced to represent the intermediate process that gradually released energy and momentum from the breaking wave bore into the water column over some distance. The wave roller effectively redistributed the incident wave stress over the surfzone (Lippmann et al., 1995) and was most noticeable on a barred beach (Svendsen, 1984b), where multiple breakpoints were common.

The transfer of momentum was described as a two-step process. The momentum from a breaking wave was supplied to a turbulent roller that in turn transferred momentum through a surface shear stress (Deigaard, 1993) to the water column at a finite rate. The roller was an approximation to the front face of a breaking wave, where turbulent fluid was conveyed at the wave celerity (Lippmann et al., 1995). In their model, wave asymmetry, and phase speed determined the spatial distribution and intensity of the roller energy dissipation. Waves with smaller asymmetry, or increased local water depth, resulted in a shoreward shift of the break point, and an increased distance that the roller traveled. Together these effects shifted the current towards the trough region. The spatial lag of momentum input into the mean currents by the roller was an efficient means for offsetting the current maximum from over the bar into the trough.

Although rollers were able to shift the momentum input shoreward of the bar, their effect alone did not accurately predict the cross-shore distribution of alongshore currents

(Lippmann et al., 1995). Reniers and Battjes (1997) presented laboratory results of alongshore currents over barred beaches that showed:

- The roller contribution helped to describe the cross-shore distribution of the observed shear stress.
- Lateral mixing alone had no significant influence on the location of the maximum velocity.

The concept that emerged was that the velocity profile was shifted shoreward by the roller, and spread horizontally by the effect of lateral mixing.

Alongshore Pressure Gradients

In the same paper, Reniers and Battjes (1997) also suggested that alongshore pressure gradients were important for predicting alongshore current location. Laboratory experiments of wave driven currents over a barred beach in the absence of alongshore pressure gradients produced alongshore currents near the regions of breaking; over the bar, and at the shoreline. They hypothesized that alongshore currents located in the trough were explained by alongshore pressure gradients in the field due to uneven topography in the alongshore direction.

Putrevu et al. (1995) conducted model studies that examined the importance of including the effects of alongshore non-uniformities on alongshore currents. Variable beach topography in the alongshore direction affected the breaker height and location of wave breaking in the cross-shore. Including the forcing from alongshore pressure gradients had a significant impact on the alongshore current location. They found that this component could be almost equal in magnitude to the forcing due to the alongshore component of the radiation stress term in some cases. The effect of the alongshore

pressure gradient was dependent on the angle of wave incidence: it increased as waves approached closer to shore normal.

Slinn et al. (2000) coupled topography and radiation stress gradients over alongshore variable topography in numerical model experiments to test this hypothesis. Their results showed that currents tended to follow contours of constant depth. Variable points of wave breaking caused momentum to be inputted at different cross-shore locations depending on topography. The alongshore pressure gradients and the radiation stress terms counteracted each other to some degree. They concluded that alongshore pressure gradients alone were insufficient to produce peak currents in the trough. They concluded, however, that topographic variability in the alongshore had a significant influence on nearshore circulation.

Vertical Distribution of Wave Stresses

In depth-integrated, 2D, circulation models on a uniform coast with straight and parallel contours, alongshore currents were forced by the cross-shore gradients of the depth integrated wave radiation stresses, dS_{xy}/dx. With the advancement to quasi-3D and 3D modeling techniques, the distribution of the wave shear stresses within the water column became important. Earlier work describing the vertical distribution of wave stresses was simplified to examine shore normal waves, where $dS_{xy}/dx = 0$. The only dynamic wave force present in these models was dS_{xx}/dx, which drove set-up and cross-shore circulation.

Longuet-Higgins and Stewart (1964) defined the relationship between the depth-dependent radiations stress, $s_{xx}(z)$ and the depth-integrated value that was used in

2D circulation models as $S_{xx} = \int_{-h}^{\zeta} s_{xx}(z)dz$. The wave radiation stress, S_{xx}, was divided into three parts, so $S_{xx} = S_{xx}^{(1)} + S_{xx}^{(2)} + S_{xx}^{(3)}$. The breakdown of each component was:

$$S_{xx}^{(1)} = \overline{\int_{-h}^{\zeta} \rho u^2 dz} = \int_{-h}^{0} \rho \overline{u^2} dz \quad (1)$$

$$S_{xx}^{(2)} = \overline{\int_{-h}^{0} (p - p_0)dz} = \int_{-h}^{0} (\overline{p} - p_0)dz = \int_{-h}^{0} (-\rho \overline{w^2})dz \quad (2)$$

$$S_{xx}^{(3)} = \overline{\int_{0}^{\zeta} pdz} = \frac{1}{2}\rho g \overline{\zeta^2} \quad (3)$$

In shallow water, $S_{xx}^{(1)} + S_{xx}^{(2)} = \int_{-h}^{0} \rho \overline{u^2} dz$ because $u^2 >> w^2$. This term was due to the momentum of the wave orbital motion, and was equal to the total energy density of the waves, E. It was distributed evenly over the water column and accounted for two-thirds of the total radiation stress. $S_{xx}^{(3)}$ was the pressure term due to the waves, and was equal to ½ E. It accounted for one-third of the total force, and was centered about the mean water level (MWL) (Figure 1). S_{xy} lacked the pressure terms due to the waves, and was given by the relationship $S_{xy} = \overline{\int_{-h}^{\zeta} \rho uvdz}$.

Deigaard and Fredsoe (1989) compared their findings to the works of Dally and Dean (1984), and Svendsen (1984a), for the vertical variation of the wave induced shear stress that included components of radiation stress, wave roller effects, and set-up. Their analyses were based on linear shallow water wave theory over a horizontal bottom. Dally and Dean (1984) modeled the vertical distribution of radiation stress following the approach of Longuet-Higgins and Stewart (1964). The resulting shear stress distribution was split up into the three components: wave motion, surface roller, and set-up. Dally

and Dean (1984) did not include the effect of a surface roller. They assumed the set-up balanced the radiation stress gradient, and the result was a linear distribution of the shear stress across the water column, and a depth-uniform distribution of the radiation stress below the trough. The shear stress had a maximum at the MWL and was zero at the bed (Figure 2).

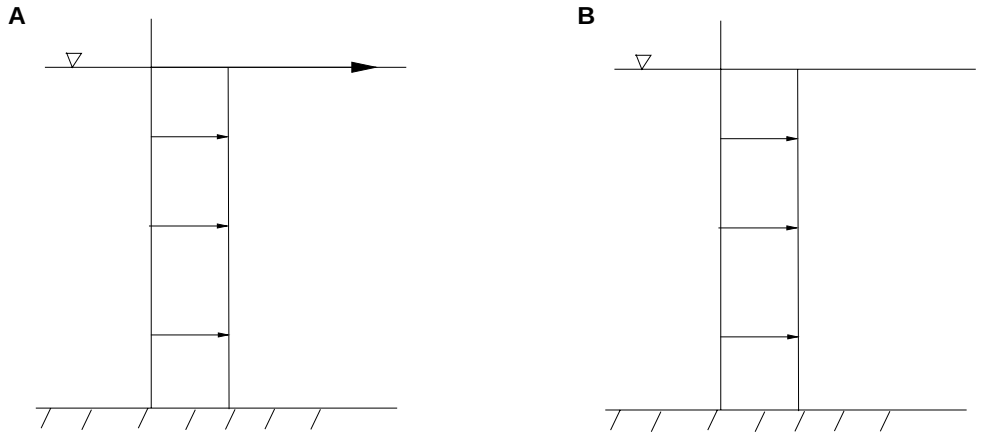

Figure 1. Longuet-Higgins and Stewart's description of the vertical distribution of the total radiation stresses. A) $s_{xx}(z)$. B) $s_{xy}(z)$

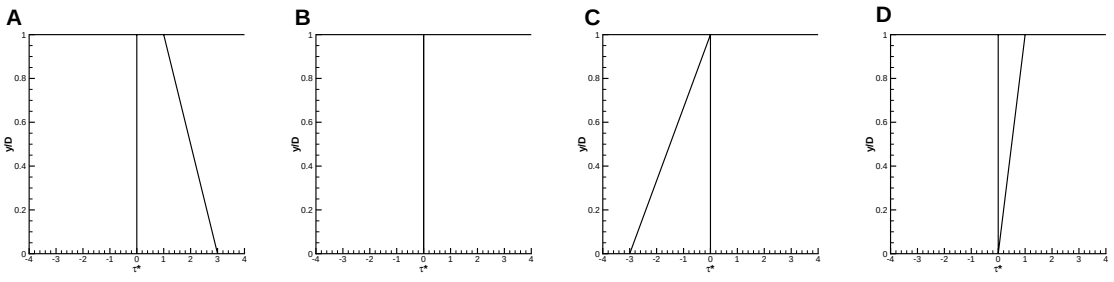

Figure 2. Dean and Dally's description of the components of shear stress distribution. y/D is the normalized water depth. $\tau^* = -\tau / \left(\frac{1}{16} \rho g \frac{dH^2}{dx} \right)$. A) Wave motion. B) Surface roller. C) Setup. D) Resulting shear stress distribution.

Svendsen's (1984a) results were similar to Dally and Dean (1984). He used the same linear shallow water wave theory, but included the effect of a surface roller. The

surface roller added an additional component to the pressure gradient that produced a depth-uniform addition to the shear stress distribution (Figure 3B). The wave setup component was also adjusted so that the total shear stress was still linearly distributed with depth (Figure 3C). In this formulation, the total wave shear stress term had a maximum at the MWL about twice that of Dally and Dean (1984) and zero at the bed (Figure 3D). This resulted in a stronger net cross-shore shear force than Dally and Dean (1984) predicted.

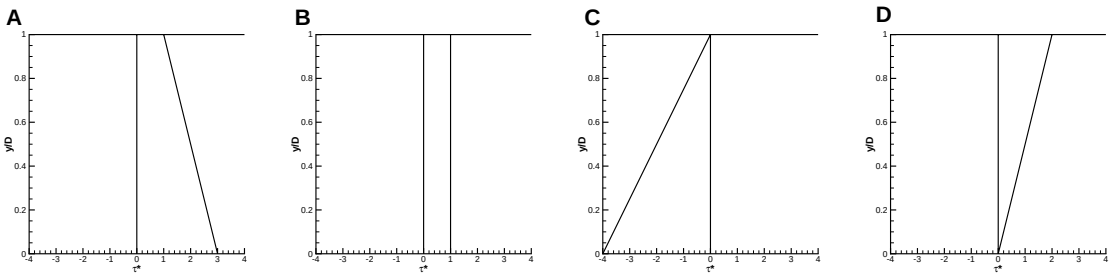

Figure 3. Svendsen's description of the components of shear stress distribution. $\tau^* = -\tau / \left(\frac{1}{16} \rho g \frac{dH^2}{dx} \right)$. y/D is the normalized water depth. A) Wave motion. B) Surface roller. C) Setup. D) Resulting shear stress distribution.

Dally and Dean (1984) and Svendsen (1984a) both used a control volume approach to describe the distribution of shear stress and omitted the transfer of momentum ($\overline{UW}$) through the bottom of the control volume. In the presence of irregular waves, such as in the surf-zone, Deigaard and Fredsoe (1989) showed that this term was significant to the overall magnitude and distribution of the shear stress. They found that the $\overline{UW}$ term doubled the surface shear stress. The magnitude of the surface roller effect was also slightly higher in their calculations compared to Svendsen (1984a). As a result of the larger shear stresses due to wave motion and the surface roller, the balancing shear stress due to set-up was also larger. The net distribution (Figure 4) still increased linearly with

height: with zero shear stress at the bed, and a maximum at the MWL almost three times that of Dally and Dean (1984) and one and a half times that of Svendsen (1984a). The reader is referred to Deigaard and Fredsoe (1989) for a more detailed comparison of the three theories presented.

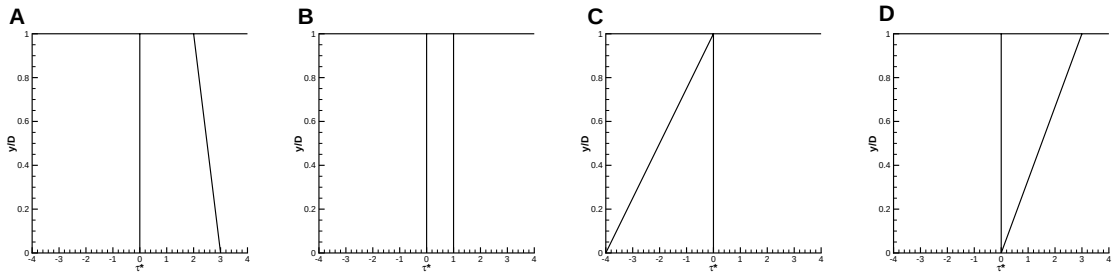

Figure 4. Deigaard and Fredsoe's description of the components of the shear stress distribution. y/D is the normalized water depth. $\tau^* = -\tau / \left(\frac{1}{16} \rho g \frac{dH^2}{dx} \right)$. A) Wave motion. B) Surface roller. C) Setup. D) Resulting shear stress distribution.

Sobey and Thieke (1989) discussed the importance of depth-dependent forcing in the nearshore region. They clarified that although depth integration of the forcing was valid because it produced a net zero mass flux condition in the cross-shore direction, it did not include the cross-shore circulation produced by the wave induced mass-flux and undertow. Their wave action term ($(\rho \overline{\tilde{u}^2} - \rho \overline{\tilde{w}^2})$) in $s_{xx}(z)$, where $\tilde{u}, \tilde{w}$ were the time-averaged, u-, w-velocity fluctuations, was vertically uniform in agreement with Dally and Dean (1984). Their pressure gradient term, however, linearly increased from the trough to the MWL, where it reached a maximum. A complementary linear decrease in the apparent stress from MWL to the wave crest was also predicted (Figure 5).

Rivero and Arcilla (1995) extended the work of Deigaard and Fredsoe (1989) and demonstrated that a sloping bottom bed had an important effect on the wave shear stress.

Under dissipative wave conditions, the resulting distribution had a nonzero value at the bed equal to $\left(\frac{E}{\rho h}\right)\tan\beta$ that linearly increased to a maximum of $\left(\frac{E}{\rho h}\right)\tan\beta - \frac{1}{2}\left[\frac{\partial}{\partial x}\left(\frac{E}{\rho}\right) - \left(\frac{E}{\rho}\right)\frac{\partial h}{\partial x}\right]$ at the MWL (Figure 6).

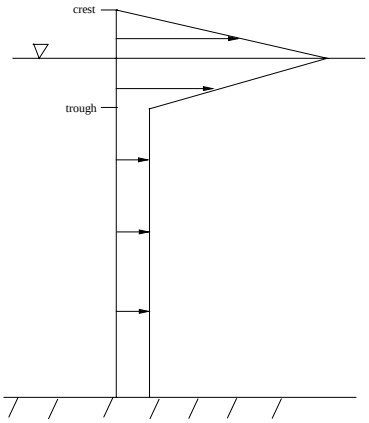

Figure 5. Sobey and Thieke's description of apparent radiation stress ($s_{xx}(z)$) distribution.

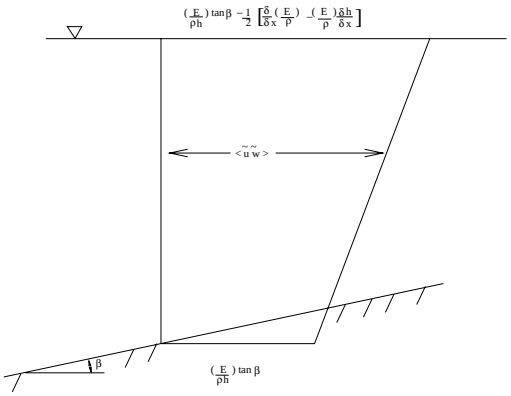

Figure 6. Rivero and Arcilla's description of the shear stress distribution for sloping topography.

More recently, the work of Mellor (2003) addressed the vertical distribution of both the alongshore and cross-shore wave radiation stresses for surface waves (Figure 7). His equations for radiation stress were:

$$S_{\alpha\beta} = kDE\left[\frac{k_\alpha k_\beta}{k^2} F_{cs}F_{cc} + \delta_{\alpha\beta}\left(F_{cs}F_{cc} - F_{ss}F_{cs}\right)\right] \quad (4)$$

where:

$$F_{ss} = \frac{\sinh kD(1+\zeta)}{\sinh kD}, \qquad F_{cs} = \frac{\cosh kD(1+\zeta)}{\sinh kD},$$

$$F_{sc} = \frac{\sinh kD(1+\zeta)}{\cosh kD}, \qquad F_{cc} = \frac{\cosh kD(1+\zeta)}{\cosh kD}.$$

He described $E = \frac{ga^2}{2}$, D was the depth, $\delta_{\alpha\beta}$ was the Kronecker delta function, and ζ was the transformed vertical coordinate such that ζ = -1 when z = -h and ζ = 0 at the surface.

His resulting vertical distribution for $s_{xx}(z)$ differed from previous theory. As seen in Figure 7A, $s_{xx}(z)$ linearly increased with depth. This was due to the F_{ss} term that linearly decreased with depth and was subtracted from the other radiation stress components. When vertically integrated over the water depth, his equations were off by a factor of rho (1000 kg/m^3) in comparison to the depth averaged equations given by Mei (1989) Eq. 3-10. Vertical integration of his equations and the determination of the vertical distribution of each of his sub-terms (F_{ss}, F_{sc}, F_{cs}, and F_{cc}) were calculated separately. This was done to ensure that the resulting vertical distribution presented above was not an error in inputting the equations into the model. The vertical distributions of the sub-terms used in the model were similar to those presented in his paper. His $s_{xy}(z)$ term remained roughly depth-linear because the 2nd term (with the Kronecker delta) in his equation only existed for normal ($s_{xx}(z)$, $s_{yy}(z)$) forces. This representation of radiation stresses remains questionable for its purpose and validity in the nearshore. Putrevu and Svendsen (1999) and Zhao et al. (2003) also discussed effects

of the local contribution of the radiation stress on lateral mixing within the surfzone but are not discussed in detail.

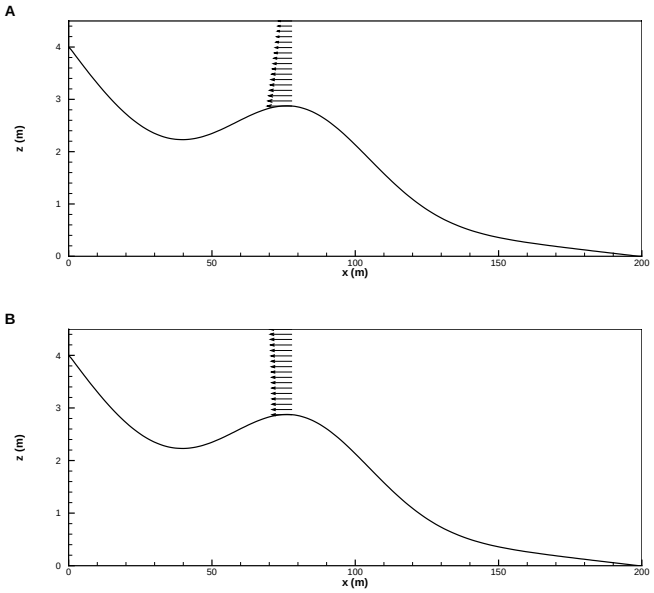

Figure 7. Mellor's description of the distribution of radiation stresses. A) $s_{xx}(z)$, B) $s_{xy}(z)$.

The $s_{xx}(z)$ term affected the cross-shore flow and potentially the location of the alongshore current. In the formulations based on linear wave theory, the $s_{xy}(z)$ term did not include a depth-dependent pressure term as found in $s_{xx}(z)$. It was therefore uniformly distributed over depth, and drove the alongshore currents. The local variation of the radiation stresses over depth and the resulting cross-shore and alongshore currents could cause a lateral mixing effect that might dominate over turbulent mixing (Putrevu and Svendsen, 1999).

Chapter Contents

A main purpose of our study was to investigate the effects of the vertical distribution of radiation stresses on the phase-averaged alongshore current position, the formation of shear instabilities, the net horizontal mixing, and to compare the influence

of vertical forcing with those of previous theories. A variety of vertical distributions of the radiation stresses were tested in a 3D, phase-averaged, Large Eddy Simulation (LES) nearshore circulation model over an alongshore uniform barred beach bathymetry. The use of a 3D model allowed for the development, interaction, and analysis of cross-shore mixing by the undertow with the alongshore current. Mixing effects caused by large-scale shear instabilities, and those due to depth-dependent cross-shore circulation, were examined separately by utilizing alongshore domains of varying dimensions. The smaller [O (20 m)] domain inhibited the development of the fastest growing linearly unstable modes that produced large-scale [O (100 m)] shear waves. Longer domains [O (200 m)] were also modeled that permitted shear waves to be developed and allowed a determination of the relative contribution to cross-shore mixing of the two processes.

The thesis is divided into five chapters. Chapter 2 reviews some previous model studies of alongshore current distributions and shear waves. Chapter 3 covers the 3D model problem setup, governing equations, and details of sub-models used in the numerical experiments. Chapter 4 provides a description of the simulations and the main results. The discussion focuses on the effects of the vertical distribution of the radiation stress and the response of the flows. Emphasis is given to the stability and structure of the alongshore current, the cross-shore current structure, and the effects of model approximations. The effect of domain length and the relative magnitude of lateral mixing caused by shear waves and radiation stress distributions are also addressed. Chapter 5 summarizes conclusions of the work, considers strengths and limitations of this approach, and outlines future directions.

CHAPTER 2
MODEL COMPARISONS

This chapter summarizes work of three previous model studies that focused on shear instabilities, and their effect on alongshore currents on barred beaches. Two of the models were 2D, and one was quasi-3D, a sophisticated hybrid approach.

Two-Dimensional Alongshore Current Models for Barred Beaches

Traditional 1- and 2D phase-averaged models were unsuccessful at predicting the location of the peak alongshore current on barred beaches. Using linear wave theory, breaking wave parameterizations, and depth-averaged mean flow equations, they predicted peak currents at the two locations of maximum wave breaking intensity: the bar and the shoreline. Some field data, however, showed peak currents located in the trough region, an area where reduced breaking occurred (Church et al., 1992). A probable contributing factor in this discrepancy was the effects of shear waves.

In this section, two similar modeling approaches are discussed and summarized in Table 1. The first, by Slinn et al. (1998), was a qualitative examination of the shear instability problem, and the second, by Özkan-Haller and Kirby (1999) was a more quantitative analysis with comparisons of their model results to field data from the SUPERDUCK experiment. The two models used slightly different governing equations, but both showed that shear waves could alter the alongshore current profile, and caused increased flow in the trough region. Both of the models were phase-averaged and worked with depth-averaged currents. For a full description of the models and their

results, the reader is referred to Allen et al. (1996), Slinn et al. (1998), and Özkan-Haller and Kirby (1999).

In both models, as the frictional terms (C_f) were decreased, the alongshore currents became stronger and contained more perturbations. Results of varying the frictional terms are presented in Figure 8. These were obtained using a model similar to the one used by Slinn et al. (1998). A consequence of the more unsteady flows was the shedding of more vortices, and resulted in the cross-shore mixing of the alongshore current (Figure 8D). For high values of C_f (Figure 8A), the currents were weak and stable. For moderate values (Figure 8B), the current remained relatively stable over time, with a small amount of horizontal spreading: peak values in the trough increased as currents over the bar decreased, but the location of the maxima did not change. As C_f was decreased, the peak currents increased before instabilities appeared (Figure 8C, Figure 8D). With lower friction coefficients, the current became strongly unstable. At the lowest value (Figure 8D), the current had the broadest cross-shore distribution due to more energetic instabilities that increased horizontal mixing.

Slinn et al. (1998) found that lowering the bottom friction coefficient shifted energy in the frequency - alongshore wave number (f - k_y) spectra to smaller length and shorter timescales. Özkan-Haller and Kirby (1999) also varied their horizontal mixing coefficient (M) in their diffusion terms to approximate diffusion caused by breaking waves or depth-varying currents. They found that by increasing the mixing coefficient, they generated less energetic instabilities at longer length scales. The model of Özkan-Haller and Kirby (1999) was able to approximate alongshore currents and propagation speeds of the instabilities for the SUPERDUCK experiment. It should be noted,

however, that peak alongshore currents for the days they simulated were still located near the nearshore bar and not in the trough. Their model was also not able to accurately match the observed frequency spectra, predicting more energy at lower frequencies than observed.

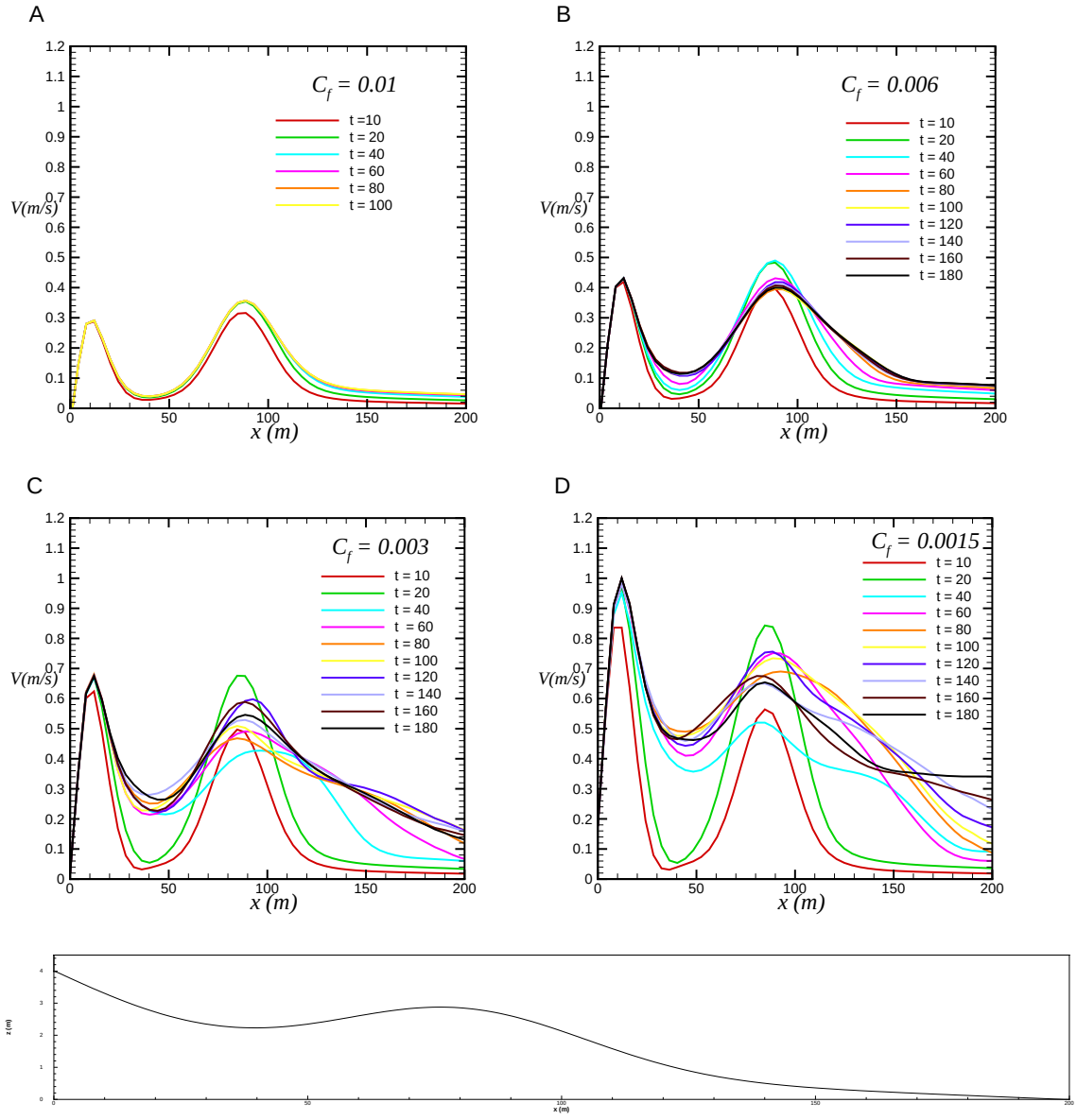

Figure 8. Comparison of alongshore current profiles from 2D circulation for varying values of C_f over time. Results were from a 2D model similar to the one used by Slinn et al. (1998). H_o = 0.7 m, T_p = 8 s, θ_o = 30°. Bottom panel is the beach topography, h(x) and given in Eq.(5).

In both models, the flows that were generated were sensitive to the free parameters. As the correct representative values of these parameters were unknown for field conditions, they were tuned to produce currents similar to field data. The free parameters could be seen as a weakness of the modeling approach because they influenced the outcome at the user's discretion.

Results of the alongshore current distribution (Figure 8), and snapshots of vorticity (Figure 9) attained from a model similar to Slinn et al. (1998) are presented for comparison with the 3D model results. Wave parameters ($H_o = 0.7$ m, $T_p = 8$ s, $\theta_o = 30^o$) and bathymetry were the same for the 2D and 3D models. A coefficient of friction equal to 0.0015 was used to generate currents in the 2D model with magnitudes comparable to the 3D results. This value generated a current with strong instabilities that caused considerable mixing. Larger values of C_f produced weaker currents that became unstable at later times. The peak velocities before the current became unstable in this example were approximately 0.9 m/s over the bar, and about 1 m/s at the shoreline.

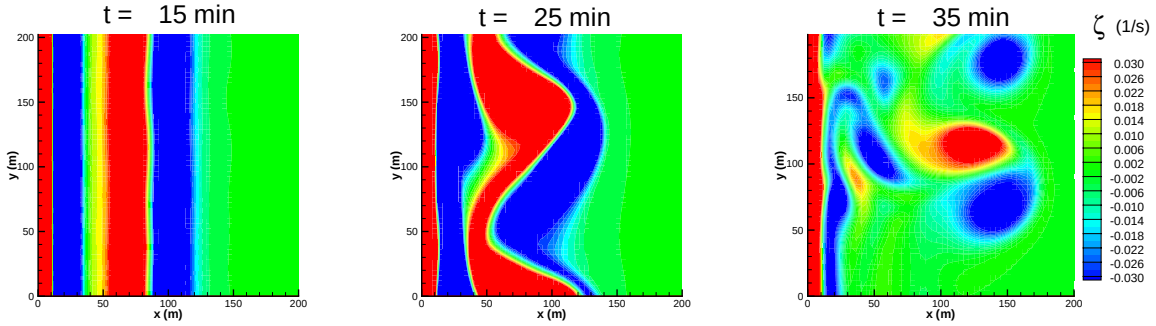

Figure 9. Vorticity contours from 2D model over time. Using a coefficient of friction (C_f) = 0.0015, the 2D results compared well with the 3D model. The current remained stable until about 20 min, then it began to meander (25 min), and evolved into large vortex structures (35 min) and remained in this condition.

Quasi-3D Models: SHORECIRC

Recent work by Zhao et al. (2003) analyzed 3D effects from shear waves using the quasi-3D nearshore circulation model, SHORECIRC. Their work focused on the importance of including the depth variation of the currents. Using the depth-integrated 2D equations, they included a quasi-3D dispersive mixing term that approximated the effect of depth-varying currents (Putrevu and Svendsen, 1999). Their parameters are summarized in Table 2. The reader is referred to Zhao et al. (2003) for a more complete description of the model and their findings.

The effect of breaking waves was parameterized with a roller model included in the radiation stress term and short wave-induced volume flux. The quasi-3D model approximated effects of vortex tilting, and depth-varying currents that produced horizontal mixing on the same order of magnitude as the shear wave component. The quasi-3D dispersive mixing term also included effects of depth-varying radiation stresses. Zhao et al. (2003) compared the quasi-3D simulation results to the 2D model results of Özkan-Haller and Kirby (1999). They found that the quasi-3D model generated a more steady flow, localized shoreward of the bar. The flow contained a less energetic turbulent kinetic energy field that was attributed to the mixing terms being of the same order as the diffusion produced by the shear waves. Özkan-Haller and Kirby (1999) found similar results when they increased their horizontal mixing coefficient.

Summary

The 2D and quasi-3D models had advantages because they produced reasonable approximations of the alongshore current structure efficiently or in a predictive, forecast manner. The use of relatively coarse grids and depth-integrated equations of motion, however, inhibited the development of 3D turbulence and depth-varying interactions

between the alongshore and cross-shore currents. The utilization of a fully 3D model with a much finer grid resolution allowed for these properties to influence the alongshore current with fewer ad-hoc approximations. This allowed greater insight into properties that might be important to the dynamics of the surfzone.

Table 1. Comparison of 2D models

Property	Slinn et al. (1998)	Özkan-Haller and Kirby (1999)
Governing equations	$(hu)_x + (hv)_y = 0,$ $u_t + uu_x + vu_y = -\frac{p_x}{\rho_o} - \mu\frac{u}{h} - \nu\nabla^4 u,$ $v_t + uv_x + vv_y = -\frac{p_y}{\rho_o} - \mu\frac{v-V}{h} - \nu\nabla^4 v$ where: h = local water depth, h(x) (u,v) = velocity components p = pressure ρ_o = constant fluid density μ = bottom friction coefficient ν = small biharmonic diffusion coefficient V = velocity due to wave forcing	$\eta_t + (du)_x + (dv)_y = 0,$ $u_t + uu_x + vu_y = -g\eta_x + \tilde{\tau}_x + \tau_x' - \tau_{bx},$ $v_t + uv_x + vv_y = -g\eta_y + \tilde{\tau}_y + \tau_y' - \tau_{by}$ where: η = wave-averaged free surface elevation d = h + η (u,v) = velocity components in x and y direction respectively $\tilde{\tau}_x, \tilde{\tau}_y$ = wave forcing (see below) τ_x', τ_y' = momentum mixing terms τ_{bx}, τ_{by} = bottom friction
Wave forcing and wave breaking model (ε_b)	$F = \frac{\rho_o \mu V(x,y)}{h(x)}$, where: V(x,y) is a function of $\left(\frac{\partial S_{xy}}{\partial x}\right)$ ε_b: Thornton and Guza (1986)	$\tilde{\tau}_x = -\frac{1}{\rho d}\left(\frac{\partial S_{xx}}{\partial x}\right), \tilde{\tau}_y = -\frac{1}{\rho d}\left(\frac{\partial S_{xy}}{\partial x}\right)$ ε_b: Whitford (1988)
Momentum mixing	$\nu = 1.25 m^4/s$ for 2 m grid spacing, $\nu = 2.5 m^4/s$ for 2.5 m grid spacing.	$\tau_x' = \frac{2}{d}\frac{\partial}{\partial x}\left(d\nu\frac{\partial u}{\partial x}\right) + \frac{1}{d}\frac{\partial}{\partial y}\left(d\nu\frac{\partial v}{\partial x}\right),$ $\tau_y' = \frac{1}{d}\frac{\partial}{\partial y}\left(d\nu\frac{\partial v}{\partial x}\right),$ where : $\nu = Md\left(\frac{\in_b}{\rho}\right)^{1/3}$, 0 < M < 0.5, M = mixing coefficient
Bottom friction	$\mu = C_f \lvert u_{rms}\rvert$ where: $\lvert u_{rms}\rvert \simeq 0.3$ m/s is the wave orbital velocity $0.002 \le C_f \le 0.012$	$\tau_{bx} = \frac{\mu}{d}u, \tau_{by} = \frac{\mu}{d}v$, where: $\mu = \frac{2}{\pi}c_f u_o, c_f = 0.0035, 0.003$ $u_o = \frac{1}{4}\sqrt{\frac{g\pi}{h}}H_{rms}$
Domain lengths	Lx = 1000 m Ly = 1200 or 1280 m	Lx = 550 m Ly = 16 x $L_{max,}$ where: $L_{max} = 2\pi/k_{max}$ and ranges between 160 – 200 m.
Boundary conditions	Top: Rigid-Lid Lateral: periodic Shore: $u = u_{xx} = v_x = v_{xxx} = 0$ Offshore: $u = u_{xx} = v_x = v_{xxx} = 0$	Top: Free-surface Lateral: periodic Shore: free-slip Offshore: absorbing boundary

Table 2. Quasi-3D model summary

Property	Zhao et al. (2003)
Governing equations	$\frac{\partial \overline{\zeta}}{\partial t} + \frac{\partial}{\partial x_\beta}(\tilde{V}_\beta h) = 0,$ $\frac{\partial}{\partial t}(\tilde{V}_\alpha h) + \frac{\partial}{\partial x_\beta}(\tilde{V}_\alpha \tilde{V}_\beta h) + \frac{1}{\rho}\frac{\partial S_{\beta\alpha}}{\partial x_\beta} - \frac{1}{\rho}\frac{\partial T_{\beta\alpha}}{\partial x_\beta} + \frac{1}{\rho}\frac{\partial L_{\beta\alpha}}{\partial x_\beta} + gh\frac{\partial \overline{\zeta}}{\partial x_\alpha} + \frac{\tau_\alpha^B}{\rho} = 0.$ where: $\overline{\zeta}$ = short-wave averaged free surface elevation h = still water depth α, β = are the x,y directions respectively $\tilde{V}$ = depth-uniform current $S_{\beta\alpha}$ = short-wave induced radiation stress $L_{\beta\alpha}$ = quasi-3D dispersive term $T_{\beta\alpha}$ = depth-integrated turbulent shear stress
Wave forcing	REF/DIF 1 is used as the wave driver to calculate wave radiation stresses and volume flux
Momentum mixing	$T_{\beta\alpha} = \rho h \nu_t \left(\frac{\partial \tilde{V}_\alpha}{\partial x_\beta} + \frac{\partial \tilde{V}_\beta}{\partial x_\alpha} \right)$ $L_{\beta\alpha} = \rho \left[\overline{\int_{-h_o}^{\zeta} V_{1\alpha} V_{1\beta} dz} + \overline{\int_{\zeta_t}^{\zeta} (u_{w\alpha} V_{1\beta} + u_{w\beta} V_{1\alpha}) dz} \right],$ where: $\nu_t = 0.08\sqrt{\frac{f_w}{2}} \mid u_0 \mid h + 0.1h\left(\frac{D}{\rho}\right)^{1/3} + \nu_{t,0}$ $V_{1\alpha,\beta}$ = depth-varying current u_w = wave component velocity ζ_t = free surface at the wave trough level
Bottom friction	$\tau_\alpha^B = \frac{2}{\pi} c_f \frac{\mid u_o \mid}{h} \tilde{V}_\alpha, \; c_f = 0.0035$
Boundary conditions	Top: free surface, phase-averaged Lateral: Periodic Shore: wall-boundary with free-slip condition Offshore: no-flux
Domain lengths	Lx = 788 m, Ly = 2490 m

CHAPTER 3
PROBLEM AND MODEL SETUP

The nonlinear dynamics of finite amplitude shear instabilities of alongshore currents over barred beach topography were studied using finite-difference, numerical experiments. The model was non-hydrostatic, wave phase-averaged, and fully 3D. It solved the transformed Navier-Stokes equations with a Large Eddy Simulation (LES) sub-grid scale closure on a curvilinear (σ-coordinate) grid. A principal advantage of our model was that it included dynamics of the undertow and depth varying currents that led to enhanced cross-shore mixing.

Model Domain and Solution Method

The model was formulated for alongshore-uniform bathymetry and included a shore-parallel sand bar. The depth profile was an approximate fit to topography measured at Duck, North Carolina, October 11, 1990, as part of the DELILAH field experiment (Lippmann et al., 1999) given by:

$$h(x,y) = a_1 \tanh\left(\frac{x_v b_1}{a_1}\right) + \frac{a_1}{\gamma_1}\left[\frac{x_v b_1}{a_1} - \tanh\left(\frac{x_v b_1}{a_1}\right)\right] - a_2 e^{-5\left(\frac{x_v - x_c}{x_c}\right)^2} \quad (5)$$

where:

a_1 = 2.97, defines the amplitude of the nearshore trough
a_2 = 1.5, defines the amplitude of the offshore trough
x_v = (i-1)dx, 1 < i < nx-1 where i is the cross-shore counter
$b_1 = tan(\beta_1)$, where β_1 = 0.075, defines the nearshore beach slope
$b_2 = tan(\beta_2)$, where β_2 = 0.0064, defines the offshore beach slope
$\gamma_1 = b_1/b_2$
x_c = 80, defines the cross-shore location of the nearshore bar

Two alongshore domains were used. The short alongshore domain was 20 m in length and inhibited the production of alongshore generated shear waves so we could focus on other dynamics that might have influenced the alongshore current. The large alongshore domain extended to 200 m and allowed for large-scale shear wave generation and interaction with the alongshore current.

Grid spacing was in part based upon results of Scotti et al. (1997). They found that a maximum aspect ratio between any two grid length scales of approximately 4:1 could be used for LES schemes on anisotropic grids without influencing the results. The effect of grid spacing is discussed in more detail in Chapter 4. Constraints in the grid generation scheme did not allow the depth of the cross-shore domain to go to zero, therefore the model domain was cut off at a depth of 0.5 m. The grid was clustered along the bottom and near the shoreline for higher resolution in areas of stronger variability (Figure 10). The short domain was typically modeled with (*nx, ny, nz*) = (257, 33, 17) grid points, with an average aspect ratio of 3:1 between horizontal and vertical length scales. The long domain was modeled with (*nx, ny, nz*) = (257, 257, 17) grid points and also had an average aspect ratio between the horizontal and vertical length scales of approximately 3:1.

Boundary Conditions

Uncertainties associated with the bottom friction parameterization were reduced in this approach by modeling the bottom stress with a no-slip condition using a high-resolution vertically clustered grid with O (1-10 cm) scales near the seabed. The top boundary utilized the rigid-lid approximation and was modeled with a free-slip condition. The offshore and shoreline boundaries were modeled with a no-slip condition to aid in obtaining numerical stability. The lateral boundaries were periodic.

Initial Conditions

The model was initially at rest and was forced by the momentum input from the wave radiation stresses. Run-up time to steady-state flow was approximately 1 h of real time.

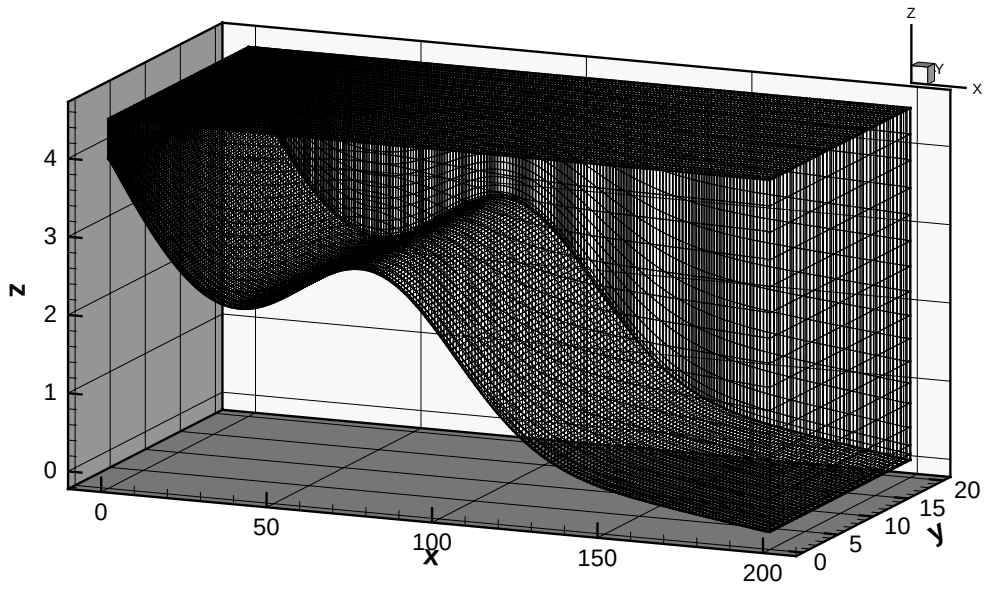

Figure 10. 3D outlay of physical grid used in the short domain simulations. (x,y,z) are the cross-shore, alongshore, and vertical axes respectively and are measured in m. The long domain extended to 200 m in the alongshore (y) direction and had the same discretization in the x-z plane.

Governing Equations

The LES equations of motion for the Cartesian coordinate system were:

$$\frac{\partial u_i}{\partial t} + u_j \frac{\partial u_i}{\partial x_j} = -\frac{1}{\rho}\frac{\partial p}{\partial x_i} + \frac{\partial \tau_{ij}}{\partial x_i} + F_{x_i}, \tag{6}$$

$$\frac{\partial u_i}{\partial x_i} = 0, \tag{7}$$

where $u_i = (u, v, w)$ were the cross-shore, alongshore, and vertical velocity components, p was pressure, t was time, ρ was fluid density equal to 1028 kg/m^3, and F_x and F_y were the horizontal body forces in the cross-shore and alongshore directions respectively and

were equal to the vertical distribution of the radiation stress gradients, $\frac{1}{\rho}\frac{\partial}{\partial x}S_{xx}$, and $\frac{1}{\rho}\frac{\partial}{\partial x}S_{xy}$. $\tau_{ij} \equiv \overline{u_i u_j} - \bar{u}_i \bar{u}_j$ represented the LES sub-grid stresses written in terms of the resolved strain tensor, $\tau_{ij} - \frac{\delta_{ij}}{3} \equiv -2\nu_t \bar{S}_{ij}$, where $\bar{S}_{ij} \equiv \frac{1}{2}\left(\frac{\partial u_i}{\partial x_j} + \frac{\partial u_j}{\partial x_i}\right)$, and the turbulent eddy viscosity, ν_t, were calculated with the Smagorinsky approach, (i.e., $\nu_t = \left(C\bar{\Delta}\right)^2 \left(2\bar{S}_{ij}\bar{S}_{ij}\right)^{1/2}$ where $C = \pi^{-1}\left(\frac{2}{3}C_k\right)^{3/4}$ and $C_k = 1.5$ was the Kolmogorov constant, and $\bar{\Delta} = (\Delta_x \Delta_y \Delta_z)^{1/3}$ was the filter width based on the local grid spacing in each direction).

The model used a boundary fitted curvilinear coordinate system that allowed variation of the geometry in two directions (x, z). To reduce the computational complexity, the model required the x-z curvilinear coordinate system to be orthogonal ($x_\xi z_\xi + x_\varsigma z_\varsigma = 0$), where the subscripts (ξ, ς) denoted partial differentiation between physical and computational space. Orthogonal grid intersection at the boundaries increased the accuracy of the boundary conditions with the interior solutions. To compute approximate solutions to the governing equations, the physical domain (*x, y, z*) that solved for the physical space velocities (*u, v, w*) was transformed to a cubic grid of regularly spaced grid points in computational space (ξ, η, ζ) and solved for the contravariant velocities (*U, v, W*). This transformation allowed the use of easily coded numerical methods, but at an increased cost of more complicated transformed equations of motion. The mapping between physical and computational space was done through an orthogonal transformation of three successive elliptic boundary value problems following

Winters et al. (2000). The bathymetry was uniform in the alongshore direction and grid spacing was constant in the y-direction.

Transformation of velocities was done by:

$$\begin{bmatrix} u \\ w \end{bmatrix} = \begin{bmatrix} x_\xi & x_\zeta \\ z_\xi & z_\zeta \end{bmatrix} \begin{bmatrix} U \\ W \end{bmatrix} \quad \text{and,} \tag{8}$$

$$\begin{bmatrix} U \\ W \end{bmatrix} = \frac{1}{J_{xz}} \begin{bmatrix} z_\zeta & -x_\zeta \\ -z_\xi & x_\xi \end{bmatrix} \begin{bmatrix} u \\ w \end{bmatrix}, \tag{9}$$

where:

$$J_{xz}(\xi,\zeta) = x_\xi z_\zeta - x_\zeta z_\xi. \tag{10}$$

Transformation of derivatives was done by:

$$\begin{bmatrix} f_x \\ f_z \end{bmatrix} = \frac{1}{J_{xz}} \begin{bmatrix} z_\zeta & -z_\xi \\ -x_\zeta & x_\xi \end{bmatrix} \begin{bmatrix} f_\xi \\ f_\zeta \end{bmatrix}. \tag{11}$$

After transformation, the governing equations to be solved were written as:

$$\frac{d}{dt}U + \beta_{1,1}U^2 + \beta_{1,2}UW + \beta_{1,3}W^2 = -\frac{1}{\rho}\frac{\left(x_\zeta^2 + z_\zeta^2\right)}{J_{xz}^2} p_\xi + \left(\frac{z_\zeta}{J_{xz}}\right) F_x + diss(U), \tag{12}$$

$$\frac{d}{dt}v = -\frac{1}{\rho} y_\eta p_\eta + F_y + diss(v), \tag{13}$$

$$\frac{d}{dt}W + \beta_{3,1}U^2 + \beta_{3,2}UW + \beta_{3,3}W^2 = -\frac{1}{\rho}\frac{\left(x_\xi^2 + z_\xi^2\right)}{J_{xz}^2} p_\zeta + \left(\frac{z_\xi}{J_{xz}}\right) F_x + diss(W), \tag{14}$$

$$D_{xz}[U,v,W] = \frac{1}{J_{xz}}\left(\frac{\partial}{\partial\xi}\left(J_{xz}U\right) + \frac{\partial}{\partial z}(J_{xz}W)\right) + \frac{1}{y_\eta}\frac{\partial}{\partial\eta}v = 0, \tag{15}$$

where:

$$\frac{d}{dt} = \frac{\partial}{\partial t} + U\frac{\partial}{\partial\xi} + \left(\frac{1}{y_\eta}\right)v\frac{\partial}{\partial\eta} + W\frac{\partial}{\partial\zeta}. \tag{16}$$

$$\beta_{1,1} = \frac{(z_\zeta x_{\xi\xi} - x_\zeta z_{\xi\xi})}{J_{xz}} \qquad \beta_{1,2} = \frac{2(z_\zeta x_{\xi\zeta} - x_\zeta z_{\xi\zeta})}{J_{xz}} \qquad \beta_{1,3} = \frac{(z_\zeta x_{\zeta\zeta} - x_\zeta z_{\zeta\zeta})}{J_{xz}}$$

$$\beta_{3,1} = \frac{(x_\xi z_{\xi\xi} - x_\zeta z_{\xi\xi})}{J_{xz}} \qquad \beta_{3,2} = \frac{2(x_\xi z_{\xi\zeta} - z_\xi x_{\xi\zeta})}{J_{xz}} \qquad \beta_{3,3} = \frac{(x_\xi z_{\zeta\zeta} - z_\xi x_{\zeta\zeta})}{J_{xz}}$$

(Winters et al., 2000)

Diss (U, v, W) were dissipation terms implemented through the LES sub-grid-scale closure model described above, and were not given here in the transformed coordinate system for simplicity. D_{xz} was the transformed divergence equation.

A fourth-order compact low pass spatial filter (Lele, 1992) was also applied to the contravariant velocity field as part of the sub-grid dissipation model to help maintain a resolved and stable simulation. Spatial derivatives were calculated with fourth-order compact differencing schemes. The pressure solver utilized a fourth-order finite difference scheme based on the multi-grid method. Time stepping was explicit and done to third-order accuracy with the Adams-Bashforth (AB3) method with a variable time step. Initial time stepping was done with the Euler and AB2 methods.

Forcing

Two-Dimensional Sub-model

The alongshore current forcing conditions were coupled to the beach topography and specified surface wave conditions using the wave refraction model of Slinn et al. (2000) that implemented the wave energy dissipation model of Thornton and Guza (1983, 1986). Deep water wave height, angle, and peak period were specified, and the waves were shoaled into the shoreline using linear theory. The majority of the effects of wave set-up were included through an induced cross-shore pressure gradient. Except for the simulation with Mellor's equations (Case 13), the depth-integrated 2D radiation stress gradients were calculated for the shoaling wave as it propagated over the beach topography. These forces were then used as input to the 3D model and distributed throughout the water column following a variety of approximations introduced in Chapter 1, and discussed in more detail immediately below. The cross-shore distribution of the nondimensionalized forcing coupled to topography used in the simulations is

presented in Figure 11. To implement the vertical distribution of radiation stresses following Mellor (2003) (Case 13), the individual wave parameters: wave energy, wave number, wave angle, and water depth were calculated at each grid point and used as input for his equations in a separate program.

Three-Dimensional Forcing Model

A variety of vertical distributions of the wave-induced radiation stress gradients were implemented to test their influence on the resulting alongshore and cross-shore current structures. Preliminary sensitivity tests of the model were performed with depth-uniform and linearly distributed forcing in both the alongshore and cross-shore directions.

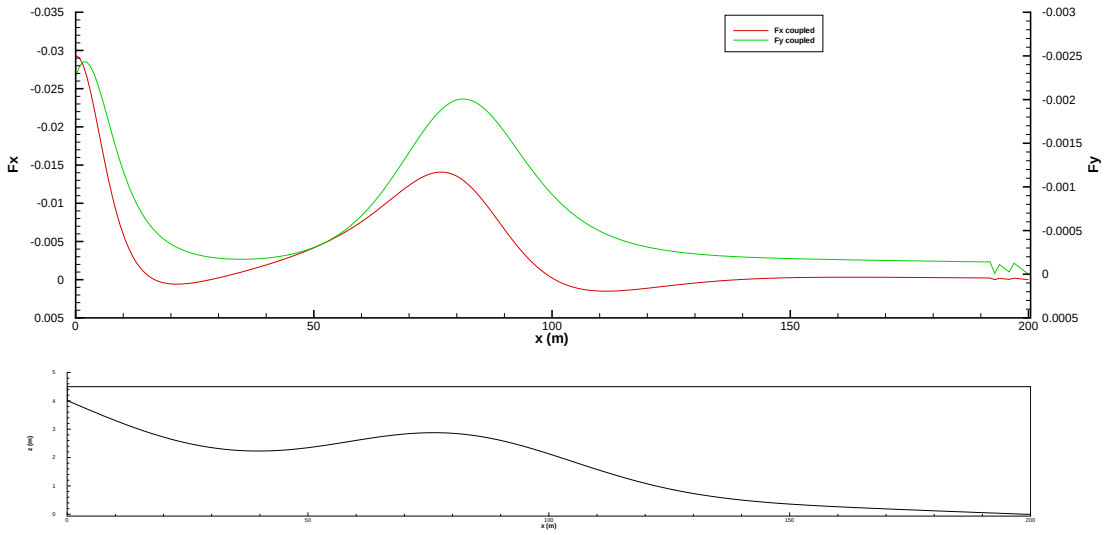

Figure 11. Cross-shore distribution of nondimensionalized wave radiation stress forcing coupled to topography. $F_x = dS_{xx}/dx$, $F_y = dS_{xy}/dx$, x = 0 is the shore boundary, x = 200 is the offshore boundary. The beach topography is given in the lower panel.

Forcing Distributions

The rigid-lid approximation used in the model represented the wave phase-averaged equations, and eliminated the vertical region between the MWL and the

wave crest. All possible vertical distributions of the radiation stresses tested were only approximations because a portion of $s_{xx}(z)$ existed in that region, not contained in any phase-averaged model. The vertical distributions were also based on linear wave theory, but applied in the surfzone that was influenced by nonlinear effects.

The vertical distribution of the cross-shore radiation stress in the surfzone was divided into two parts following Longuet-Higgins and Stewart (1964). Two-thirds of the total x-momentum forcing was distributed uniformly over the entire water column and represented the momentum due to wave orbital motion. The remaining one-third represented the excess pressure force due to the waves between the trough and crest of the wave. This portion was generally depth-dependent and various forms were implemented for the different tests. It was referred to as the pressure term. The alongshore momentum forcing, F_y, did not include the pressure term as in F_x, and was generally implemented as a depth-uniform force. The magnitude of the forcing was normalized by h(x) so that $\int F_x(x,z)dz = \frac{dS_{xx}(x)}{dx}$ and $\int F_y(x,z)dz = \frac{dS_{xy}(x)}{dx}$. In Figure 12 to Figure 17, the true direction of F_y pointed in the alongshore direction, but for graphing purposes, was presented as an onshore directed vector force above the 2D cross-shore profile.

Case 8 used a depth-uniform distribution to represent the pressure term. It was added in over the top five grid points of the domain to represent the approximate depth of the wave trough (Figure 12A). This was a first attempt to simulate the vertical distribution of wave radiation stresses due to breaking waves.

For Case 9, the pressure term was applied as a depth-linear force (increasing from zero at the bottom most point) over the top five grid points as illustrated in Figure 13A.

This forcing was a closer approximation of the vertical distribution of wave radiation stresses obtained from linear wave theory, with the approximation that the portion above the MWL was a mirror image in the vertical distribution to the portion between the trough and the MWL. It was therefore folded back on its mirror image below the MWL and doubled the force distribution in the trough to MWL region.

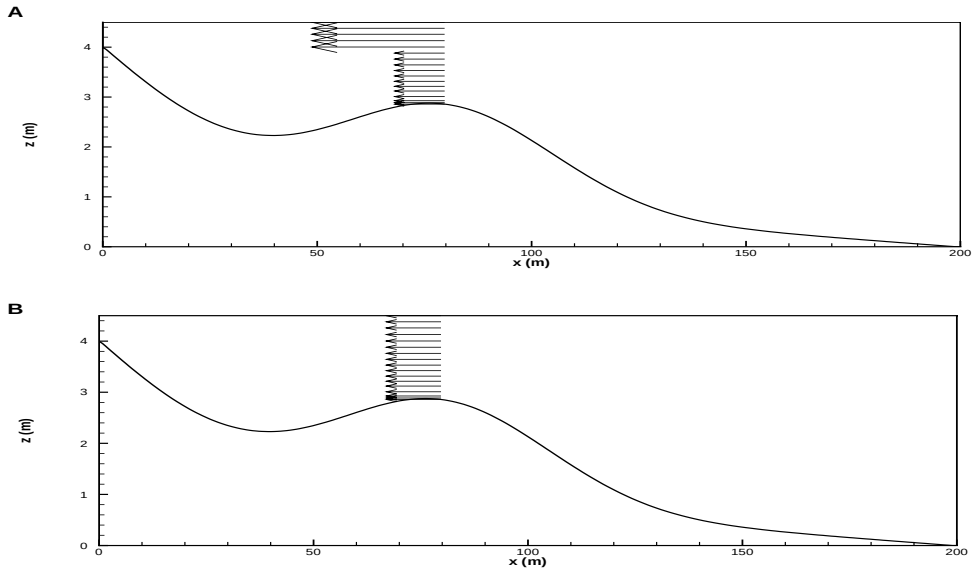

Figure 12. Case 8: Sample vertical distribution of nondimensionalized forcing. A) F_x. B) F_y. Forcing distribution was applied over the cross-shore domain and varied in magnitude according to Figure 11.

The distribution in Case 10 was another attempt to more accurately model the varying wave trough depth in the cross-shore. The σ-coordinate grid stretched to fill the water column, with grid spacing more refined in regions associated with smaller wave amplitudes. For example, over the bar crest, the wave trough depth was approximately 0.3 m and the vertical grid spacing was approximately 0.1 m. For the majority of the grid points in the cross-shore direction, the depth of the wave trough was approximately three vertical grid spaces. Case 10 had uniform forcing occurring over the top three grid points instead of five (Figure 14A).

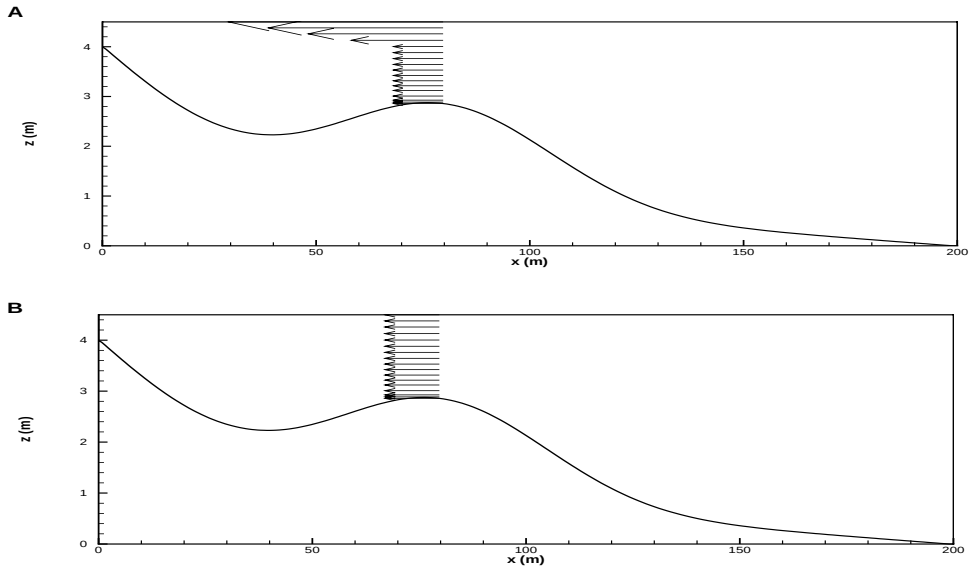

Figure 13. Case 9: Sample vertical distribution of nondimensionalized forcing. A) F_x. B) F_y. Forcing distribution was applied over the cross-shore domain and varied in magnitude according to Figure 11.

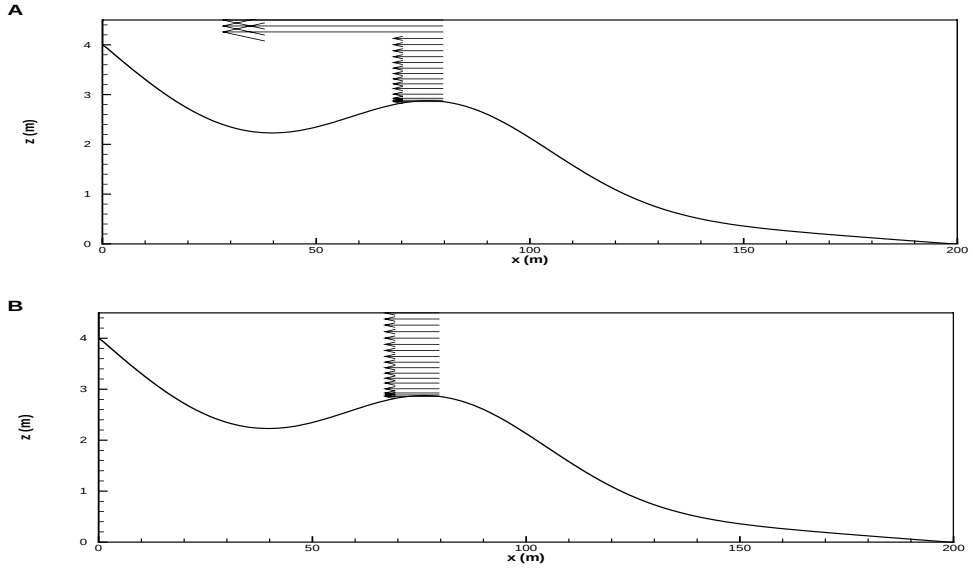

Figure 14. Case 10: Sample vertical distribution of nondimensionalized forcing. A) F_x. B) F_y. Forcing distribution was applied over the cross-shore domain and varied in magnitude according to Figure 11.

The forcing in Case 11 (Figure 15A, B) combined the linear distribution of x-momentum from Case 9, but with the linearly increasing force applied over the top three grid points (Case 10).

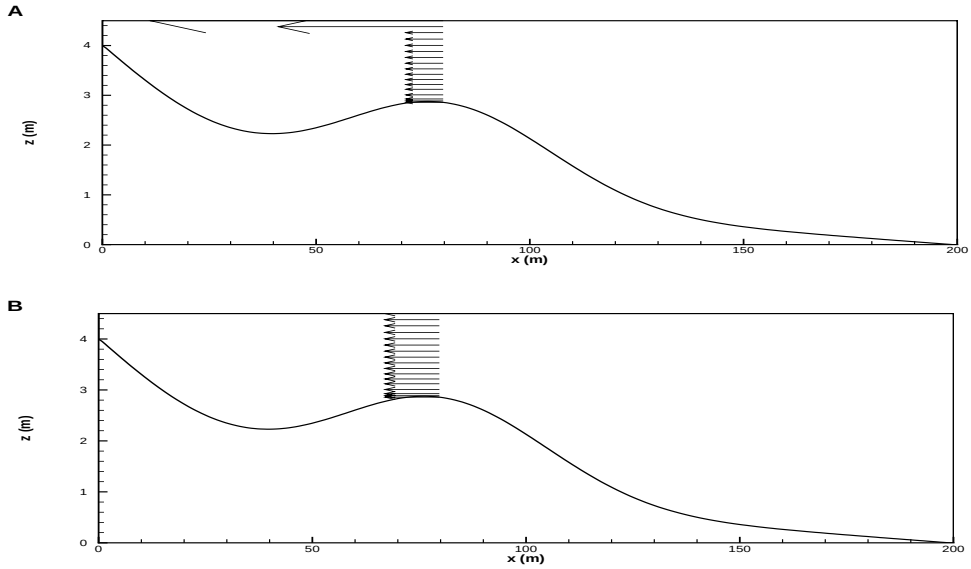

Figure 15. Case 11: Sample vertical distribution of nondimensionalized forcing. A) F_x. B) F_y. Forcing distribution was applied over the cross-shore domain and varied in magnitude according to Figure 11.

With the rigid-lid approximation used in our model, the moving free surface was removed or wave-phase averaged out. Instead of doubling the pressure term in the trough-MWL region as was done in Cases 8-11, the forcing for Case 12 was broken down into three parts: two-thirds of the total forcing was depth-uniform over the entire water column, one-sixth of the total forcing was a depth-linear force over the top three grid points, and a surface stress at the top grid point accounted for the remaining one-sixth of the total wave radiation stress force above the MWL (Figure 16A).

The forcing in Case 13 was based on the equations of Mellor (2003). As is shown in Figure 17, the vertical distribution of forcing in the x-momentum equation was quite different from the other approaches. Since Mellor's work focused on large scale,

deep-ocean modeling, his equations for the radiation stress terms might not have been a suitable description of surfzone radiation stress distributions. The full equations of momentum presented in his work, however, did account for the transfer of momentum through dissipation in other terms (Personal Communication, 2004). These other terms were not used in the current model because we focused on the cross-shore derivatives of the vertical distribution of radiation stresses only. As seen in Figure 17A, the direction of the resulting force due to radiation stress gradients in the x-direction produced variable forcing in both the vertical profile, and in direction (note at x = 125 m, the resulting force was offshore directed).

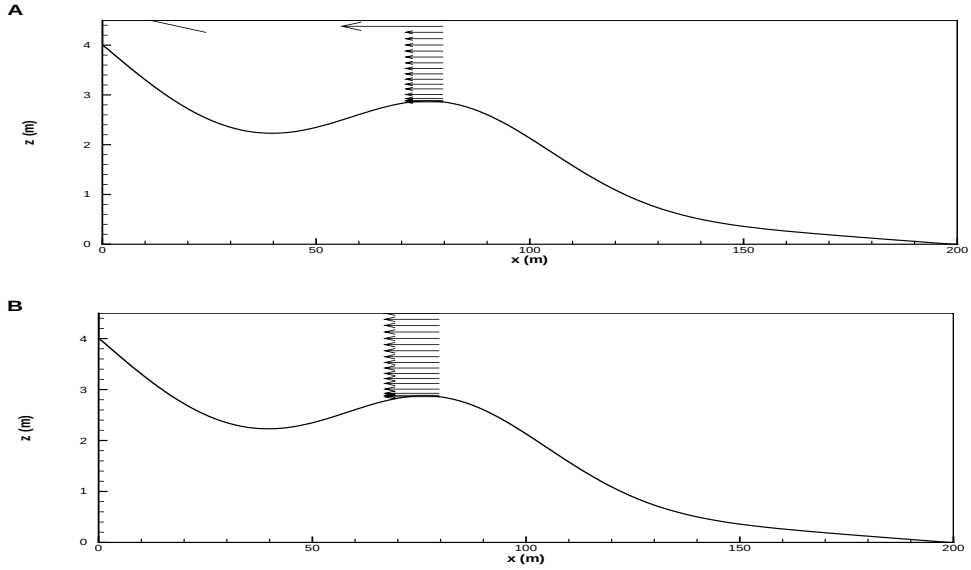

Figure 16. Case 12: Sample vertical distribution of nondimensionalized forcing. A) F_x. B) F_y. Forcing distribution was applied over the cross-shore domain and varied in magnitude according to Figure 11.

These vertical distributions of wave radiation stresses followed the basic guidance arising from linear theory. Breaking waves in the surfzone have more complex dynamics than contained in linear theory. Hence, other vertically variable distributions of F_x and F_y may be more accurate approximations of natural conditions. The vertical distribution of

radiation stresses due to nonlinear breaking waves is a topic of ongoing research. The results presented below should be considered a sensitivity study to variation of $s_{xx}(z)$ rather than as the most accurate method to model the surfzone with a 3D model.

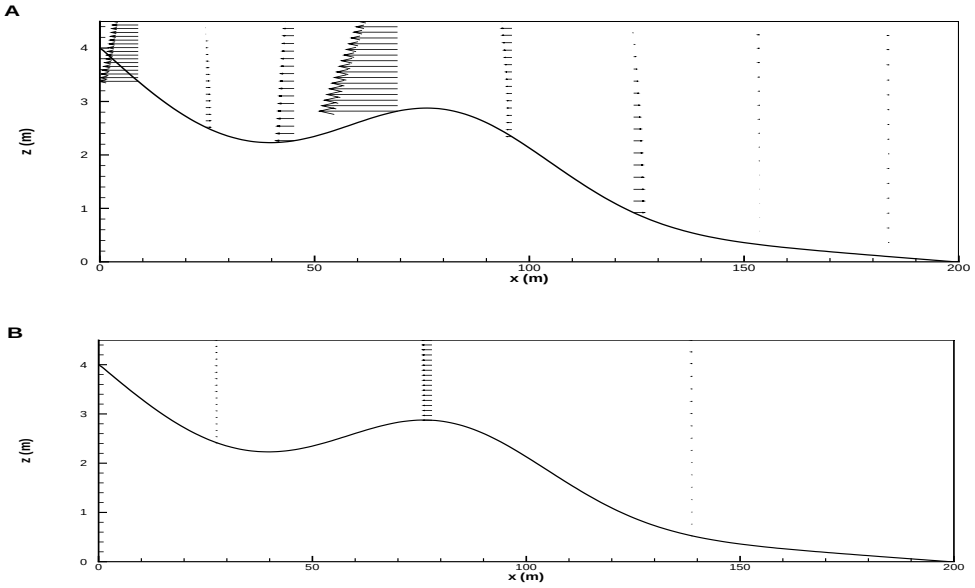

Figure 17. Case 13: Sample vertical distribution of nondimensionalized forcing. A) F_x, B) F_y. Forcing distribution was applied over the cross-shore domain.

Scope of the Model

The current model simulations pursued process-based studies concentrating on surfzone dynamics. While the model was a rational advance to investigate new physical interactions in the surfzone, it still contained several necessary approximations that limited the scope of utility of the model. Results were qualitatively and semi-quantitatively similar to field and lab data, however, several limitations inherent in the model hindered direct comparison with field data.

The surfzone is a highly dynamic area where many different physical processes interact and influence each other. The wave breaking model that was implemented is widely accepted, but was still an approximate representation of forcing. Our model did

not include the effects of mass-flux/Stoke's drift, wave-current interaction, or a wave roller, each of which would affect the quantitative predictions of the current profile. Phase averaging of the waves removed the time-variance of the forcing, and the mass-flux, and modified the total bottom drag applied to the mean currents.

The boundary conditions imposed also influenced several processes. The shoreline boundary cut-off at a depth of approximately 0.5 m was a crude approximation and influenced the inner jet region. The no-slip condition imposed for stability purposes on the cross-shore boundaries also manipulated fluid velocities in those areas. The rigid-lid approximation on the top boundary removed the MWL to crest area where a portion of the wave stresses could have been applied. Approximating this force as a surface stress was limited by the free-slip condition. Bottom friction in LES was another inelegant compromise, both because the wave component was omitted, and no wall model was used. The grid aspect ratios require further testing to increase confidence that convergence was reached and was no longer affecting the fluid dynamics. The alongshore periodic boundary conditions forced only alongshore wavelengths of integral numbers of periods to be present and did not permit features longer than the domain length to arise.

The model is in its development stages with many of the above mentioned limitations being considered. Increasing domain lengths in the alongshore and cross-shore directions will decrease boundary effects and include more of the inner jet. Increased grid resolution will improve the modeling of bottom friction and other LES effects. Higher grid resolution may also increase stability and allow for an improved representation of the free-slip boundary condition to be applied on the cross-shore

boundaries. The inclusion of mass flux and alternative methods of approximating the forces above the mean water level are currently being developed. The inclusion of a wave roller is presently available in the model if desired.

It was desired to pursue simplified process-oriented studies to isolate interactions of certain key physical processes. A consequence of this approach was that other important processes were suppressed making quantitative comparison with field data difficult. The main utility of the 3D model was the simultaneous resolution of both alongshore and cross-shore low frequency currents. Even with its inherent weaknesses and engineering approximations it was able to contribute new understanding to the dynamics of nearshore currents.

CHAPTER 4
SIMULATIONS

Sixteen cases are discussed to address the effects of grid resolution, vertically dependent forcing, and alongshore domain length. Table 3 lists the case numbers, the domain size, what was tested, and the grid used. All runs used a deepwater wave angle (α_o) of 30°, offshore boundary wave height (H_o) of 0.7 m, and peak period (T_p) of 8 s.

Table 3. Summary of simulations

Case number	Domain size (x,y) (m)	Grid resolution (nx, ny, nz)	Average aspect ratio (H:V)	Effect tested
1	(200, 198)	(129, 129, 33)	11 : 1	Vertical forcing, domain length
2	(200, 198)	(129, 129, 33)	11 : 1	Vertical forcing, domain length
3	(200, 20)	(257, 33, 33)	6 : 1	Grid resolution
4	(200, 20)	(257, 33, 17)	3 : 1	Grid resolution
5	(200, 20)	(129, 17, 33)	11 : 1	Grid resolution
6	(200, 20)	(129, 17, 17)	6 : 1	Grid resolution
7	(200, 20)	(513, 33, 33)	3 : 1	Grid resolution
8	(200, 20)	(257, 33, 17)	3 : 1	Vertical forcing
9	(200, 20)	(257, 33, 17)	3 : 1	Vertical forcing
10	(200, 20)	(257, 33, 17)	3 : 1	Vertical forcing
11	(200, 20)	(257, 33, 17)	3 : 1	Vertical forcing
12	(200, 20)	(257, 33, 17)	3 : 1	Vertical forcing
13	(200, 20)	(257, 33, 17)	3 : 1	Vertical forcing
14	(200, 198)	(257, 257, 17)	3 : 1	Domain length
15	(200, 198)	(257, 257, 17)	3 : 1	Domain length
16	(200, 198)	(257, 257, 17)	3 : 1	Domain length

Simulations were compiled using the Intel Fortran Compiler (IFC) and ran on Intel Pentium 4 (2.6 GHz) to Intel Xeon (3.06 GHz) single processors. The model was computationally expensive based on grid resolution, domain size, and forcing distribution. Depth-uniform forcing simulations ran at faster speeds because they were more stable. Cases 1 and 2 produced 60 min of data in approximately 6 weeks of CPU time. Cases 3-7 required between 4 and 12 weeks of CPU time to compute 30 min of data. Cases 8-12 averaged 9 weeks of CPU time for 60 min of data. The model could

produce results at approximate rates of 3.5 min/CPU week (Case 15 and 16) and 6 min/CPU week for Case 14 on the long domains.

The model also was run in parallel on an SGI-Origin 3400. Running a simulation in parallel on four processors decreased the computational time by approximately a factor of two compared to a single processor Intel computer. A disadvantage of the parallel platform was that batch limits were set to allow a simulation to run for a maximum of five days at a time. Thus, a simulation had to be restarted manually several times to be completed. There were additional inevitable turn-around time losses between the completion of one portion of a simulation and the next opportunity to restart it. An advantage of the dedicated single processor Intel computers was that they could be run continuously for extended periods. It could also be noted that the University of Florida, Civil and Coastal Engineering Department's 20 processor SGI Origin 3400 cost approximately $400,000 to purchase and maintain during 2001-2003, compared to single or dual processor Intel computer costs of under $2,000. The cost to benefit ratio appeared to favor the single processor platforms.

All the simulations produced reasonable velocities for the given wave parameters. Representative time series for u, v, and w- velocity are given for two locations within the surfzone. The first, at x = 80 m, was located at the bar. The second time series was taken at x = 40 m, and was situated in the middle of the bar trough. The data presented was for Case 11. Both time series were taken at mid-depth and mid-way of the alongshore domain (y = 10 m). U and w fluctuated about a mean, while the time series of v showed the spin-up and migration of the alongshore current into the trough region by the time lag between the two signals.

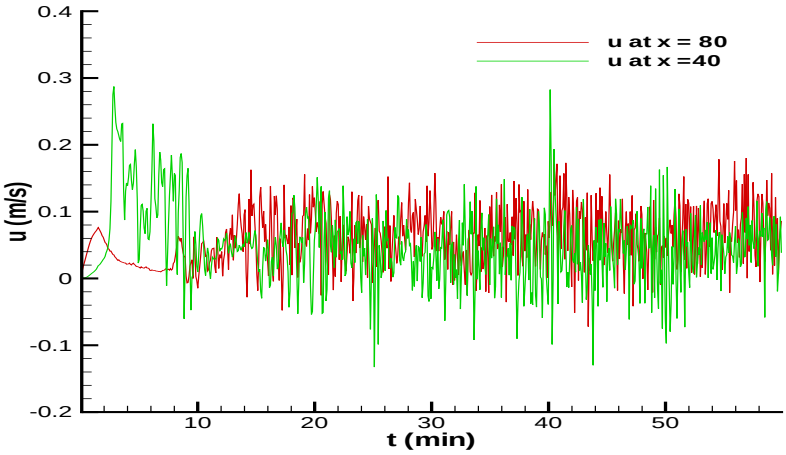

Figure 18. Time series for u-velocity. Data was from Case 11, sampled at (x_o, y_o, z_o) = (80, 10, 1.1) (red) and (x_o, y_o, z_o) = (40, 10, 1.5) (green). All co-ordinates were in m, where z_o was measured positive downwards from the top boundary.

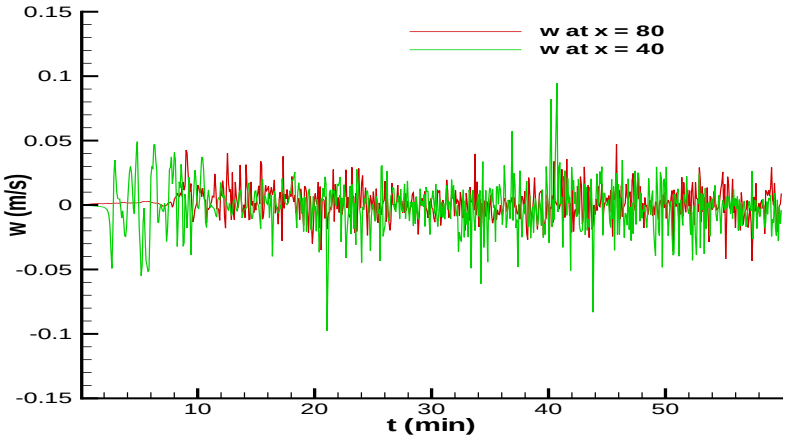

Figure 19. Time series for w-velocity. Data was from Case 11, sampled at (x_o, y_o, z_o) = (80, 10, 1.1) (red) and (x_o, y_o, z_o) = (40, 10, 1.5) (green). All co-ordinates were in m, where z_o was measured positive downwards from the top boundary.

All the simulations produced reasonable magnitudes of the mean alongshore currents for the given parameters. Since the bottom friction was modeled using a no-slip condition, ad-hoc tuning of the bottom friction coefficient (C_f) could not be done to adjust the strength of the alongshore current. In addition, with the phase-averaged model,

the bottom friction did not feel the time-varying wave bottom boundary layer where $Drag \approx C_f \vec{u}\left|u + u_w\right|$. This was significant because u_w could be relatively large. The omission of u_w produced a no-slip drag that was biased lower than field conditions. This offered one explanation for why the mean currents generated by the model might have been slightly higher than observed for the same wave conditions in the field.

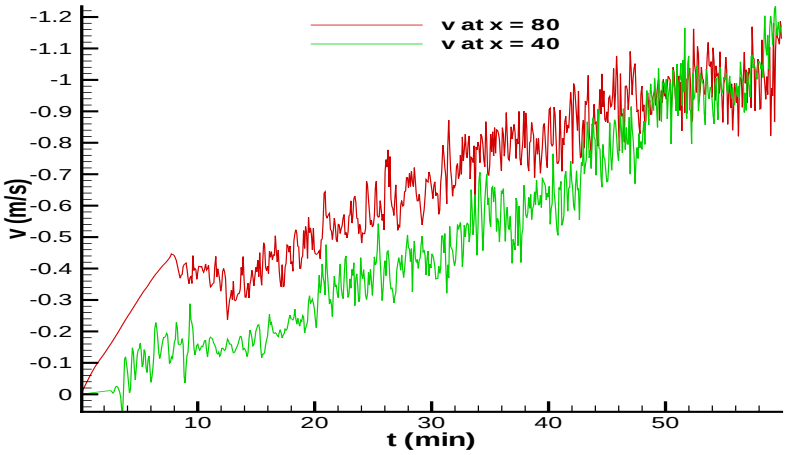

Figure 20. Time series for v-velocity. Data was from Case 11, sampled at (x_o, y_o, z_o) = (80, 10, 1.1) (red) and (x_o, y_o, z_o) = (40, 10, 1.5) (green). All co-ordinates were in m, where z_o was measured positive downwards from the top boundary.

The first simulations discussed were a comparison of forcing the model with two vertical distributions over the water column: a depth-uniform (Case 1) or a linearly depth-varying force (Case 2) (Figure 21) in both the alongshore and cross-shore directions based on Fredsoe and Deigaard (1992).

These runs produced a number of new and interesting results. First, instabilities of the alongshore current developed much sooner for depth-dependent forcing. Second, the depth-averaged current was much stronger before breaking down into instability and turbulence for depth-uniform forcing. Third, the alongshore wavelength of the initial

instabilities was longer (of order 100's of meters) for the depth-uniform current, but on the order of 10's of meters for the depth-dependent current. A comparison for the alongshore and depth-averaged alongshore currents is given in Figure 22. The strong peak currents at the shore and over the bar were present in the depth-uniform case (Figure 22A) until the current became unstable (20 min). After this time, the current laterally spread across the surfzone, but a strong current was still present at the shoreline. In Figure 22B, the depth-dependent forcing did not produce distinct alongshore current peaks over the bar, but instead the current was much weaker, and was spread across the surfzone with local maxima shoreward of the bar.

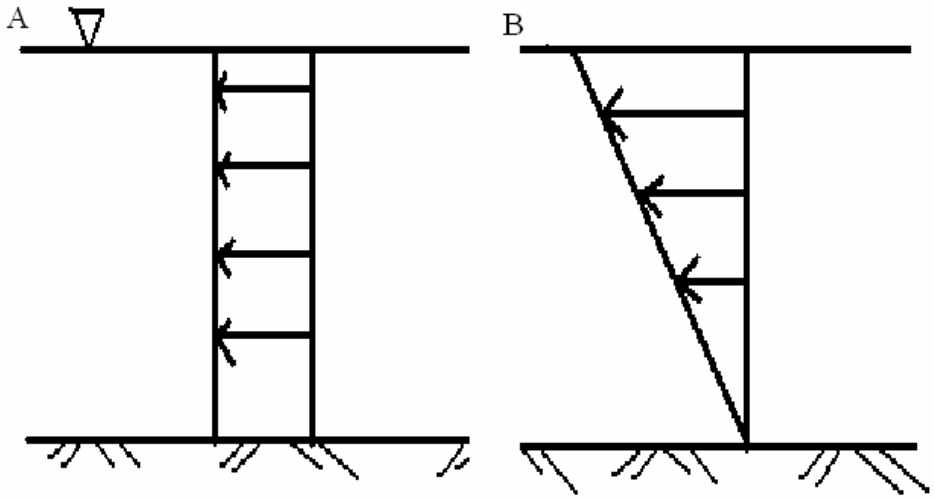

Figure 21. Case 1 and 2: Vertical distribution of forcing used in the simulations. Case 1 (A) and 2 (B).

These results showed that the response of the alongshore current was sensitive to the vertical distribution of forcing. The cross-shore distributions of the mean alongshore current profiles revealed effects of 3D mixing and preferential cross-shore advection. The physical interpretation had two major components. The first was that much stronger cross-shore circulation developed for the depth-dependent forcing. When F_x was depth-uniform, very little cross-shore circulation was produced; rather, a barotropic

cross-shore pressure gradient balanced the forcing. When F_x was depth-dependent, however, a strong undertow developed rapidly and was compensated by a shoreward mass flux in the top half of the water column (Figure 23).

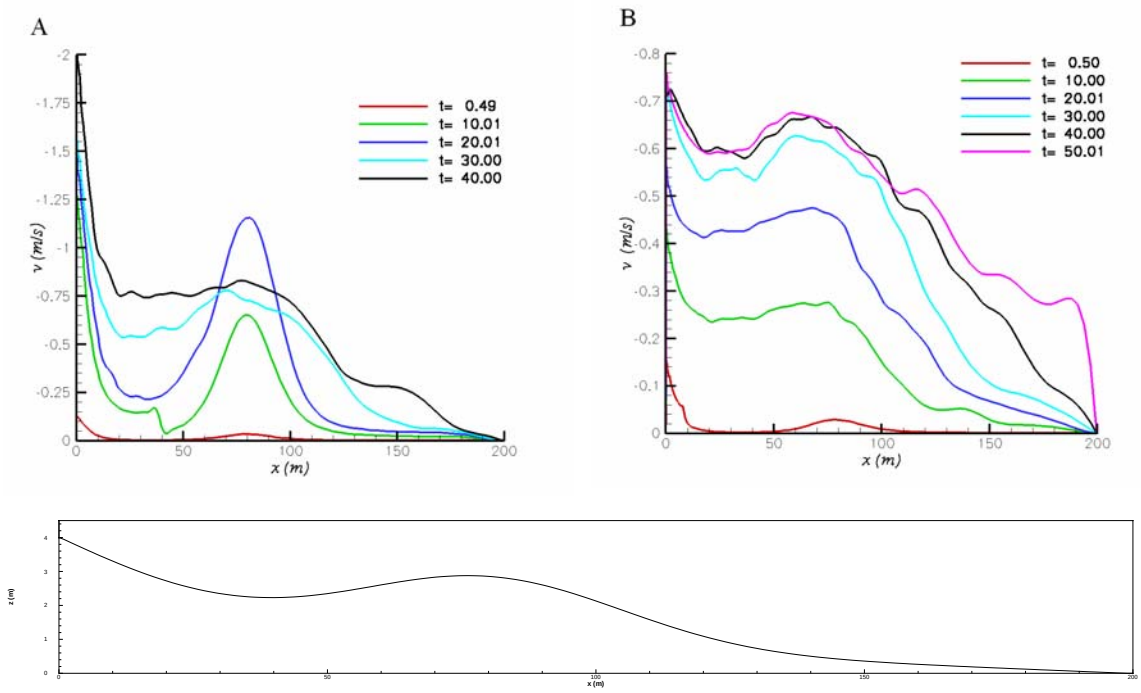

Figure 22. Comparison of depth and alongshore averaged currents for the initial simulations. A) Depth-uniform forcing, B) Depth-dependent forcing. Note: vertical axes used different scales for A and B. Bottom panel is the beach profile.

One reason this was dynamically important to the depth-averaged alongshore current was that F_y and *V(z)* were also depth-dependent in this case. This was partly due to the no-slip boundary condition on *V* at the sea bed and the free-slip condition at the surface. Hence, there was a much stronger alongshore current in the top half of the water column than in the bottom, as seen in nature. Thus, the faster surface current was advected shoreward (into the trough) while the weaker, bottom current drifted offshore. The net effect was a shoreward shift of the alongshore current maximum that became balanced in the trough. This was a similar response to having included a roller model in

the wave sub-model to shift the location of wave momentum input shoreward. A roller model was not incorporated into the formulations of the Thornton-Guza (T-G, 1983) wave breaking model that was used to generate input radiation stresses for these cases.

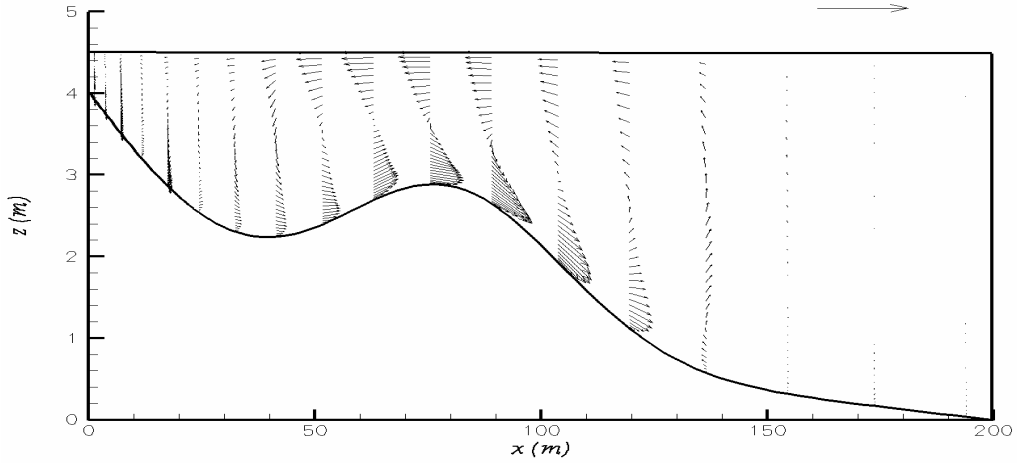

Figure 23. A typical vertical profile of cross-shore velocity vectors produced by depth linear forcing. Vectors were plotted to show the extent of the undertow along the bottom boundary. The reference vector above represented 1 grid space/unit magnitude.

The vertical distribution of forcing also affected the stability of the alongshore current. In the depth-uniform case (Figure 24), linear growth of the alongshore current produced finite large scale instabilities similar to 2D models. Depth-linear forcing (Figure 25), however, produced small-scale disturbances in the alongshore current at much earlier times.

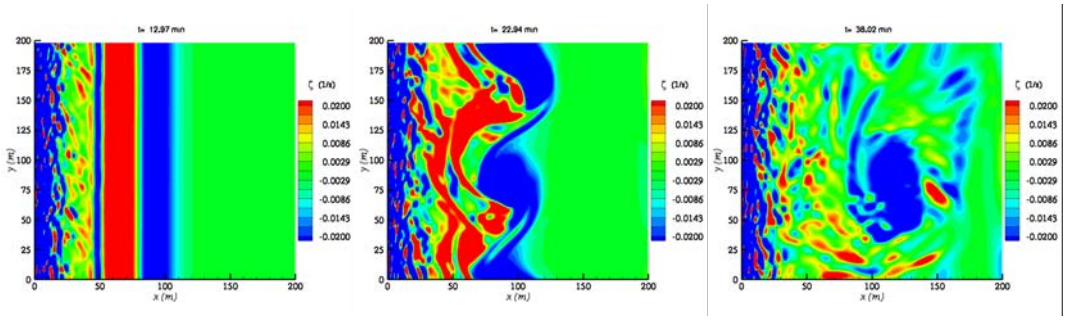

Figure 24. Surface vorticity contours for depth-uniform forcing as a function of time.

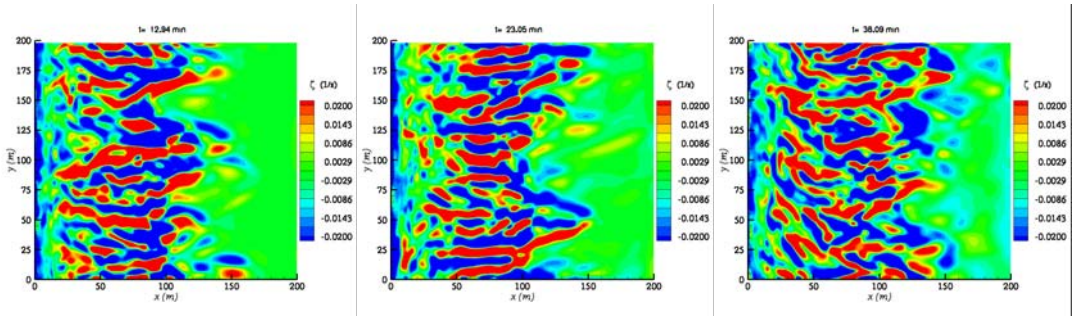

Figure 25. Surface vorticity contours for depth-dependent forcing as a function of time.

In summary, these initial simulations showed that depth-uniform forcing produced results comparable to previous 2D works. Depth-linear forcing, however, produced very different results for the vorticity structures, and provided the motivation to investigate the effects of vertical forcing and grid resolution further.

The Effect of Grid Resolution

The initial simulations were done on a grid with a high horizontal to vertical aspect ratio that exceeded the recommendations of Scotti et al. (1997) for LES closure. A series of tests were run to determine adequate grid resolution, and to verify the generality of the results. A total of five different grids were tested using depth-linear forcing as in Case 2 on a 200 m by 20 m by depth-varying grid. The 20 m domain length was used to reduce computational time, and was valid because the turbulent structures seen in Case 2 were on the order of 6 m and could be adequately captured on the smaller domain.

Case 5 had the same aspect ratio as the original tests conducted, while Case 4 followed the recommendations of Scotti et al. (1997), and Case 7 was within close proximity of his upper bound recommendation of a 4:1 grid aspect ratio. Alongshore and cross-shore currents, as well as depth-averaged vorticity fields, were compared to study grid resolution effects on flow characteristics. Each test was run to approximately 30 min.

Alongshore-Averaged Alongshore Currents

Comparing the vertical distribution of alongshore currents showed effects of the grid resolution and aspect ratio. Velocity contours comparing runs (Figure 26) showed that they were qualitatively similar to first-order observation.

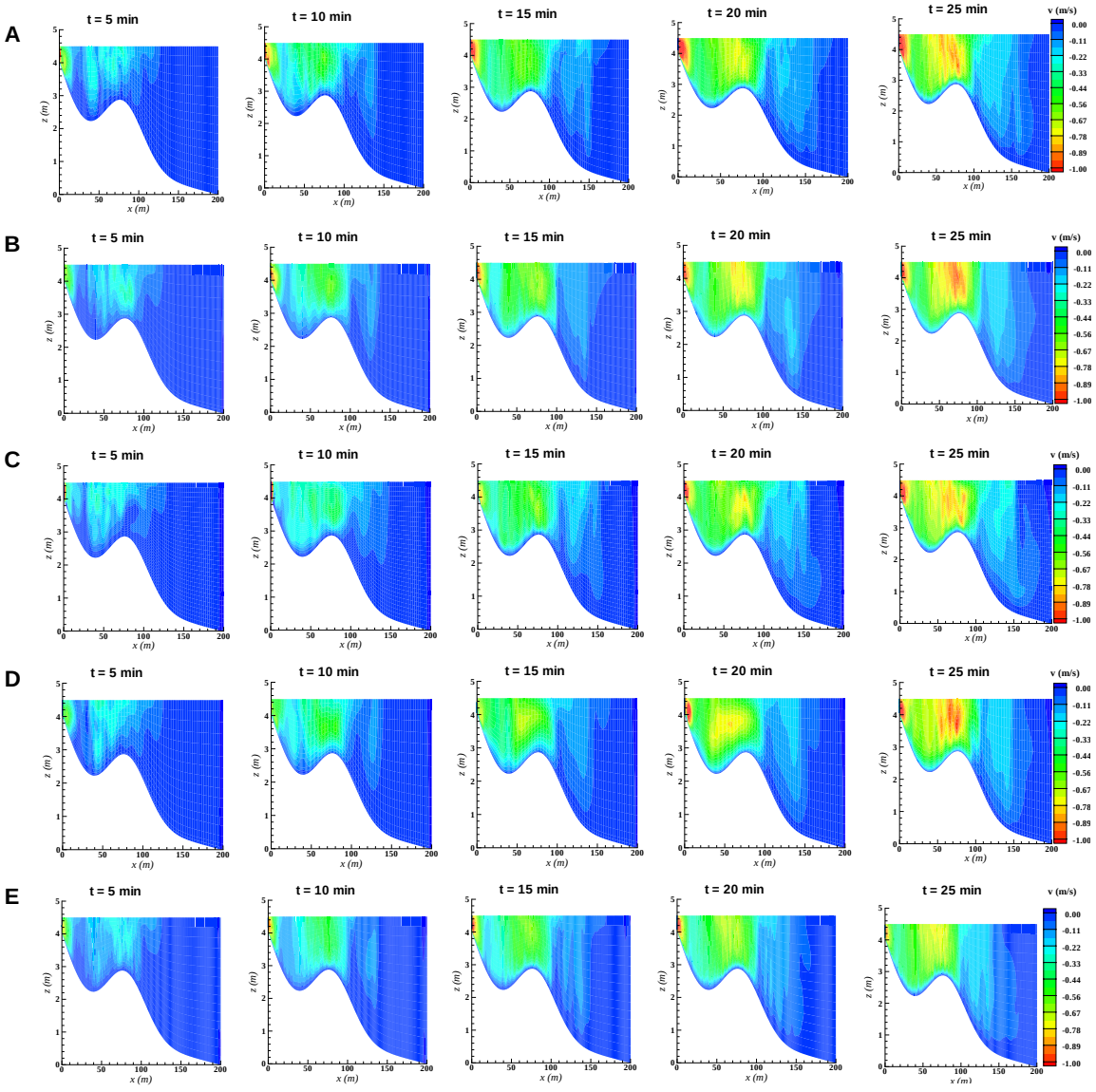

Figure 26. Cases 3-7: Contours of the alongshore-averaged alongshore velocity (v) for variable grid sizes in the x-z plane. Plots are given in 5 min intervals to show progression of current migration. A) Case 3. B) Case 4. C) Case 5. D) Case 6. E) Case 7.

The high aspect ratio grid of Case 5 showed preferential cross-shore mixing at earlier time periods. The alongshore current spread across more of the surfzone, and showed a stronger jet at the shoreline between 0 and 10 min than was present in other runs. Currents generated over the offshore bar were also weaker due to the increased lateral mixing. Case 6 produced somewhat stronger alongshore currents over the bar, and within the surfzone. Cases 3 and 4 were comparable in magnitude but varied slightly in cross-shore position. Cases 4 and 7 were comparable in cross-shore distribution but Case 7 had slightly weaker currents over the bar.

Alongshore and Depth-Averaged Alongshore Currents

The analysis of alongshore, and depth-averaged alongshore currents showed the cross-shore distribution of the current. At earlier time (Figure 27), there was little difference between the cross-shore distributions. At later times (Figure 28), however, Cases 3, 5, and 6 produced somewhat stronger alongshore currents at the bar trough and shoreline, while Cases 4 and 7 were comparable to each other.

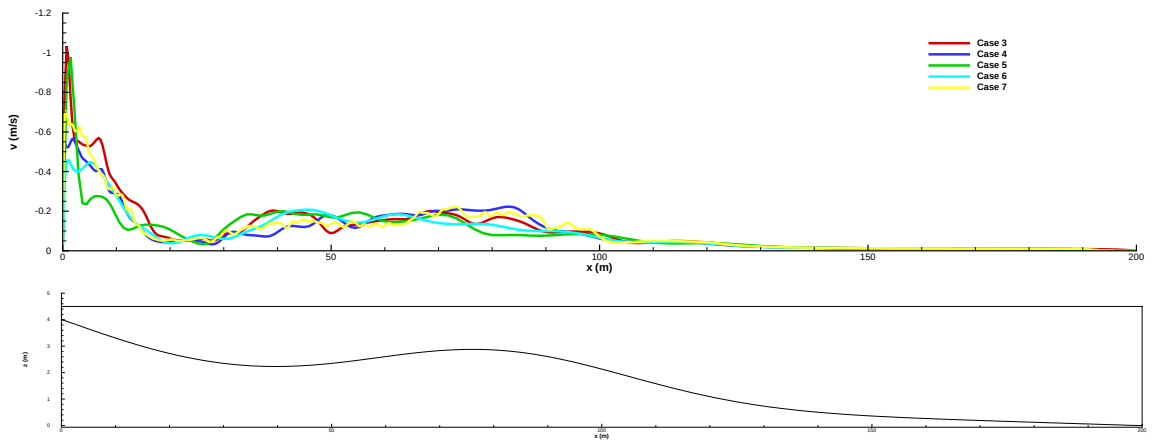

Figure 27. Depth and alongshore-averaged alongshore currents at t = 5 min.

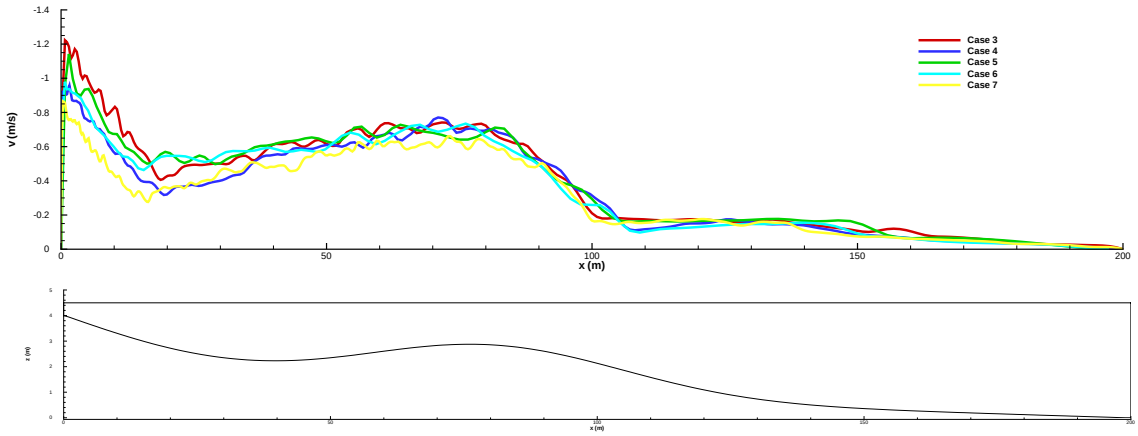

Figure 28. Depth and alongshore-averaged alongshore currents at t = 25 min.

Alongshore-Averaged Cross-shore Currents

Time, and alongshore-averaged cross-shore velocity (<*u*>, <*w*>) vector plots (Figure 29 to Figure 33) gave a qualitative feel for the cross-shore currents. The vertical axis of the grid was greatly exaggerated by approximately a factor of 40:1 compared to the horizontal scale. Therefore the direction of the velocity vectors gave a different impression of the flow depending on the manner chosen for plotting. The results were presented in two manners, but conveyed the same information. Vectors were plotted relative to grid units/magnitude scale (A), and specified the vector length as the number of grid units per unit vector magnitude, or relative to cm/magnitude scale (B) and, specified the vector length as the number of screen centimeters per unit of vector magnitude. Each option provided a different sense of the cross-shore currents. Using the vectors plotted as in A, the correct direction of the velocity vectors was given. In B, the correct magnitude was given. In both options, a reference vector equal to the relative scale was included. The grid resolution in the x-z plane varied, however, only 64 x 8 vectors were plotted to allow more space for larger vectors.

Cases 3, 5, and 6 produced stronger vertical mixing over the bar (A) as well as stronger cross-shore currents over the bar and at the shoreline (B). Case 6 had very strong downwards velocities at the shoreline. Cases 4 and 7 produced similar results. The strongest cross-shore flow occurred over the bar and along the bottom at the shoreline edge.

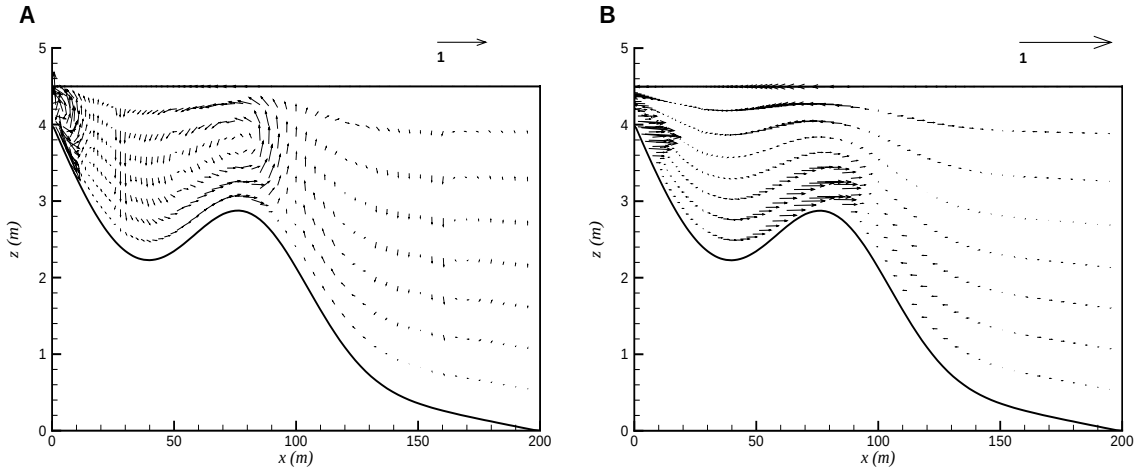

Figure 29. Case 3: Time-averaged vertical profiles in the cross-shore of the alongshore-averaged cross-shore velocity (u,w) vectors. A) relative to grid units/magnitude scale. B) relative to cm/magnitude scale.

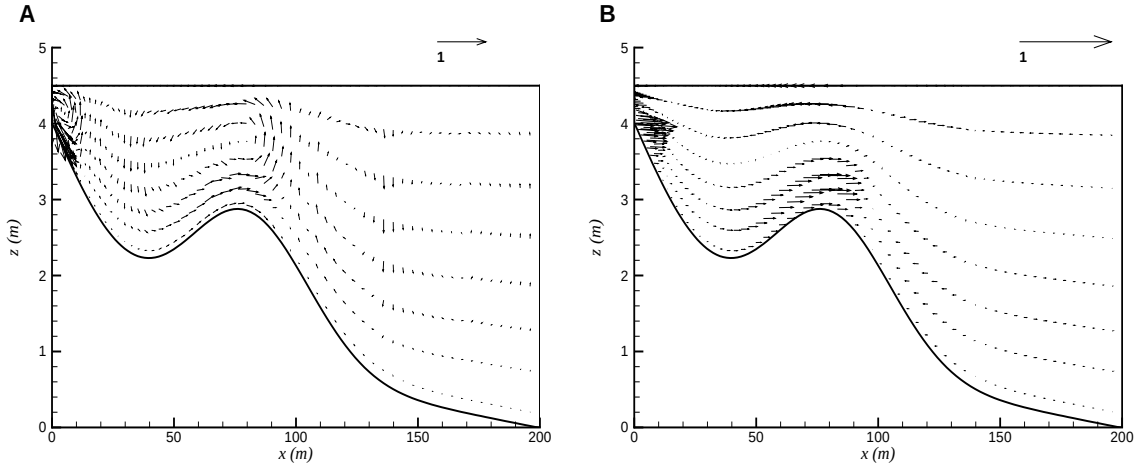

Figure 30. Case 4: Time-averaged vertical profiles in the cross-shore of the alongshore-averaged cross-shore velocity (u,w) vectors. A) relative to grid units/magnitude scale. B) relative to cm/magnitude scale.

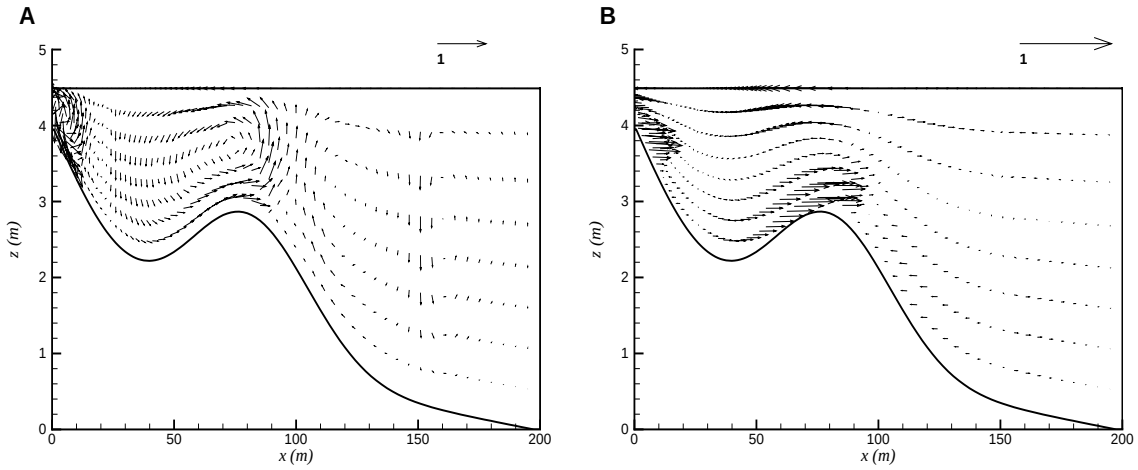

Figure 31. Case 5: Time-averaged vertical profiles in the cross-shore of the alongshore-averaged cross-shore velocity (u,w) vectors. A) relative to grid units/magnitude scale. B) relative to cm/magnitude scale.

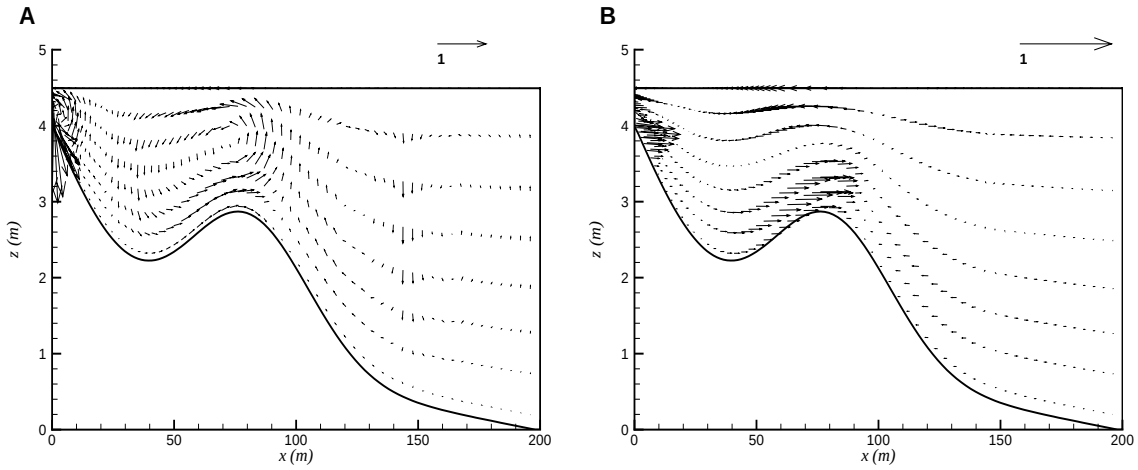

Figure 32. Case 6: Time-averaged vertical profiles in the cross-shore of the alongshore-averaged cross-shore velocity (u,w) vectors. A) relative to grid units/magnitude scale. B) relative to cm/magnitude scale.

An alternate assessment of the magnitude of cross-shore velocities was done by comparing the depth and alongshore-averaged $<u^2>$ term (Figure 34). It was clear here that the magnitude of $<u>$ was much higher (approximately a factor of 2) over the bar, and at the shoreline for Cases 5, and 6 compared to Cases 4, and 7.

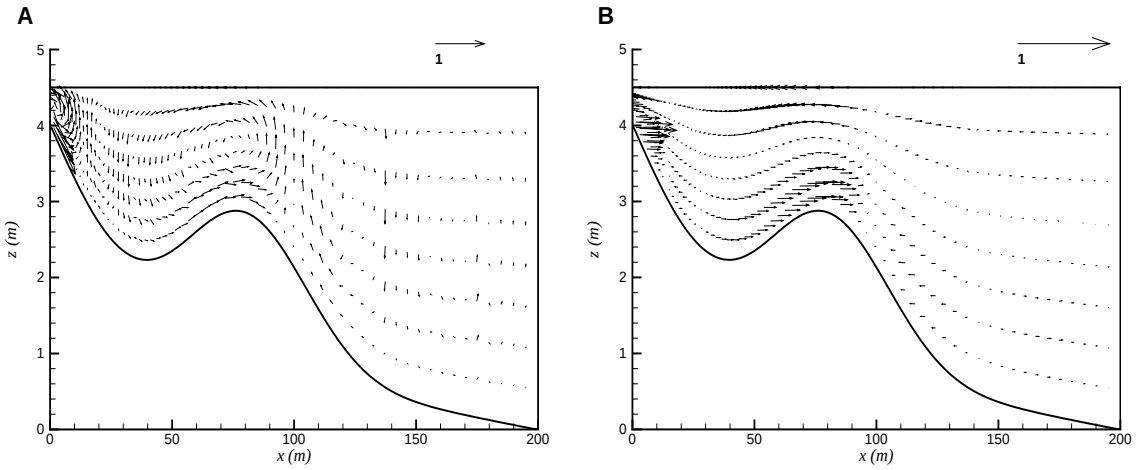

Figure 33. Case 7: Time-averaged vertical profiles in the cross-shore of the alongshore-averaged cross-shore velocity (u,w) vectors. A) relative to grid units/magnitude scale. B) relative to cm/magnitude scale.

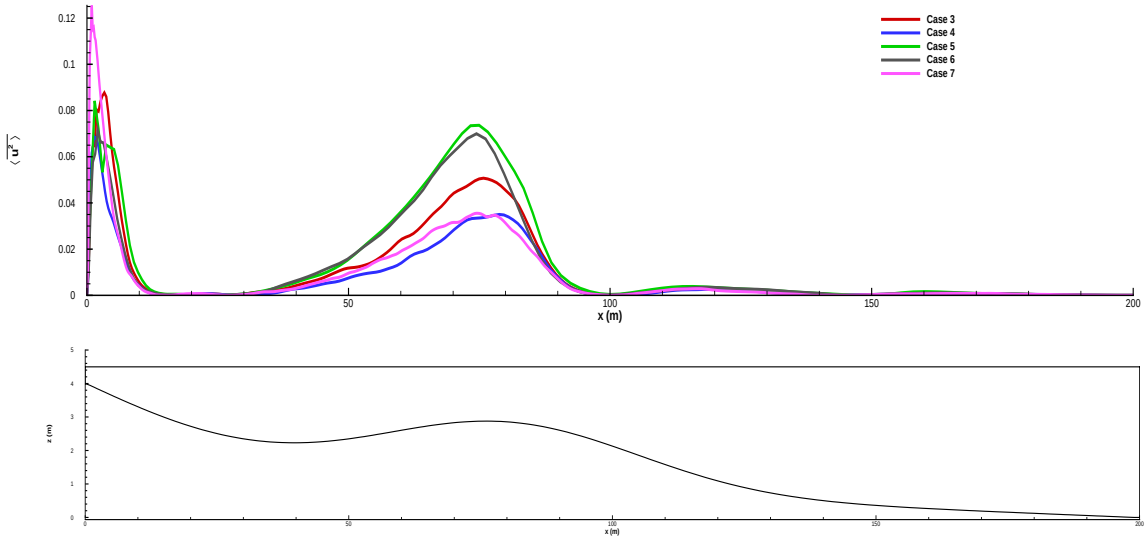

Figure 34. Comparison of the depth-averaged $\langle u^2 \rangle$ term as a function of cross-shore location.

Vorticity

Comparison of vorticity structures of all the runs showed no major differences. This led to the conclusion that the small-scale structures seen in Case 2 with depth-linear forcing were not dependent on grid resolution or aspect ratio. The results also supported

that the 3D effects produced by vertical forcing caused the highly chaotic nature of the flow, and not resolution issues related to the grid aspect ratio or LES on an anisotropic grid.

Conclusions of Grid Testing

The high aspect ratios between the horizontal and vertical length scales led to increased flow in the cross-shore direction. Case 4 was considered the best numerical experiment because it had the smallest grid aspect ratio. The error difference between Case(i) and Case 4 was defined as $Error(i) = \frac{\left[\overline{<u^2>}(i) - \overline{<u^2>}(4)\right]}{\overline{<u^2>}(4)}$, where $\overline{\langle u^2 \rangle}$ represented the depth, cross-shore, and time averaged u^2 term. The values for the error between the cases were E(3) = 0.32, E(5) = 0.66, E(6) = 0.49, E(7) = 0.13. The overall alongshore currents were more similar than the cross-shore exchanges (Figure 27, Figure 28), and the results obtained for Cases 1 and 2 were representative of results that would be obtained on higher resolution grids.

After comparing the criteria for the five simulations, the grid from Case 4 with 257 by 33 by 17 grid points was used for additional experiments on the 20 m alongshore domain. This grid fell within the recommendations given by Scotti et al. (1997) and produced characteristic flow response. Results for this grid were comparable to Case 7 that had a much higher resolution grid. It was advantageous to use the coarser grid to decrease computational time from months to weeks.

The Effect of Vertical Distribution

Based on the literature review of radiation stresses in the surfzone, a variety of vertical distributions were tested to determine the effects of depth-varying forcing on the

resulting flow structures and alongshore current (Table 3, and Chapter 3). Six distributions were tested on the small domain (*x, y, z*) = (200 m, 20 m, variable). Three distributions were tested on the large domain (*x, y, z*) = (200 m, 198 m, variable) to include effects of larger-scale alongshore current instabilities.

Cross-shore Flow

The vertical distribution of momentum forcing affected the cross-shore velocities. Stronger cross-shore flow was produced when forcing was concentrated over fewer grid points at the top of the domain (Case 8 vs. Case 10). Figure 35C and Figure 36B showed that concentrating the force over the top three grid points also pushed the peak cross-shore flow to the shoreward side of the offshore bar. Depth-linear forcing decreased cross-shore velocities when compared to depth-uniform forcing over the same number of grid points. This was an unexpected result and attributed to the free-slip condition enforced on the top boundary that set the U-velocity at the boundary by extrapolating from the four points below it at the end of each time step. The unfortunate misapplication of a shear stress at the top boundary produced alongshore currents over the bar, another effect that was attributed to the use of the incompatible free-slip boundary condition (Figure 36A). There were three cases in Table 3 that suffered from this implementation; Cases 11, 12 and 16. Cases 11 and 16 ended up putting approximately $1/5^{th}$ of the total F_x as a depth uniform force at the surface region. They were retained in the study to illustrate the influence of the long domain and shear waves on the current profile in Case 16. Mellor's equations (Figure 36C) produced an opposite cross-shore circulation pattern, with the shoreward flow along the bottom contour, and the resulting off-shore flow along the surface. Since this cross-shore circulation pattern was contrary to field and laboratory observations, his equations weren't considered useful

under these circumstances, and were not pursued further in our study. In Figure 35C, the strongest currents were slightly shoreward. In Figure 36C, the currents were weaker and opposite in direction, with the onshore flow (blue) along the bottom and the off-shore directed flow (red) along the top boundary.

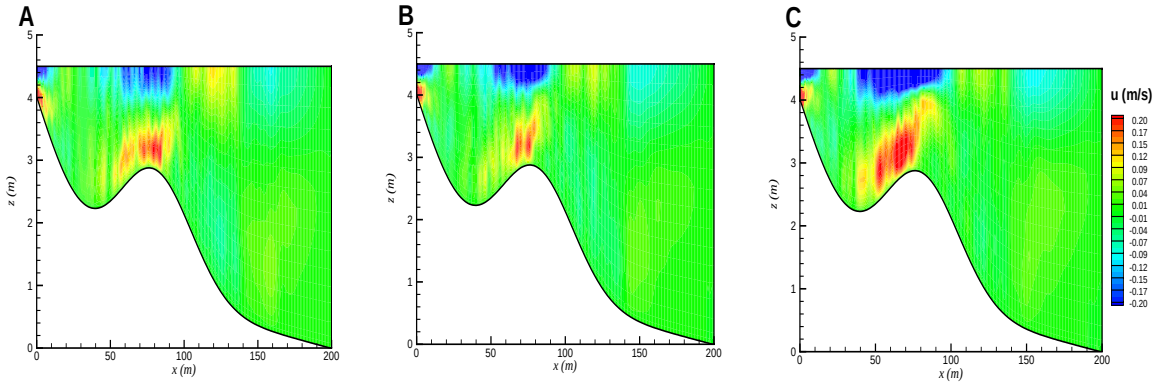

Figure 35. Cases 8-10: Comparison of alongshore and time-averaged u-velocity as a function of depth and location in the cross-shore domain. A) Case 8. B) Case 9. C) Case 10. The dark blue contours indicate strong on-shore flow and the red contours represent the off-shore directed undertow.

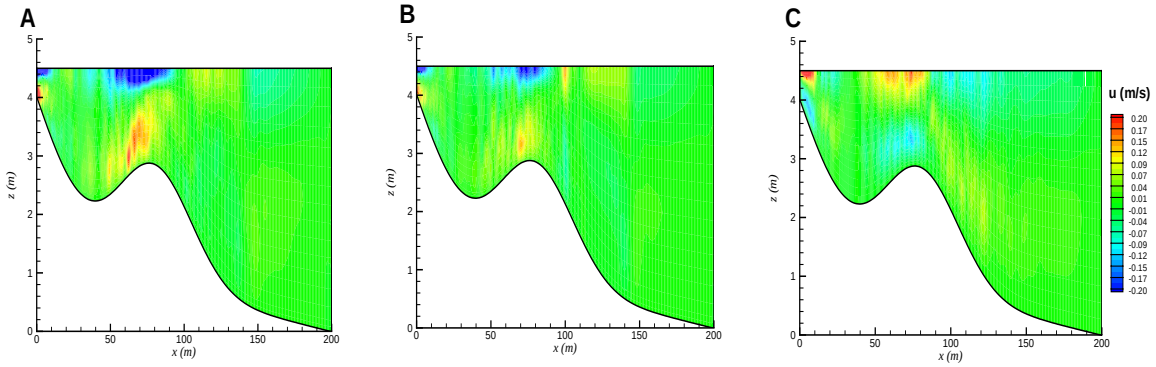

Figure 36. Cases 11-13: Comparison of alongshore and time-averaged u-velocity as a function of depth and location in the cross-shore domain. A) Case 11. B) Case 12. C) Case 13. The dark blue contours in A and B indicate strong on-shore flow and the red contours represent the off-shore directed undertow.

Another aspect of the influence of cross-shore mixing on currents was the effect of vertical mixing. Various 2D and 3D models have assumed hydrostatic flow (u >> w),

which was a valid approximation resulting in predominantly 2D (x-y) currents. The vertical velocities (w), however, were actually greater than u in various positions of the cross-shore, especially off-shore of the bar. These vertical currents resembled the strong vertical mixing in vortex trains seen by Li and Dalrymple (1998) (Figure 37). The non-hydrostatic approach in the 3D model produced similar vertical eddies offshore of the bar, with the ratio of u:w in the range of 0.5 at some locations (Figure 38 and Figure 39). Vertical mixing was significant, and a non-hydrostatic model was necessary to produce that type of cross-shore current and mixing.

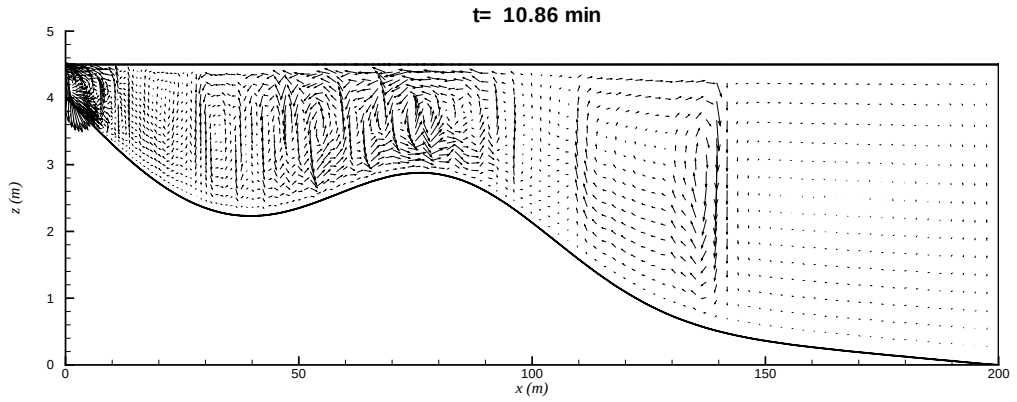

Figure 37. Vector plot of alongshore-averaged u-w velocities for Case 7. u:w = 0.5 at (x_o, z_o) = (138 m, 3.2 m).

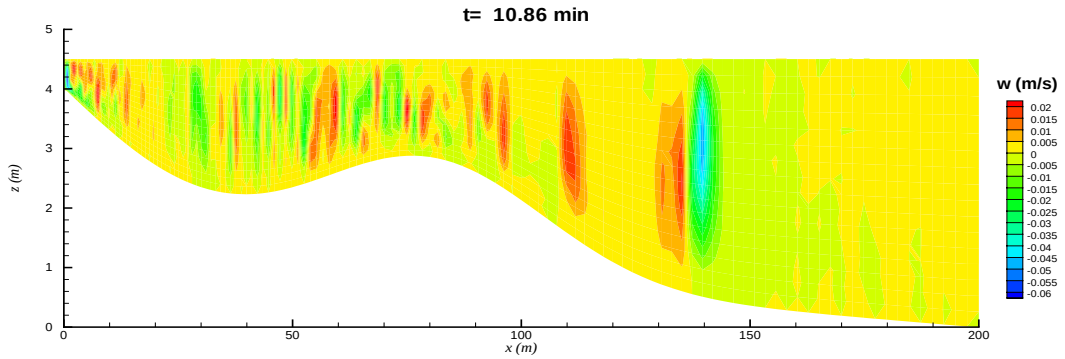

Figure 38. Alongshore-averaged w-velocity contours for Case 7, t = 10.86 min. Red contours indicate upwards flow. Blue contours represent a downwards directed velocity.

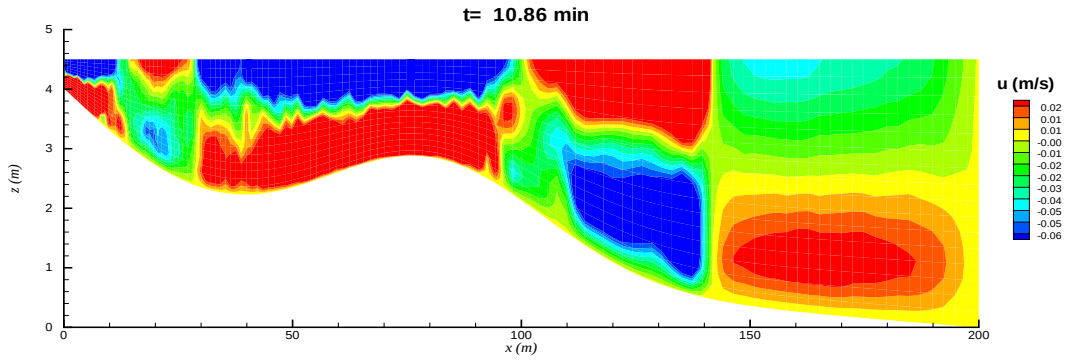

Figure 39. Alongshore-averaged u-velocity contours for Case 7, t = 10.86 min. Red contours represent offshore velocity and blue represent onshore directed velocity.

Alongshore Currents

Each forcing distribution influenced the alongshore current to some degree. Each distribution consisted of depth-uniform y-momentum forcing, and had two-thirds of the x-momentum inputted as a depth-uniform force. The remaining one-third of the total x-momentum was varied in the five runs. It was primarily this portion that affected the cross-shore current, and the eventual location of the alongshore current maximum. When a force was located over a smaller vertical area, the alongshore current was spread further into the trough. A depth-uniform distribution, compared to a depth-linear distribution, (Figure 42 vs. Figure 43) also pushed the alongshore current further into the trough. The depth-linear forcing produced stronger currents at the shoreline (approximately 40 to 50%) and over the bar (5 to 10%) (Figure 43) compared to the depth-uniform distribution (Figure 42). Applying a shear stress at the top (Figure 44) produced strong currents at the shoreline, and reduced spreading of the current across the surfzone.

Figure 40 to Figure 44 show the cross-shore distribution of the alongshore, and depth-averaged alongshore current over time for the five cases. By 60 min, the current

over the bar had begun to stabilize while the current in the trough was still increasing. The shoreward shift of the peak alongshore current was compared for the five runs in Figure 45. The apparent noise of the alongshore current was due to the small alongshore domain length that the currents were averaged over. Over longer domain lengths, the currents had a smoother profile because the small-scale instabilities were averaged over a larger scale.

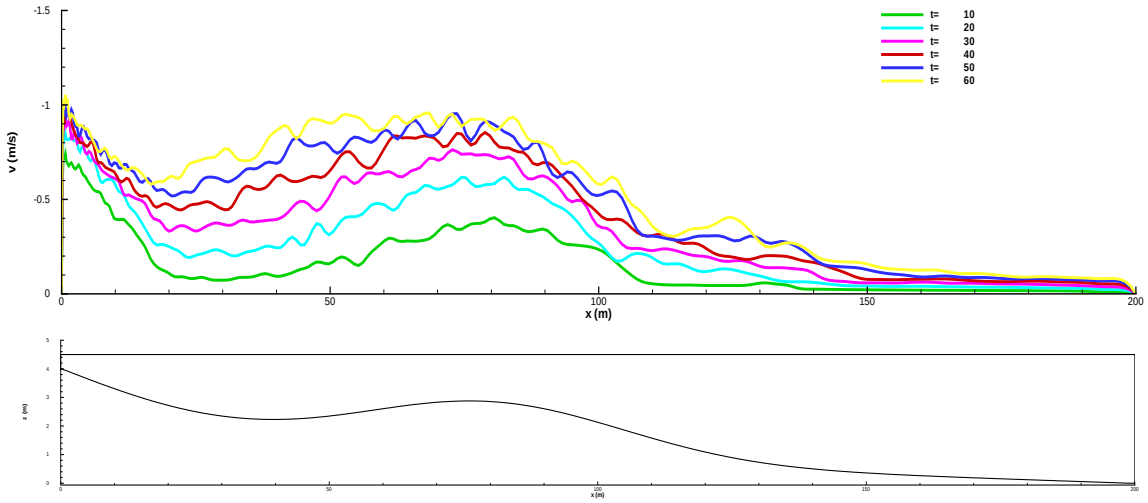

Figure 40. Case 8: Cross-shore distribution of the alongshore and depth-averaged alongshore current over a 60 min time period. Time progression shows the migration of the current shoreward of the bar (x = 80 m).

By 60 min, the peak alongshore current at the shoreline seen in Cases 8 and 9 was not visible in Case 10. The current was more uniform in the cross-shore. Concentrating the forcing over fewer grid points at the surface had smoothed out the current. The peak velocity remained around 1 m/s.

Time progression showed the migration of the current shoreward of the bar (x = 80 m) for Case 11. By 60 min, the current over the bar had begun to stabilize while the current in the trough was still increasing. A distinct peak still existed at the shoreline.

Time progression showed the current did not migrate substantially shoreward of the bar, with distinct peaks at the shoreline, and over the bar for Case 12. By 60 min, the current over the bar was starting to stabilize while the current in the trough was still increasing. Peak velocities exceeded 1 m/s.

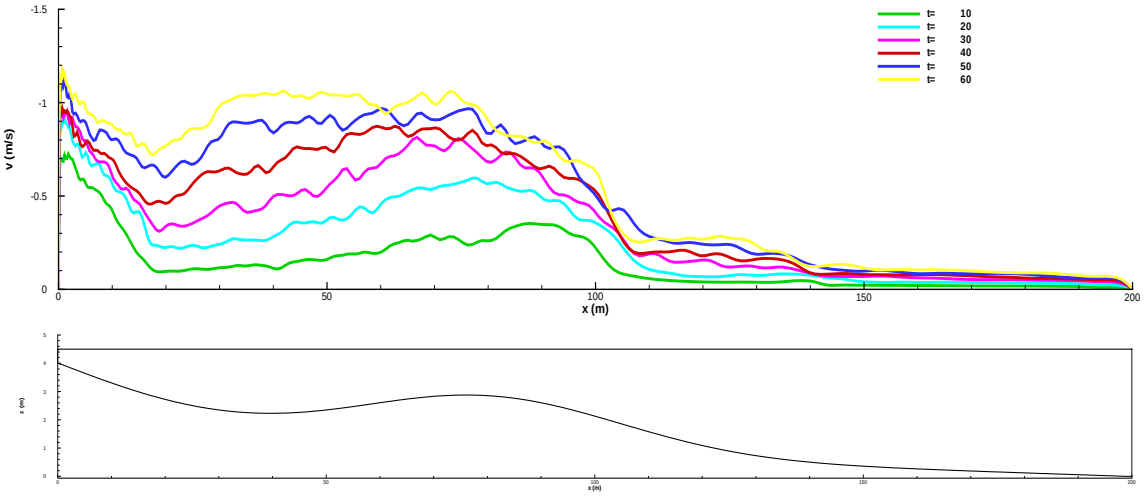

Figure 41. Case 9: Cross-shore distribution of the alongshore and depth-averaged alongshore current over a 60 min time period. Time progression showed the migration of the current shoreward of the bar (x = 80 m).

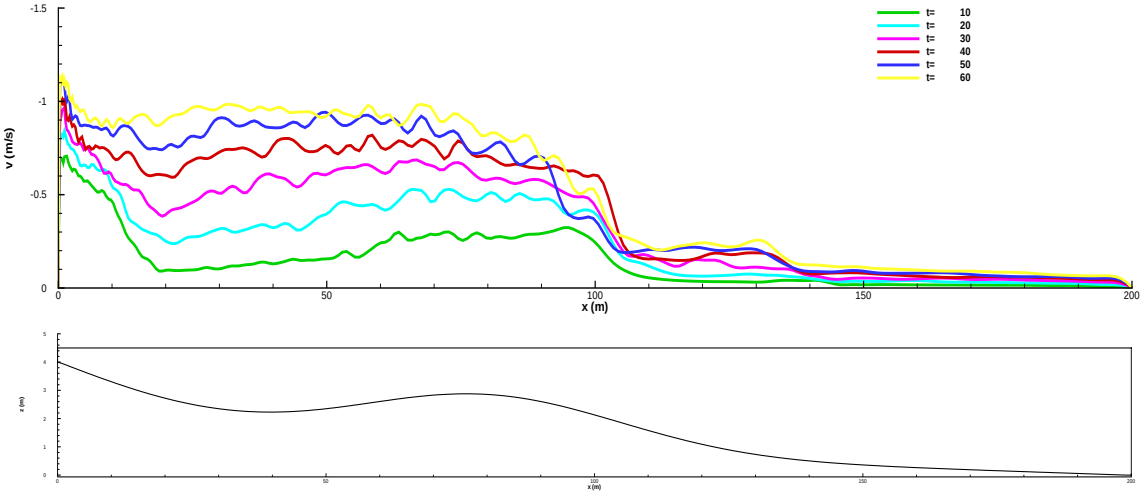

Figure 42. Case 10: Cross-shore distribution of the alongshore and depth-averaged alongshore current over a 60 min time period. Time progression showed the migration of the current shoreward of the bar (x = 80 m).

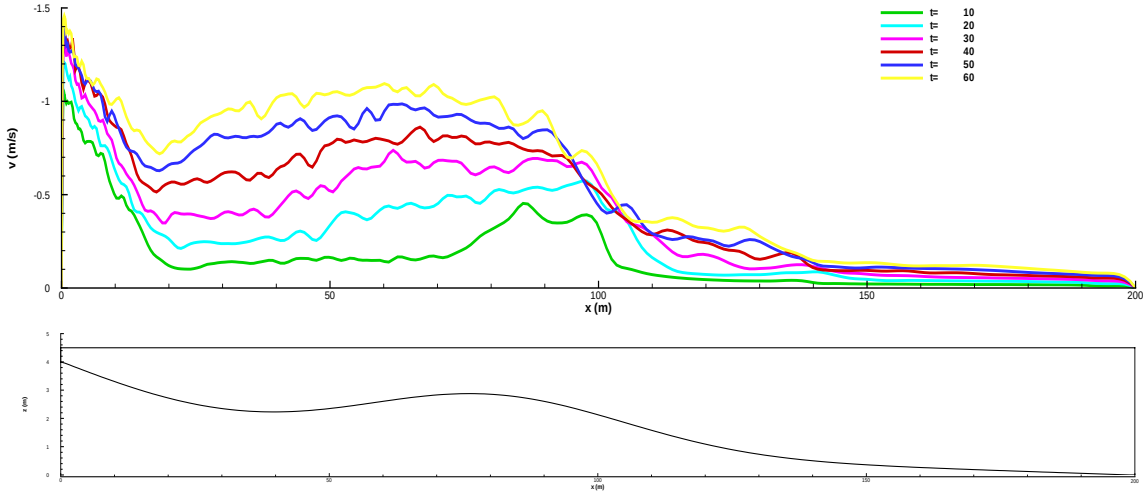

Figure 43. Case 11: Cross-shore distribution of the alongshore and depth-averaged alongshore current over a 60 min time period.

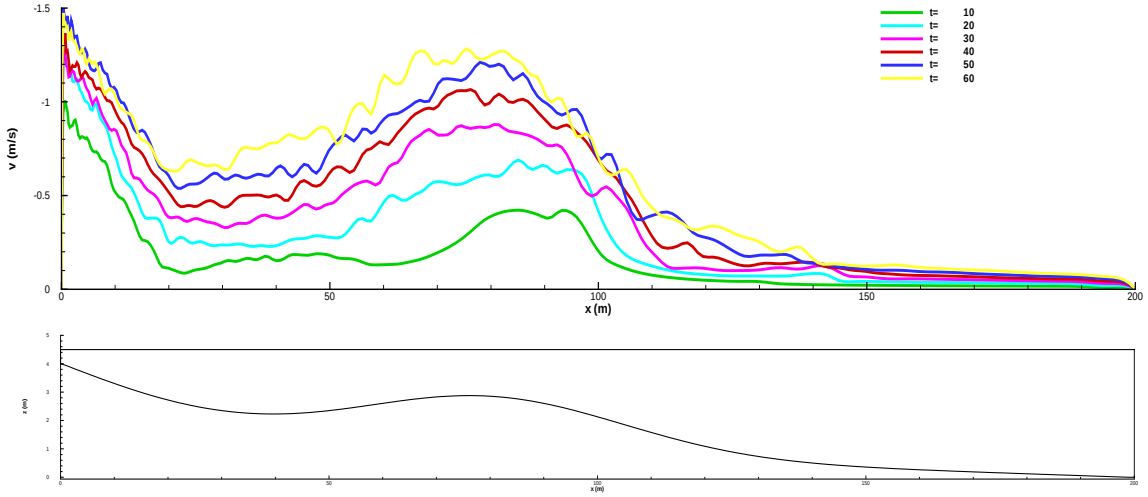

Figure 44. Case 12: Cross-shore distribution of the alongshore and depth-averaged alongshore current over a 60 min time period.

The results of the alongshore and depth-averaged alongshore currents showed the influence of 3D forcing. Since the forcing was not entirely depth uniform in the x-direction, the alongshore momentum located over the bar was advected shoreward into the trough, without the influence of large-scale shear instabilities or a surface roller. The most effective form of cross-shore spreading of the alongshore current was produced by

Case 10 (Figure 45, Figure 46). Comparison of the depth-averaged current showed the migration of the peak from over the bar into the trough (Figure 45).

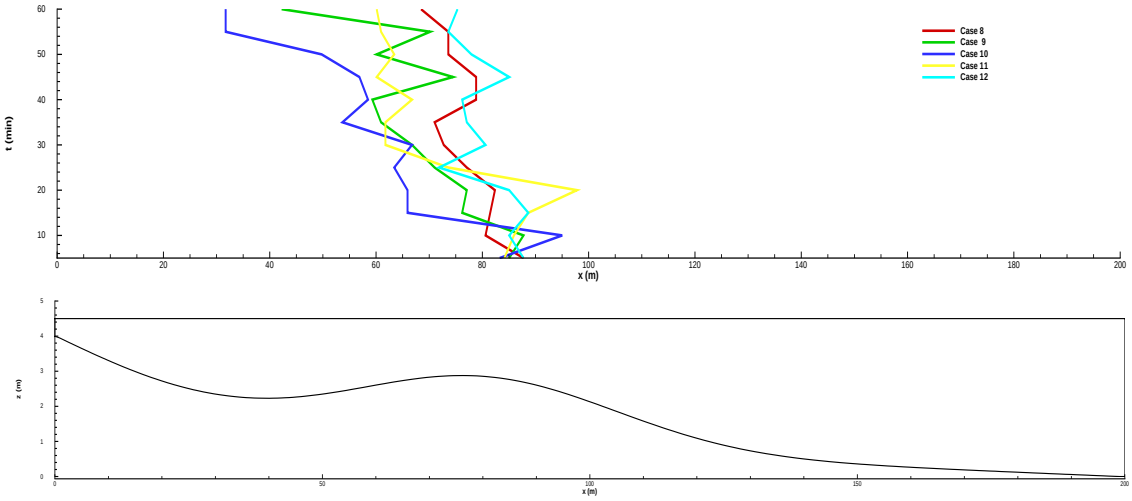

Figure 45. Cross-shore position as a function of time of the peak alongshore current for the 5 vertical distsributions tested.

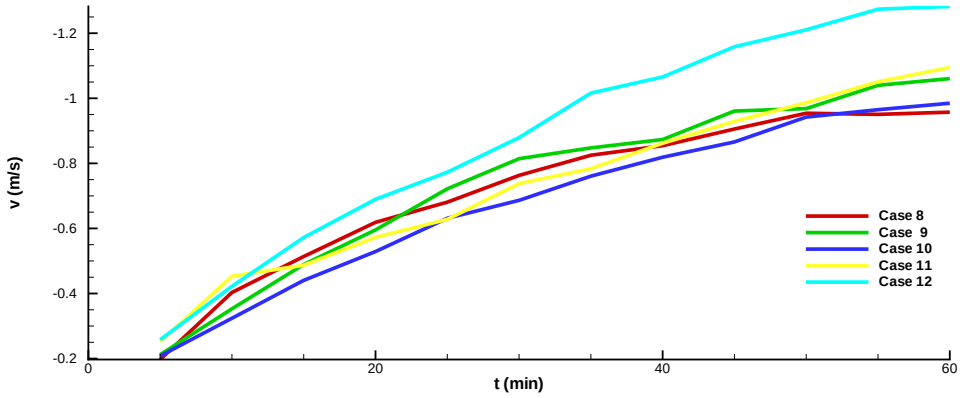

Figure 46. Peak velocity of the alongshore current as a function of time.

To better understand the differences caused by the vertical forcing, the vertical distribution of the alongshore current was studied. Figure 47 to Figure 50 compared the effects of vertical forcing on the alongshore current over a 60 min interval for each run. In each plot, a boundary layer existed along the bottom (light blue) where the alongshore

current was insignificant. This coincided with the areas of stronger cross-shore currents. Peak currents occurred slightly below the surface (darker yellow and red areas).

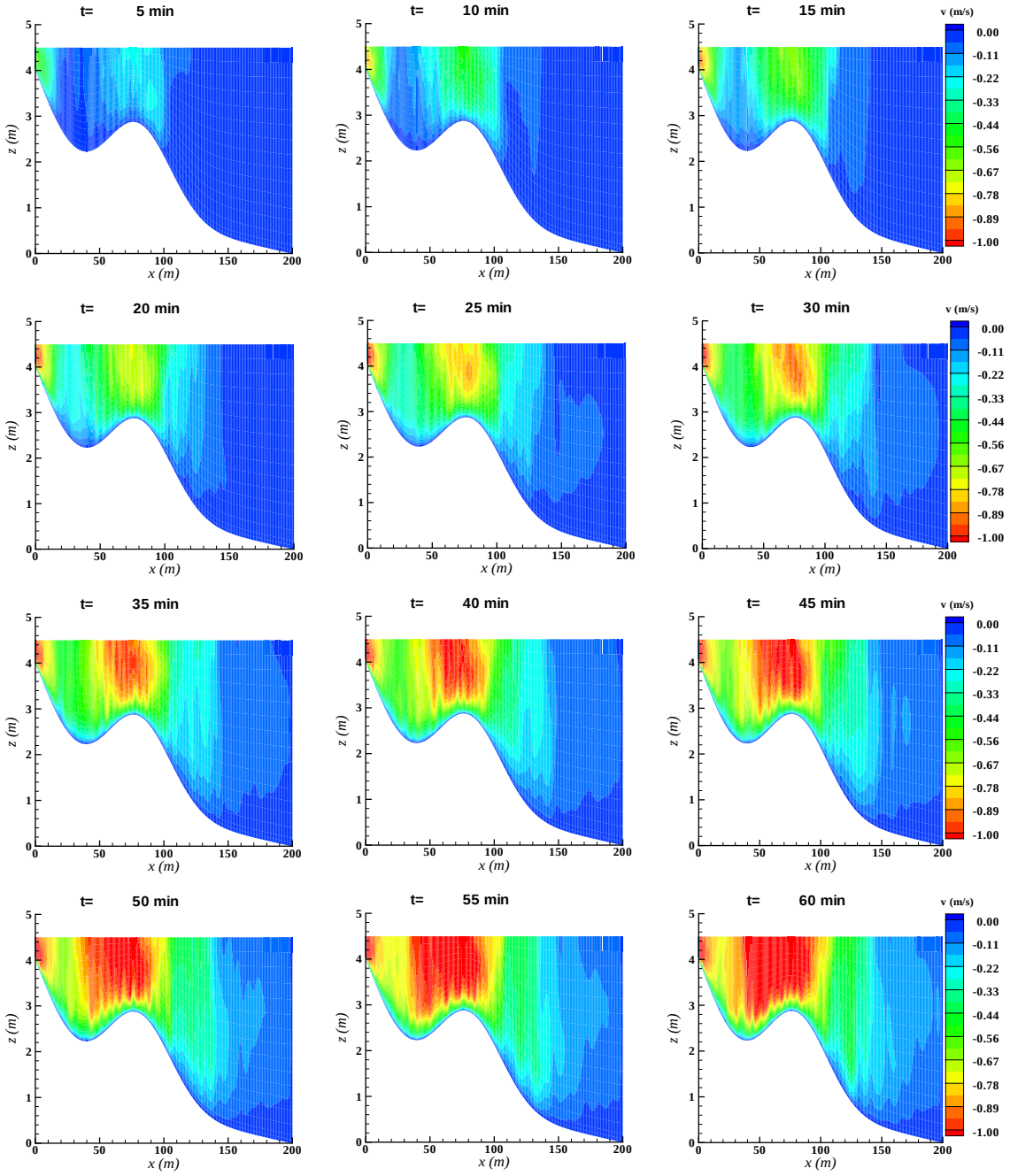

Figure 47. Case 8: Vertical cross-section contour plots of the alongshore-averaged alongshore current (v). Time progression at 5 min intervals showed the migration of the current over the bar into the trough area.

In Figure 48, peak alongshore currents (red) were stronger over the same time intervals compared to Figure 47.

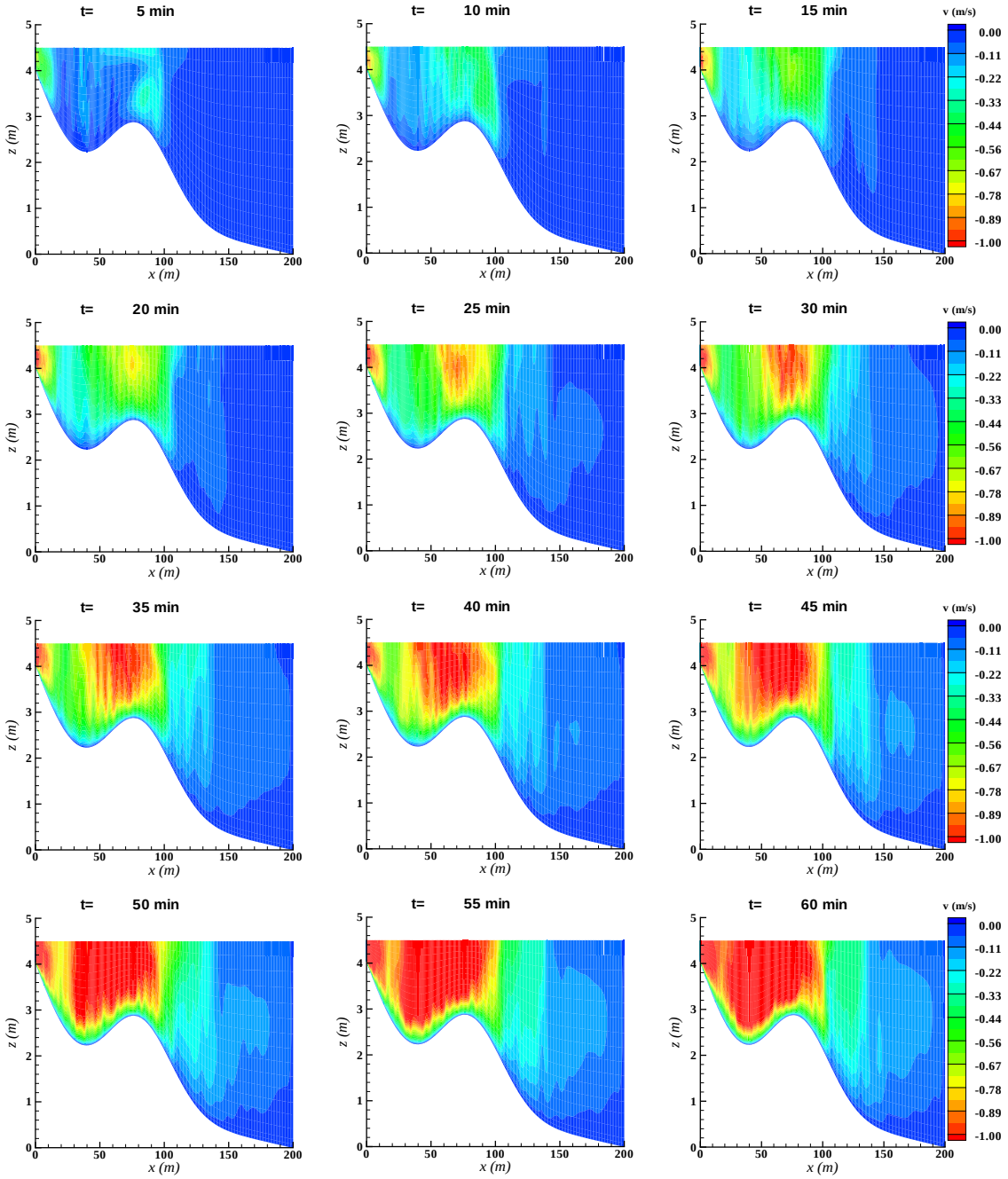

Figure 48. Case 9: Vertical cross-section contour plots of the alongshore-averaged alongshore current (v). Time progression at 5 min intervals showed the migration of the current over the bar into the trough area.

In Figure 49, a boundary layer along the bottom (light blue) existed. The alongshore current was weaker, and more spread out in the cross-shore over the same time periods for the other examples.

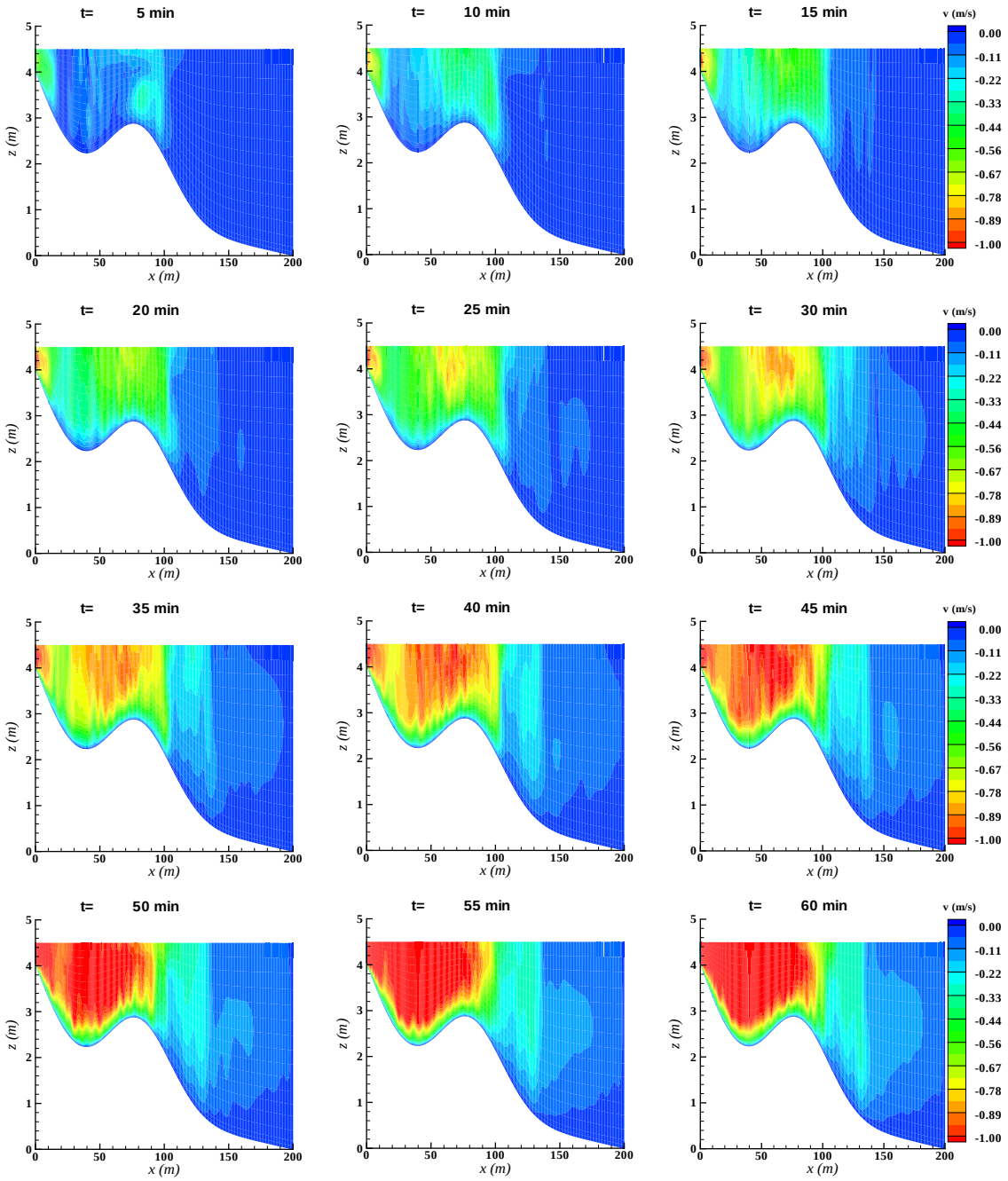

Figure 49. Case 10: Vertical cross-section contour plots of the alongshore-averaged alongshore current (v). Time progression at 5 min intervals showed the migration of the current over the bar into the trough area.

Linearly distributing the pressure term over the top 3 grid points produced cross-shore flow at the top boundary at early time (5 min) for Case 11. Alongshore currents slowly migrated into the trough at similar rates to the other forcing distributions.

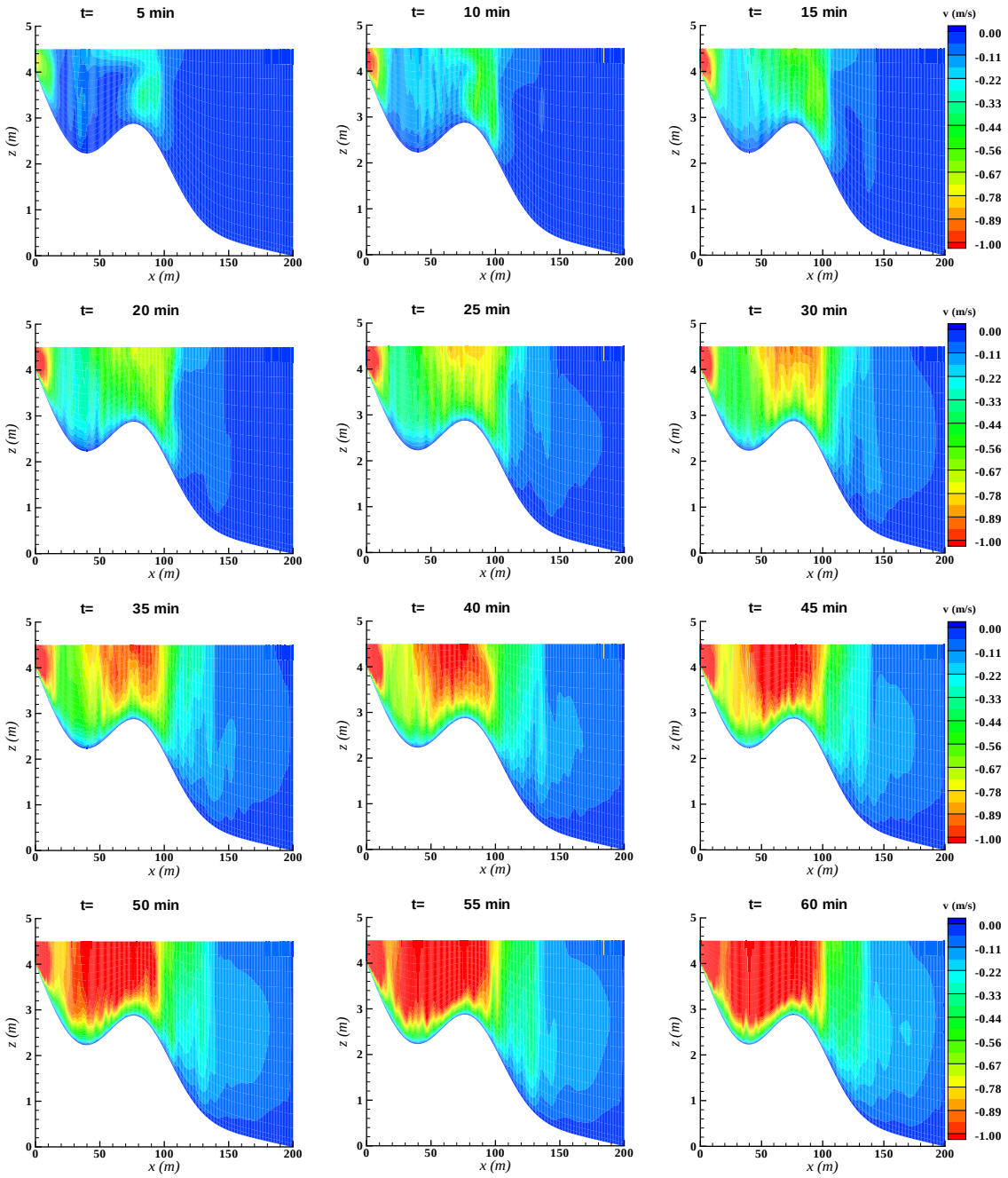

Figure 50. Case 11: Vertical cross-section contour plots of the alongshore-averaged alongshore current (v). Time progression at 5 min intervals showed the migration of the current over the bar into the trough area.

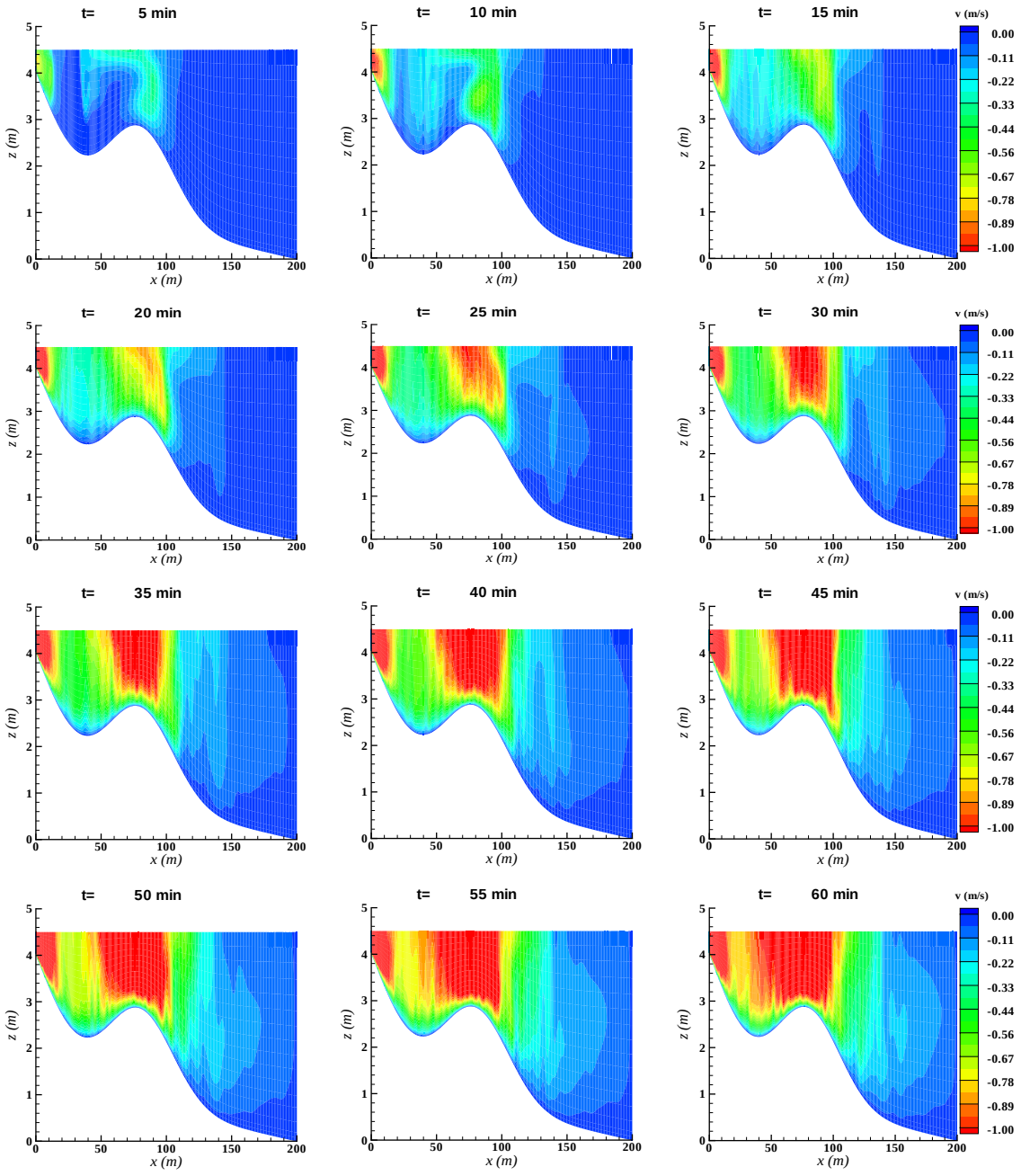

Figure 51. Case 12: Vertical cross-section contour plots of the alongshore-averaged alongshore current (v). Time progression at 5 min intervals showed the migration of the current over the bar into the trough area.

Case 12 examined the affect of applying a shear stress at the surface. At t = 5 min, the effect of the shear stress was apparent with a stronger shoreward migration of the

surface current. Currents were stronger, and less spread out in the cross-shore over time compared to other examples. A boundary layer still existed, but was less apparent.

Vorticity

Plots of the vertical vorticity in depth integrated flow models had been used in previous 2D studies as a means to observe migrating large scale features in the mean flow. The 3D vertical vorticity contour plots, however, included significant small scale features that dominated the principal impression conveyed (Figure 52A). Due to the inherent three-dimensionality of vortex dynamics, and the fine resolution of the grid that allowed turbulence to be calculated at much smaller length scales than previous 2D studies, direct vorticity comparisons were not particularly useful for large scale flow features. Contour plots and velocity vectors of alongshore velocity (Figure 52B) provided a more readily interpreted and informative tool for alongshore current flow analysis, and confirmed the mean alongshore current was not simply chaotic, as the vorticity contours had indicated.

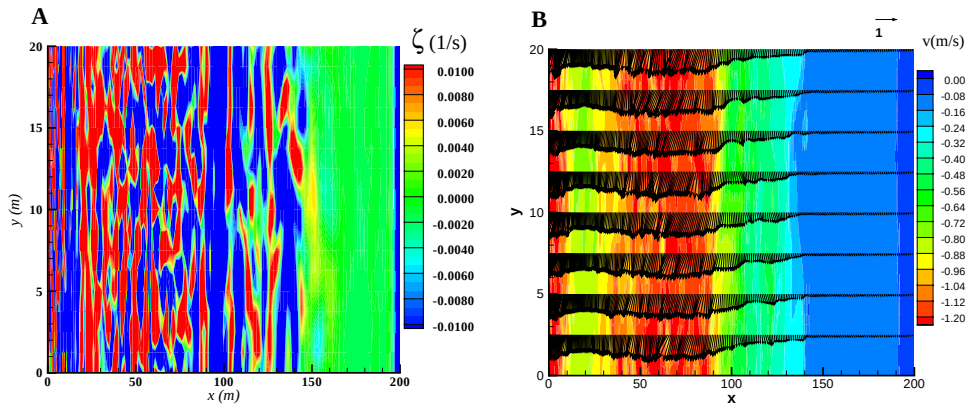

Figure 52. Comparison of surface vorticity component (ω_z) and alongshore surface current (v) contours in the cross-shore (x) and alongshore (y) domain. A) Vorticity contours showed small scale features that were highly erratic and suggested a very unstable current. B) Velocity contours and vectors of the same data showed a strong current that had peaks at the shoreline and around the bar. Snapshot was of Case 11 at t = 50 min.

Small scale perturbations seen as vorticity patches with horizontal length scales on the order of 2 m were very apparent in the cases examined in Figure 52 and Figure 53. Similar small scale vortex structures were not produced in 2D model studies and further understanding of what properties influenced these structures in 3D were needed. Two potential influences other than the vertical distribution of forcing were examined: spatial grid size and velocity filtering.

Two-dimensional models did not produce the same vorticity structures as seen in the 3D model for a number of reasons. They used coarser grids, with horizontal grid spacing in the range of 2 to 5 m which removed the ability to calculate small-scale turbulence that might have been present. As well, a 2D, depth-averaged flow could have never produced 3D turbulence. Instead of a cascade of turbulence from larger to smaller scales, a 2D flow would have produced eddies that coupled with each other to form larger eddies, known as an inverse cascade of energy. Horizontal vorticity (ω_x, ω_y) was also not produced in 2D flows. In a 3D flow, these turbulent eddies could have been stretched and tilted, which could have influenced vertical vortex structures (ω_z).

To study the effect of horizontal grid resolution on the vorticity contours, the model output velocities were spatially averaged to a 5 m grid resolution and then vertical vorticity was calculated from the averaged velocity. The 3D model had a spatially varying, high resolution grid that was able to calculate turbulence at scales on the order of 0.2 m in the nearshore to 1 m at the offshore. By taking an average velocity over a 5 m by 5 m spatial grid, the small scale perturbations were removed. The effective grid resolution was reduced from (*nx, ny*) = (257, 33) to (*nx, ny*) = (40, 4). Spatial averaging the velocities with a coarser resolution smoothed out the vorticity contours (Figure 53A).

This result demonstrated one of the influences of grid resolution on the resulting vorticity contours. Comparing Case 1 and Case 14 (discussed later) that both used depth-uniform forcing on the 200 m x 198 m physical domain at different horizontal grid resolution also showed that the finer grid produced smaller scale turbulent features. The omission of 3D turbulence and the use of coarse grids found in 2D models did not permit the presence of small-scale turbulent features as was seen in our results. Time averaging over a variety of time intervals was done to find the mean vorticity field. When the vorticity data were averaged over long time periods, as in Figure 53C, the associated vorticity contour plots were smoothed out. Time averaging over small time periods, however, did not smooth out the contour plots.

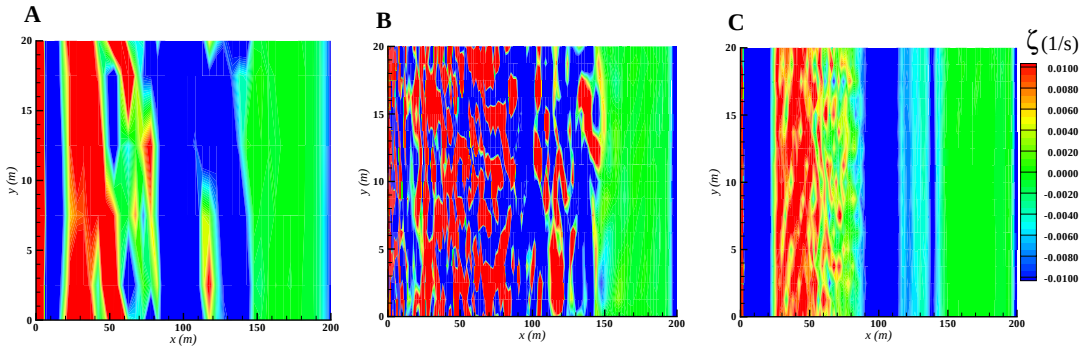

Figure 53. Sample comparison of spatially averaged, original vorticity, and time-averaged contours at vertical grid point nz-1. Plots were generated from Case 11 data, t = 50 min. A) vorticity contours for spatially averaged data at 5 m grid spacing. B) original vorticity plot on a variable grid. C) time averaged (50 min) vorticity contours of the same simulation. Time averaging of the data over long time periods showed the mean vorticity and smoothed out the contours.

Energy spectra of the u- and v-velocities were used to determine the frequency band at which the majority of the energy was concentrated. When significant energy was concentrated at lower frequencies, it indicated that the large scale features were more important to the transportation of energy. (E.g., alongshore currents with shear waves

had a peak energy concentration of about 1 m^2/s^2 located around 0.01 Hz.) Spectra of the currents during run-up time of the model were generated at various locations of x and z within the domain. Results showed that the energy was concentrated at low frequencies. In the spectral analysis of the depth-averaged currents at x = 40 m in the cross-shore (center of the bar trough), the u-velocity spectrum had a peak at 0.047 Hz (Figure 54), and the v-velocity spectrum had a peak at 0.031 Hz (Figure 55). The time and depth-averaged u- and v-velocities were 0.004 m/s, and -0.52 m/s respectively. The length scales of the peak energy were determined by using the following equation:

$Length(m) = \frac{\sqrt{E_p(m^2/s^2)}}{f_p(Hz)}$, where subscript (p) indicated the peak value. The length scale of the peak energy structures in the u-energy spectrum was approximately 2 m, with fluctuation velocities around 0.10 m/s. The length scale in the v-energy spectrum was approximately 6 m, with velocities around -0.2 m/s. The energy spectra showed that a significant amount of energy in the velocity field was contained within the small-scale features shown. This was also verified by taking the RMS of the peak v-velocity, $(V_p - V_{avg})/V_{avg}$, which was equal to almost 50% of the mean flow at this cross-shore location. Spectral analysis on equilibrated flow (t > 60 min) produced slightly different results because the effects of run-up and current migration were not present. The purpose of the filtering, however, was to determine the energy distribution in the currents at times when small scale instabilities were first appearing.

Low-pass filtering the velocities at these frequencies to remove high frequency fluctuations was done to determine the effect (Figure 56 and Figure 57). Filtering above the peak frequencies was an attempt to remove high-frequency noise that might have

obscured trends in the data. In this particular example, filtering did not remove the small scale perturbations from the velocity signal because they were where the bulk of the energy of the current lied.

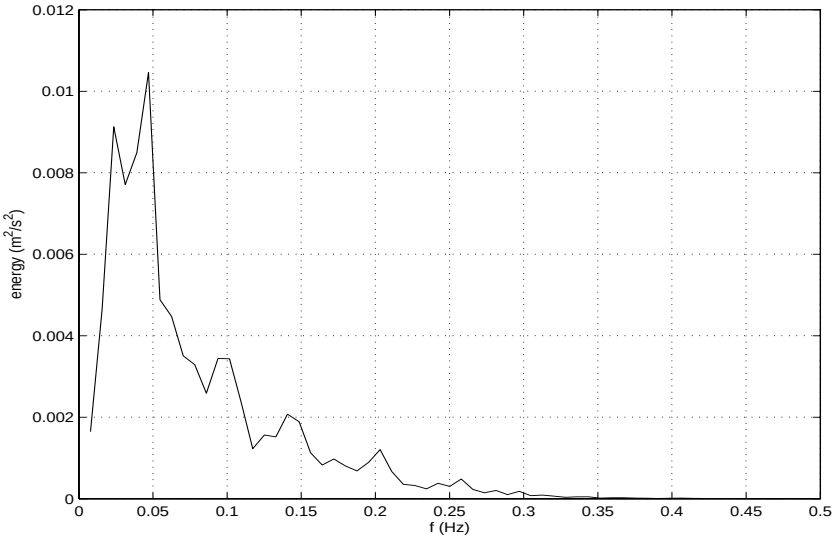

Figure 54. Depth-averaged U(xo,yo,t)-velocity energy density spectrum for Case 8, where x_o = 40 m, y_o = 10 m, t =12-66 min. Data was sampled at 1 Hz, totaling 3200 data points. Peak frequency = 0.0469 Hz. Maximum energy = 0.0105 m^2/s^2.

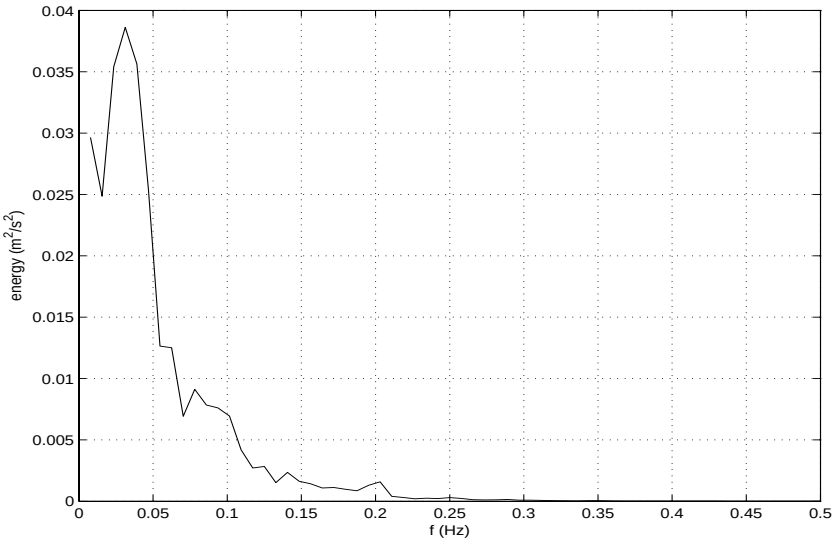

Figure 55. Depth-averaged V(xo,yo,t)-velocity energy density spectrum for Case 8, where x_o = 40 m, y_o = 10 m, t = 12-66 min. Data was sampled at 1 Hz, totaling 3200 data points. Peak frequency = 0.0313 Hz. Maximum energy = 0.0386 m^2/s^2.

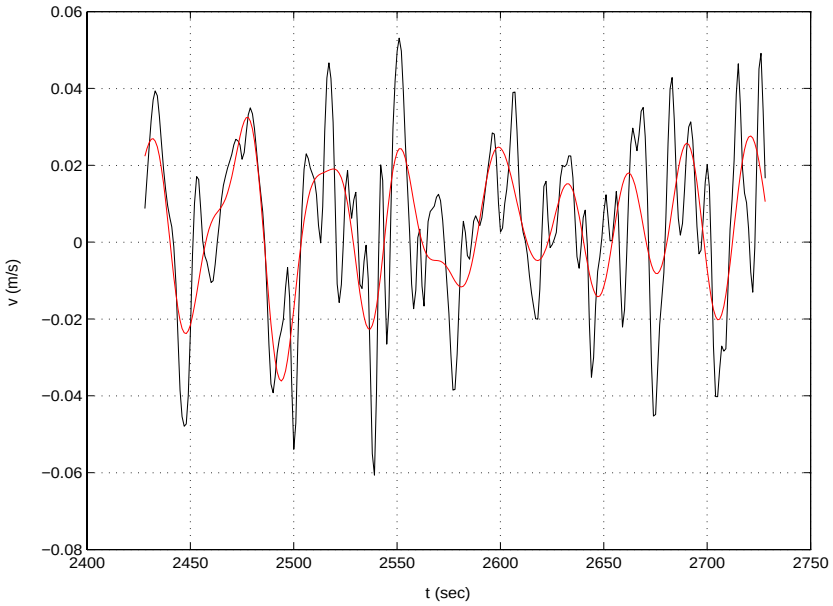

Figure 56. Time sample of velocity fluctuations (black) and the low-pass filtered (red) depth-averaged u-velocity at 0.03 Hz taken from energy spectrum data. $U(x_o,y_o,t)$ for Case 8, where $x_o = 40$ m, $y_o = 10$ m, t = 40-46 min.

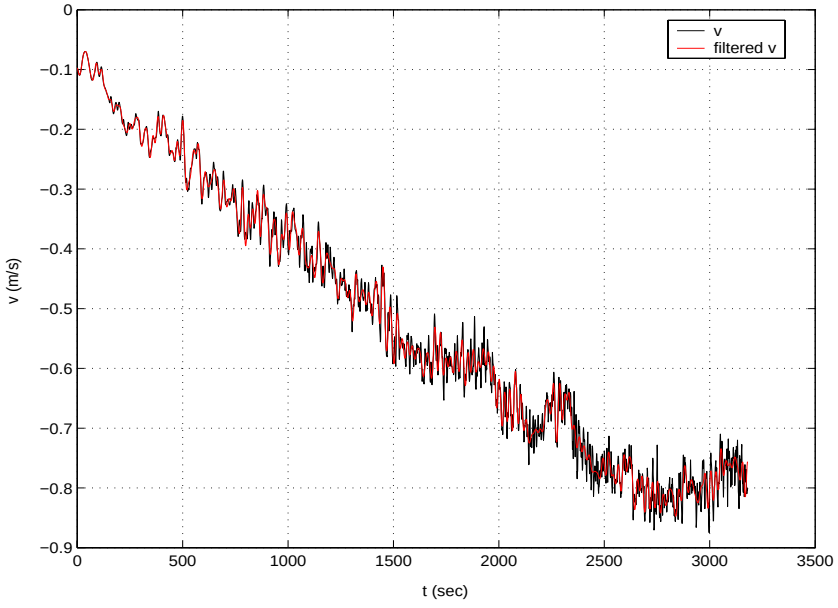

Figure 57. Time sample of raw data (black) and the low-pass filtered (red) depth-averaged v-velocity at 0.046 Hz. $V(x_o,y_o,z_o,t)$ for Case 8, where $x_o = 75$ m, $y_o = 10$ m, t = 12-66 min.

Effect of Domain Length

Two domain lengths were used for the simulations. The 20 m domain prohibited the development of large scale alongshore shear instabilities [O (100 m)] that could have influenced the cross-shore diffusion of the alongshore current. The 20 m domain restricted the focus of the study on the effects of the vertical distribution of the forcing. To verify that this assumption was correct, simulations with depth-uniform forcing in both directions were run on 20 m and 200 m domains. The alongshore current remained stable on the 20 m domain for the length of the run. On the 200 m domain, however, the current became unstable over time, and broke down into features with alongshore wavelengths of approximately 100 m, similar to those presented in previous 2D model results (Slinn et al. (1998) and Özkan-Haller and Kirby (1999)). These tests verified that domain length influenced the stability of the alongshore current. The extent of the domain length's influence on the alongshore currents generated was dependent on the vertical distribution of forcing. Three vertical distributions were tested. Case 14 was forced with a depth-uniform distribution. Case 15 used the vertical distribution from Case 10, and Case 16 used the distribution from Case 11.

When the domain length was increased and large scale instabilities were allowed to influence the alongshore current, they spread the mean alongshore current laterally. The instability of $\overline{V}(x)$ was most visible when the model was forced by a depth-uniform force (Figure 58). Without the large-scale instabilities, the current continued to grow over the bar. The large-scale shear instabilities also decreased the maximum mean alongshore current velocities through increased cross-shore mixing. This was qualitatively visible in Figure 58 to Figure 60 that compare the short and long domain results of the alongshore

depth-averaged alongshore currents for the various forcing distributions. When F_x was not entirely uniform as in Case 14, the alongshore current was spread laterally at earlier times. It appeared that the instability imposed by the vertical shear of the cross-shore currents influenced the stability of the large-scale features of the alongshore current as well, and caused the shear waves to develop at earlier times.

The short domain produced stronger currents over the bar. The alongshore current was more widely spread across the cross-shore with the long domain that included the effects of the large scale instabilities. A strong jet remained at the shoreline for both domain lengths that indicated the large scale motions had minimal effect on the currents at that location.

Large-scale shear instabilities on the order of 100 m were still present in the 200 m domain when forcing was not depth uniform. Vertical vorticity contours for Cases 14 -16 are compared in Figure 61 to Figure 63.

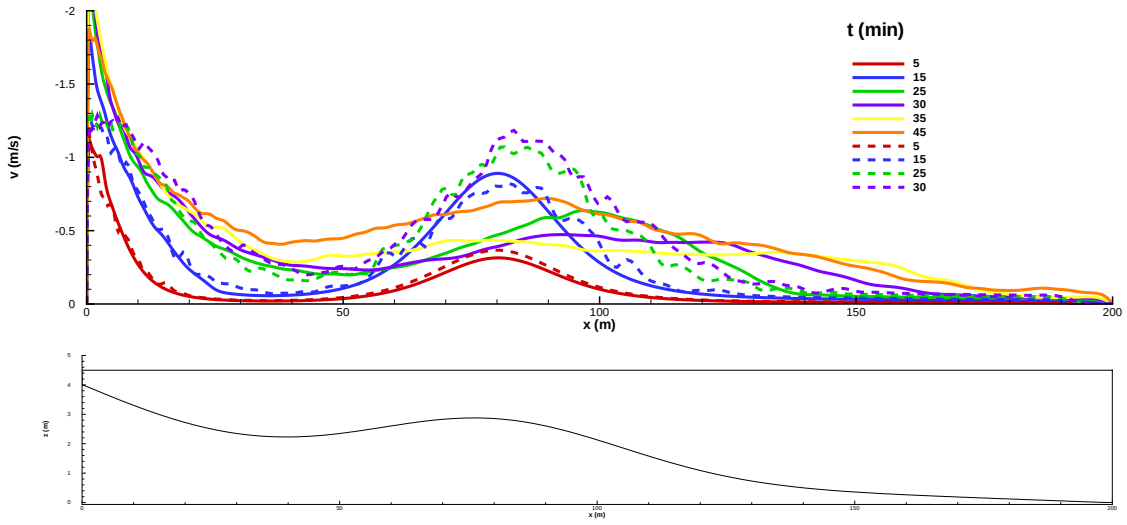

Figure 58. Influence of domain length on alongshore currents for depth-uniform forcing: Alongshore and depth-averaged alongshore current profiles as a function of cross-shore position and time. Solid lines represent the 200 m alongshore domain. Dashed lines represent the 20 m alongshore domain.

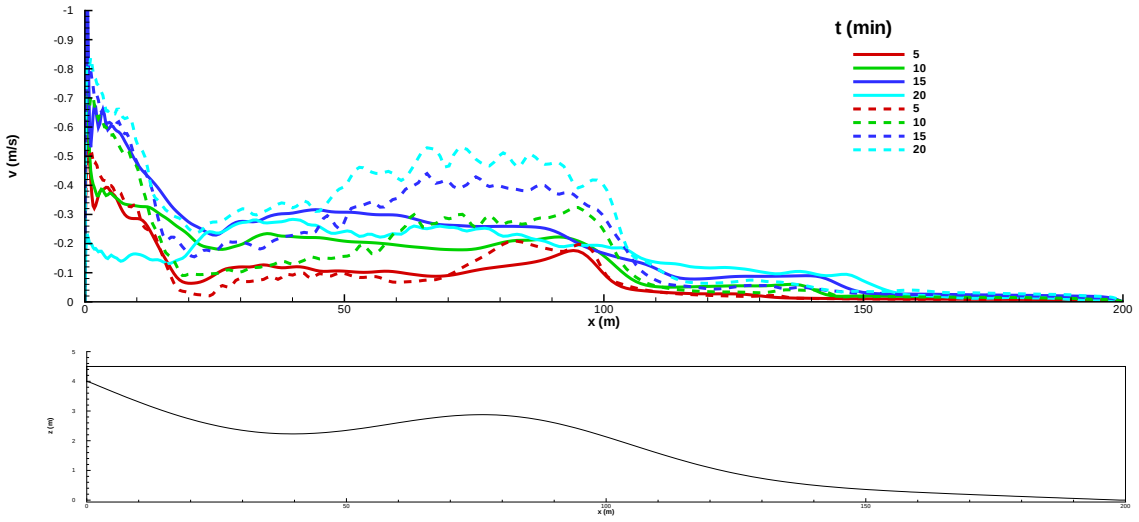

Figure 59. Influence of domain length on alongshore currents for Case 10 forcing: Alongshore and depth-averaged alongshore current profiles as a function of cross-shore position and time. Solid lines represent the 200 m alongshore domain. Dashed lines represent the 20 m alongshore domain.

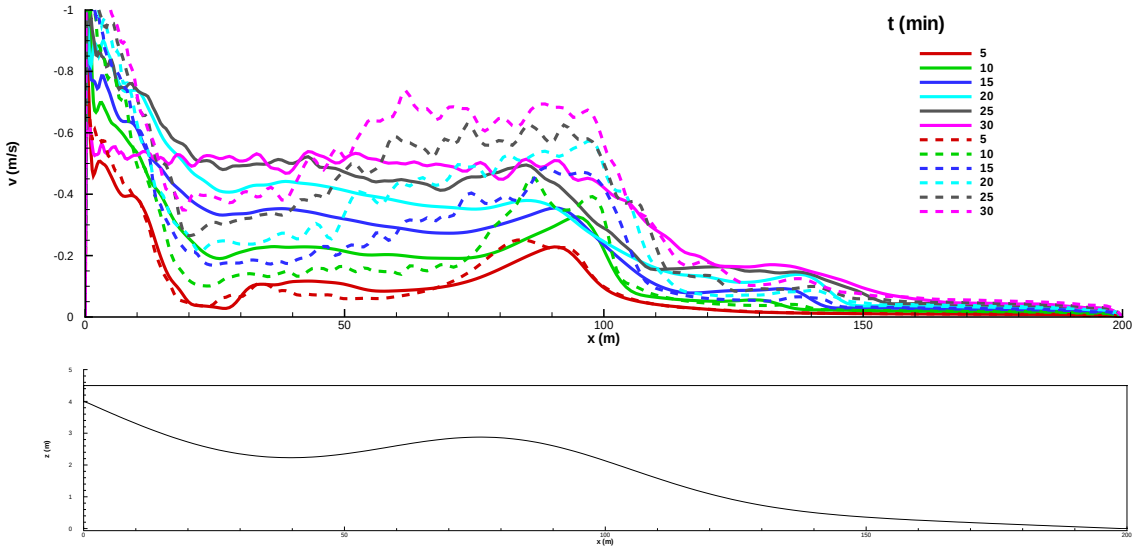

Figure 60. Influence of domain length on alongshore currents for Case 11 forcing: Alongshore and depth-averaged alongshore current profiles as a function of cross-shore position and time. Solid lines are 200 m alongshore domain. Dashed lines are for 20 m alongshore domain.

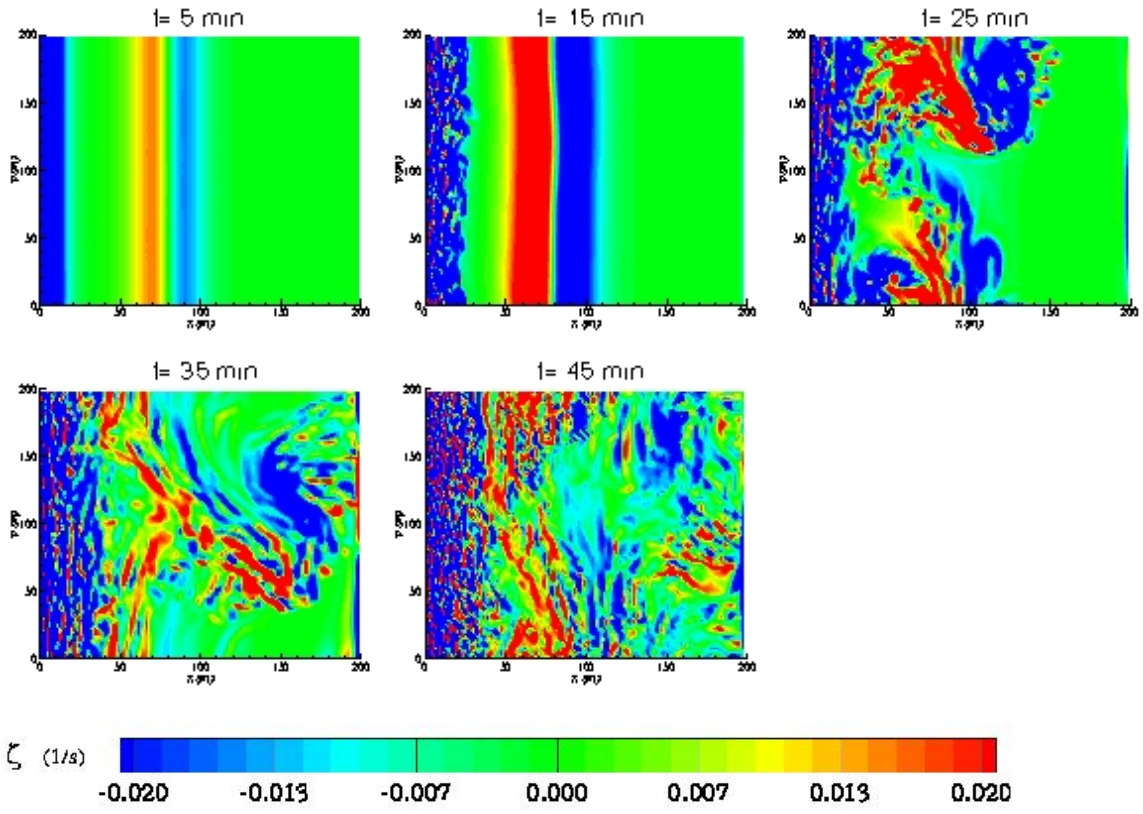

Figure 61. Case 12: Contours of the depth-averaged vorticity as a function of time. The current became unstable around 20 min and produced large scale instabilities (t = 25 min) that broke down into smaller scale turbulence (t = 45 min).

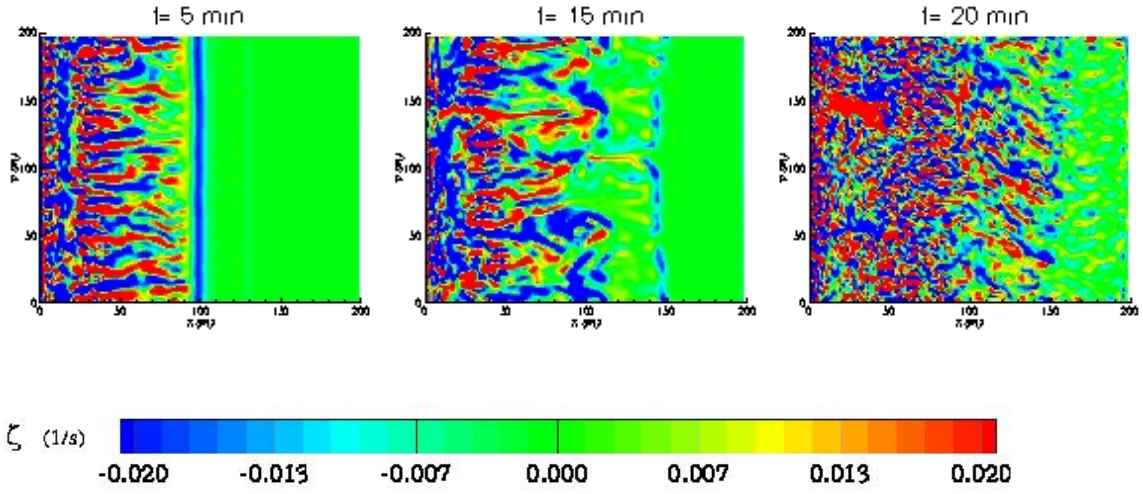

Figure 62. Case 15: Contours of the depth-averaged vorticity as a function of time. The current became unstable at the shore almost immediately (t = 5 min) and large scale instabilities were less visible.

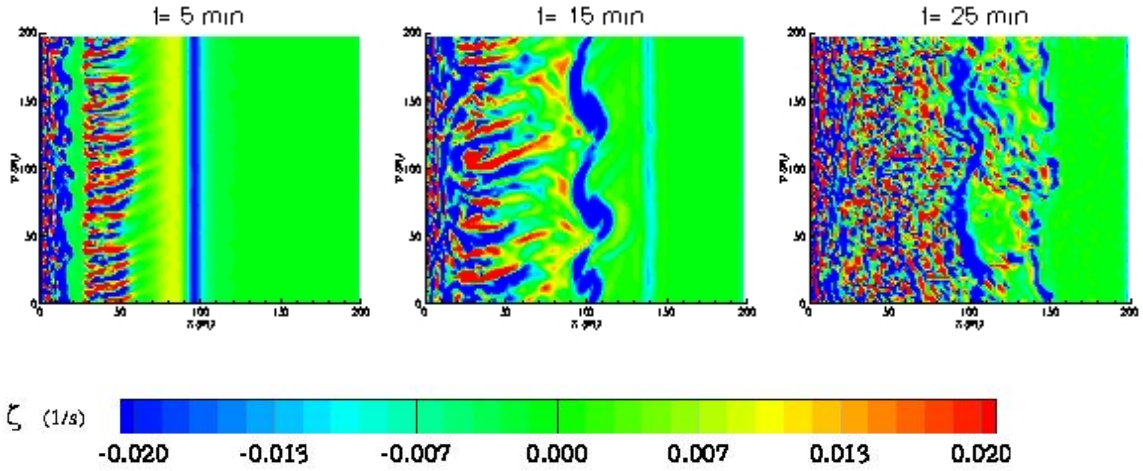

Figure 63. Case 16: Contours of the depth-averaged vorticity as a function of time. The current at the shoreline became unstable at early time, while the current over the bar became unstable around 15 min, and evolved into smaller scale turbulence (t = 25 min).

The large-scale [O (70 m)] instabilities apparent in Case 16 (t = 15 min) resulted from the instability of the alongshore current similar to the depth-uniform case. With the depth-linear forcing in the top three grid points, the effect of the top grid point was reduced because of the free-slip condition. This removed a portion of the depth-varied forcing, and put a larger influence on the depth-uniform component. This resulted in a more stable alongshore current over the bar that was strongly influenced by the alongshore shear instabilities on the current. Although the small-scale vorticity features obscured the presence of the larger scale shear waves, they were still present, and influenced the alongshore current position over time. In effect, the depth-dependent forcing pushed the peak alongshore current velocities into the trough, and the shear waves spread the current horizontally, with preferential spreading in the shoreward direction for depth-dependent forcing.

CHAPTER 5
SUMMARY AND DISCUSSION

Findings and Results

A 3D LES model was adapted to simulate alongshore currents forced by breaking waves. It produced strong alongshore currents in the trough area without the use of a roller model, alongshore pressure gradients, alongshore shear waves, or ad-hoc tuning of the bottom friction coefficient. The 3D model allowed the effect of vertical forcing on alongshore current structure to be studied on a small domain [O (20 m)]. The development and migration of alongshore currents were analyzed as the alongshore current spun up to steady state. The model did not specify the bottom friction and achieved reasonable, balanced values of $\overline{V}(x)$ for the specified wave field conditions. The effect of grid resolution, vertically dependent forcing, and alongshore domain length were all examined.

The LES closure scheme was sensitive to grid aspect ratios, and overall grid resolution. Aspect ratios less than 4:1 generated reproducible currents at varying grid resolutions. Cross-shore flow was most affected by grid aspect ratio. Grid cells that were long and flat produced preferential undertow. The overall magnitude and location of the mean alongshore current, however, was not as sensitive to grid aspect ratio. The five cases tested produced similar mean alongshore current profiles in the cross-shore.

The ideal vertical distribution of the radiation stress gradients was dependent on the situation considered. In a phase-averaged model, assumptions were made for the forcing terms that existed outside the modeling domain. Depth-uniform forcing produced

alongshore current and shear instabilities similar to 2D models. Non-uniform vertical forcing, however, produced small scale structures that were not seen in 2D models. Vertical forcing effectively produced cross-shore currents that mixed the alongshore current horizontally: currents over the bar were pushed shoreward by wave breaking stresses, and currents at the shore were pulled seaward into the trough by the resulting undertow. Case 10 that had the pressure term uniformly distributed over the top three grid points, was the most effective means of mixing the alongshore current, and produced reasonable peak velocities [O (1 m/s)] in the trough. Case 12 produced the least satisfactory results. It implemented $1/6^{th}$ of F_x as a surface shear stress. The effect on the location of the alongshore current was minimized, however, by the co-implementation of the free-slip boundary condition at the surface. The alongshore current maxima that resulted remained over the bar, and at the shoreline, with maximum velocities exceeding 1.5 m/s. It was learned that the methods of implementing the surface stress forcing were incompatible with the free-slip boundary condition. Alternate boundary conditions that will allow a surface stress can be implemented in future work.

The use of a 3D, non-hydrostatic model produced strong vertical mixing in the cross-shore. Vortex structures similar to those from lab results were produced in the model. Turbulence is described as a 3D phenomenon and its effects on fluid dynamics are best modeled in a 3D system. Some previous two-dimensional models attempted to parameterize effects of 3D turbulence by assuming isotropic horizontal diffusion. Non-isotropic net cross-shore mixing will always be present as long as there is cross-shore circulation and the alongshore currents are not entirely depth-uniform. This always occurs in nature because of the bottom boundary layer and cross-shore

non-uniformity of currents that are advected horizontally by vertically dependent forcing. The 3D model also captured another important coupling between horizontal and vertical structures of the flow. Small-scale turbulence generated in the vertical (ω_x and ω_y) could be stretched and tilted. These evolved into small scale vertical turbulent structures (ω_z) that produced enhanced cross-shore diffusion.

Complementary lines of investigation, such as the formulations in the quasi-3D implementation of SHORECIRC (Zhao et al., 2003), had considered net effects of the undertow on depth-averaged currents. They did not observe current behavior qualitatively similar to results presented here. This was explained by the fact that the quasi-3D information was used primarily to estimate an isotropic horizontal diffusion coefficient. This was a good approximation if the alongshore current had been depth-uniform because the shoreward mass-flux in the top half of the water column would have carried equal amounts of alongshore momentum as the undertow had carried offshore. If the alongshore current was depth-dependent, however, this approximation was no longer adequate. Depth-dependence of the currents occurred because of several factors. These could have included depth-dependent momentum input, a thick boundary layer developed by bottom friction, or from ongoing depth-dependent cross-shore diffusion. The net effect of 3D cross-shore circulation produced non-isotropic, preferentially shoreward diffusion of the alongshore currents.

Increasing the domain length influenced the alongshore velocity profiles. Peak currents were decreased, and the profile was laterally spread further across the cross-shore domain. Domain lengths on the order of 200 m produced large scale shear waves that horizontally diffused the mean alongshore current across the surfzone. This

feature was most noticeable with depth-uniform forcing. The magnitude of the influence of the large scale motions was dependent on the vertical distribution of forcing. When a greater portion of the forcing was depth-uniform over the water depth, as in Case 14, the large scale instabilities were the main source of horizontal mixing of the alongshore current. In Case 15, however, the effect of large scale motions was not as apparent. Horizontal diffusion of the current was present due to large scale motions not captured in the small domain, but large structures were obscured by the small-scale instabilities produced by the vertical distribution of forcing. Including the effects of vertically dependent forcing and large scale shear instabilities produced mean alongshore currents that were weaker, and centered in the bar trough. The omission of either of these effects produced alternative alongshore current distributions. The omission of vertically dependent forcing led to weaker, more stable currents centered over the bar, whereas the omission of shear waves led to stronger currents centered in the bar trough.

Future Work

A great deal remains to be done on this line of work. Linear stability analysis of the three velocity profiles should show that the growth rates of instabilities of the vertical shear are more rapid than growth rates from the horizontal shear. Model improvement continues with the addition of mass flux to future simulations. Alternative vertical distributions of the alongshore and cross-shore forcing based on complimentary model and laboratory studies to include effects of breaking and nonlinear waves should also be examined. Simulations with different wave conditions (H_o, T_p, θ_o) should also be pursued and produce different alongshore current dynamics and increase understanding on the relative importance of including large scale shear instabilities and vertically distributed forcing.

Larger domains and finer grid testing should also improve the statistics of the model results. Larger domains will more effectively include alongshore instabilities and reduce the wall effects on the offshore boundary. Finer grids, especially in the vertical, will better resolve turbulence closer to the boundaries, but may affect the stability of the pressure solver. Comparing model results to available field data from the DELILAH experiment could be used to help validate the model.

LIST OF REFERENCES

Allen, J.S., P.A. Newberger, and R.A. Holman, Nonlinear shear instabilities of alongshore currents on plane beaches, *Journal of Fluid Mechanics, 310*, 181-213, 1996.

Bowen A.J., and R.A. Holman, Shear instabilities of the mean longshore-current, 1, theory, *Journal Of Geophysical Research, 94,*18023-18030, 1989.

Church, J.C., E.B. Thornton, and J. Oltman-Shay, Mixing by shear instabilities of the longshore current, *Coastal Engineering 1992*, Chapter 230, 1992.

Dally, W.R., and R.G. Dean, Suspended sediment transport and beach evolution, *Journal of Waterway, Port, Coastal and Ocean Engineering, 110*,15-33, American Society of Civil Engineers,1984.

Deigaard, R., A note on the three-dimensional shear stress distribution in a surf zone, *Coastal Engineering, 20*, 157-171, 1993.

Deigaard, R., and J. Fredsoe, Shear stress distribution in dissipative water waves, *Coastal Engineering, 13*, 357-378, 1989.

Dodd, N., On the destabilization of a longshore current on a plane beach: Bottom shear stress, critical conditions, and onset of instability, *Journal of Geophysical Research, 99*, 811-824, 1994.

Dodd, N., V. Iranzo, and A.J.H.M. Reniers, Shear instabilities of wave-drive alongshore currents, R*eviews of Geophysics, 38*, 437-463, 2000.

Dodd, N., and E.B. Thornton, Growth and energetics of shear waves in the nearshore, *Journal of Geophysical Research, 95*,16,975-16,083, 1990.

Falques, A., and V. Iranzo, Numerical simulation of vorticity waves in the nearshore, *Journal of Geophysical Research, 99*, 825-841, 1994.

Faria, A.F.G., E.B. Thornton, T.C. Lippmann, and T.P. Stanton, Undertow over a barred beach. *Journal of Geophysical Research, 105*, 16,999-17,010, 2000.

Fredsoe, J. and R. Deigaard, *Mechanics of Coastal Sediment Transport*, 369 pp., World Scientific Publishing, River Edge, NJ, 1992.

Greenwood, B., and D.J. Sherman, Longshore current profiles and lateral mixing across the surf zone of a barred nearshore, *Coastal Engineering, 10*, 149-168, 1986.

Haines, J.W., and A.H. Sallenger, Vertical structure of mean cross-shore currents across a barred surf zone, *Journal of Geophysical Research, 99,* 14,223-14,242, 1994.

Hansen, J.B., and I.A. Svendsen, A theoretical and experimental study of undertow, *Proceedings of the 19th International Conference of Coastal Engineering*, Houston, TX, ch.151, pp. 2246-2262, 1984.

Holman, R.A., Nearshore processes, *Reviews of Geophysics, Supplement*, 1237-1247, 1995.

Lele, S. K., Compact finite difference schemes with spectral-like resolution, *Journal of Computational Physics, 103*, 16-42, 1992.

Li, L., and R.A. Dalrymple, Instabilities of the undertow, *Journal of Fluid Mechanics, 369*, pp175-190, 1998.

Lippmann, T.C., T.H.C. Herbers, and E.B. Thornton, Gravity and shear wave contributions to nearshore infragravity motions, *Journal of Physical Oceanography*, 29, 231-239, 1999.

Lippmann, T.C., E.B. Thornton, and A.J.H.M. Reniers, Wave stress and longshore current on barred profiles, *Coastal Dynamics '95: International Conference on Coastal Research in Terms of Large Scale Experiments*, edited by W.R. Dally, 401-412, American Society of Civil Engineers, Reston, VA, 1995.

Longuet-Higgins, M.S., Longshore currents generated by obliquely incident sea waves, 1. *Journal of Geophysical Research*, 75, 6778-6789, 1970.

Longuet-Higgins, M.S., and R.W. Stewart, Radiation stresses in water waves; a physical discussion, with applications, *Deep-Sea Research, 11*, pp.529-562, 1964.

Matsunaga, N., K. Takehara, and Y. Awaya, Coherent eddies induced by breakers on a sloping bed, *Proceedings of the 21st International Coastal Engineering Conference,* edited by B.L. Edge, pp.234-245, American Society of Civil Engineers, Reston, VA, 1989.

Matsunaga, N., K. Takehara, and Y. Awaya, The offshore vortex train, *Journal of Fluid Mechanics, 276*, 113-124, 1994.

Mei, C.C., *The Applied Dynamics of Ocean Surface Waves*, 465 pp., World Scientific Publishing, River Edge, NJ, 1989.

Mellor, G., The three-dimensional current and surface wave equations, *Journal of Physical Oceanography, 33*, 1978-1989, 2003.

Noyes, T.J., R.T. Guza, S. Elgar, and T.H.C. Herbers, Field observations of shear waves in the surf zone, *Journal of Geophysical Research, 109*, CO1031, 2004.

Oltman-Shay, J., P.A. Howd, and W.A. Birkemeier, Shear instabilities of the mean longshore current, 2. Field data, *Journal of Geophysical Research, 94,* 18031-18042, 1989.

Özkan-Haller, H.T., *Nonlinear Evolution of Shear Instabilities of the Longshore Current*, Ph.D. dissertation, University of Delaware, Newark, DE, pp. 268, 1997.

Özkan-Haller, H.T., and J.T. Kirby, Nonlinear evolution of shear instabilities of the longshore current: A comparison of observations and computations, *Journal of Geophysical Research, 104*, 25953-25984, 1999.

Putrevu, U., J. Oltman-Shay, and I.A. Svendsen, Effect of alongshore nonuniformities on longshore current predictions, *Journal of Geophysical Research, 100*, 16119-16130, 1995.

Putrevu, U., and I.A. Svendsen, A mixing mechanism in the nearshore region, *Proceedings of the 23rd International Conference on Coastal Engineering*, edited by B.L. Edge, 2758-2771, American Society of Civil Engineering, Reston, VA, 1992.

Putrevu, U., and I. A. Svendsen, Three-dimensional dispersion of momentum in wave-induced nearshore currents, *European Journal of Mechanics*, 409-427, 1999.

Rayleigh, J.W.S., On the stability, or instability, of certain fluid motions, *Proceedings of the London Mathematical Society, 11*, 57-70, 1880.

Reniers, A.J.H.M., and J. A. Battjes, A laboratory study of longshore currents over barred and nonbarred beaches, *Coastal Engineering, 30*, 1-22, 1997.

Rivero, F.J., and A.S. Arcilla, On the vertical distribution of $\langle \tilde{u}\tilde{w} \rangle$, *Coastal Engineering, 25*, 137-152, 1995.

Scotti, A., C. Meneveau, and M. Fatica, Dynamic Smagorinsky model on anisotropic grid, *Physics of Fluids, 9*, 1856-1858, 1997.

Slinn, D. N., J.S. Allen, and R.A. Holman, Alongshore currents over variable beach topography, *Journal of Geophysical Research, 105*, 16,971-16,998, 2000.

Slinn, D.N., J.S. Allen, P.A. Newberger, and R.A. Holman, Nonlinear shear instabilities of alongshore currents over barred beaches, *Journal of Geophysical Research, 103*, 18,357-18,379, 1998.

Sobey, R.J., and R.J. Thieke, Mean flow circulation equations for shoaling and breaking waves, *Journal of Engineering Mechanics, 115*, 285-303, 1989.

Stive, M., and H. Wind, Cross-shore mean flow in the surf zone, *Coastal Engineering, 10*, 325-340, 1986.

Svendsen, I.A., Mass flux and undertow in a surf zone, *Coastal Engineering, 8*, 347-366, 1984a.

Svendsen, I.A., Wave heights and set-up in a surf-zone, *Coastal Engineering, 8*, 303-329, 1984b.

Svendsen, I.A., and J.B. Hansen, Cross-shore currents in surf-zone modelling. *Coastal Engineering, 12*, 23-42, 1988.

Svendsen, I.A., and R.S. Lorenz, Velocities in combined undertow and longshore currents, *Coastal Engineering, 13*, 55-79, 1989.

Svendsen, I.A., H.A. Schaffer, and J.B. Hansen, The interaction between undertow and the boundary layer flow on a beach, *Journal of Geophysical Research*, 92, pp. 11845-11856, 1987.

Thornton, E.B. and R.T. Guza, Transformation of wave height distribution, *Journal of Geophysical Research, 88***,** 5929-5938, 1983.

Thornton, E.B. and R.T. Guza, Surf zone longshore currents and random waves: Field data and models, *Journal of Physical Oceanography, 16*, 1165-1178, 1986.

Van Dongeren, A.R., and I.A. Svendsen, Nonlinear and quasi 3-D effects in leaky infragravity waves, Coastal *Engineering, 41*, pp.467-496, 2000.

Winters, K.B., H.E. Seim, and T.D. Finnigan, Simulation of non-hydrostatic, density-stratified flow in irregular domains. *International Journal for Numerical Methods in Fluids, 32*, 263-284, 2000.

Zhao, Q., I.A. Svendsen, and K. Haas, Three-dimensional effects in shear waves, *Journal of Geophysical Research, 108*, 3270, 2003.

BIOGRAPHICAL SKETCH

Kristen Splinter was born in Kingston, Ontario, Canada, on February 12, 1979. She grew up under the influence of hard-working parents. Her environmentally conscious mother taught her to appreciate the delicate balance of nature. Having spent most of her time in close proximity to water, she grew a desire to protect the animals that rely on it for life. After graduating from high school in 1998, she pursued a degree in Civil-Environmental Engineering at Queen's University at Kingston (located in Kingston, Ontario, Canada). Throughout this time, she continued to participate in environmental causes, and focused her work on water quality and coastal resources. The Natural Science and Engineering Research Council of Canada (NSERC) funded her undergraduate research, studying water resource management using wetland technology. In 2002, she attained the degree of Bachelor of Science in Engineering with First Class Honors.

Upon completion of her undergraduate degree, she wanted to continue her research career, and gain a greater understanding of coastal processes. She chose to attend the University of Florida, for its program and sunny location. Here she pursued the degree of Master of Science in Coastal and Oceanographic Engineering, under the guidance of her advisor, Dr. Donald N. Slinn. Having not tired of learning about coastal issues, and wanting a deeper scientific background in her related fields of study, she plans to attain her Ph.D. in Oceanography, under the guidance of Drs. Robert Holman and Tuba Özkan-Haller at Oregon State University starting in September of 2004.